PONTIFICIA UNIVERSIDAD CATÓLICA DE VALPARAÍSO

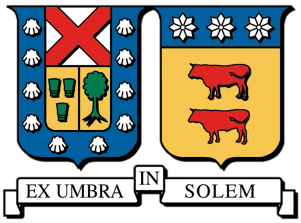

PONTIFICIA UNIVERSIDAD CATÓLICA DE VALPARAÍSO

INSTITUTO DE FÍSICA

UNIVERSIDAD TÉCNICA FEDERICO SANTA MARÍA

DEPARTAMENTO DE FÍSICA

VALPARAISO - CHILE

DOCTORADO EN CIENCIAS FÍSICAS

Characterizing the Intergalactic Medium in the Cosmic Web

Karen Marina Martínez Acosta

TESIS PARA OPTAR AL GRADO DE DOCTORA EN CIENCIAS FÍSICAS

PROFESOR GUÍA:

Dr. Nicolás Andrés Tejos Salgado

COMITÉ DE TESIS:

Dra. Yara Jaffe

Dr. Joseph Burchett

Dr. Raphael Gobat

March 10, 2026

CONSTANCIA DE VALIDACIÓN Y CONFIDENCIALIDAD DE MONOGRAFÍA A REPOSITORIO ACADÉMICO

1.- IDENTIFICACIÓN DEL TRABAJO ACADÉMICO

Tipo de monografía (marcar una opción): ☐ Memoria o trabajo de título ☒ Tesis de Postgrado

Título del trabajo: Characterizing the Intergalactic Medium in the cosmic web

Nombre del candidato(a): Karen Marina Martínez Acosta

Carrera / Grado: Doctorado en Ciencias Físicas

Campus: Casa Central Valparaíso **Departamento:** Departamento de Física

2.- VALIDACIÓN DEL PROFESOR GUÍA/DIRECTOR DE TESIS

Yo, Nicolás Andrés Tejos Salgado, en mi calidad de profesor(a) guía/director(a) del trabajo académico mencionado anteriormente **DEJO CONSTANCIA** que:

- He revisado esta versión del documento y corresponde a la versión final aprobada del trabajo.
- El trabajo cumple con los requisitos académicos y de formato establecidos por la institución.

3.- EVALUACIÓN DE CONFIDENCIALIDAD POR PROPIEDAD INDUSTRIAL (marcar una opción)

☒ El trabajo **NO contiene** información que amerite confidencialidad y puede ser publicado de inmediato en repositorio con acceso abierto.

☐ El trabajo **CONTIENE** información con potenciales implicancias de propiedad industrial o intelectual y requiere un periodo de confidencialidad (**embargo**) por **(marcar una opción):**

☐ 6 meses ☐ 12 meses ☐ 2 años ☐ 3 años ☐ 5 años ☐ 10 años

Fundamentación de la necesidad de confidencialidad (obligatorio si se solicita embargo):

4.- FIRMAS

Profesor(a) guía o director(a) de memoria o tesis:

Fecha: 29-01-2026 **Firma:** 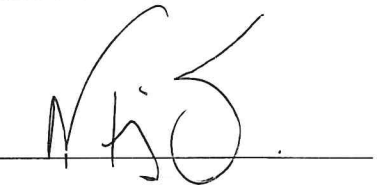

Estudiante o Candidato(a):

Fecha: 29-01-2026 **Firma:** 

Este formulario debe ser insertado como página 2 de la memoria o tesis, completado y firmado por estudiante y profesor(a) antes de la entrega en portal PRISMA de Biblioteca USM.

Dedicatory

Dedicado a los seres que amo y amaré.
A mis dos Fer gracias por compartir un planeta y una época conmigo.

Esta tesis fue escrita desde el lugar donde todos mis sueños comenzaron, en el mismo contexto, más de 20 años después. Aunque esto representa la finalización de una aventura llena de tantos sentimientos y trabas, no es un logro ni personal ni único; está dedicado a todas las personas y momentos que hicieron que fuera posible. El amor por lo que hago y la culminación de este doctorado vienen acompañados de toda una historia que me acompañará a lo largo de toda la vida. Se acostumbra un agradecimiento, primero a Dios, que siempre estuvo todo en sus manos, aunque a veces parecía que no, al final sí. A mis padres, que toda la vida me supieron apoyar en lo que pudieron; gracias por cada sacrificio que hicieron para que yo pudiera llegar, por estar en todas las formas que ni siquiera lo imaginan, a mi padre, que me dijo que podía cumplir mis sueños, y a mi madre, que hizo todo lo necesario en todas las formas que los demás no hacen válidas. Si lo pongo como una dedicatoria, sería a mis hermanas y mi hermano, aunque él ya no está conmigo; su esencia vivirá en mí para siempre; gracias a ellos, gracias por todo lo que los hermanos pueden hacer en la vida de una persona. A mis dos Fer que han sido apoyo e inspiración, ambos en igual proporción. A mi bebé amada desde el instante en que la vi hasta el último en que la vea, todo esfuerzo será para que ella viva de verdad, que sepa que el límite es el cielo y que no está sola para lograrlo. A mi esposo Fer, que caminó a mi lado, apoyándome incondicionalmente en todas las formas que cuentan cuando fue difícil, y llenó mis días de paz amando cada etapa que he atravesado en esta aventura. A mis amigas que siempre hemos sido apoyo unas de otras en cada fase de nuestra vida. Finalmente, gracias a todo mi aquelarre, a las mujeres fuertes y únicas a las que llamo amigas y a cada mujer en la historia que ha hecho posible que pueda soñar hasta este punto. Muchas gracias. Esta tesis está dedicada a los seres que amo y a todas las mujeres que no pudieron siquiera soñar antes de mí. Que sepan que se pueden lograr los sueños; es difícil, pero se pueden lograr porque juntas llegamos más lejos. A todos y todas, y a cada historia que me acompaña, este final es por todas/os nosotros.

Acknowledgements

I gratefully acknowledge the financial support that made this doctoral research possible. This work was supported by a national scholarship granted by the National Agency for Research and Development (ANID)/Scholarship Program/Doctorado Nacional/2022-21220649, as well as by an additional scholarship provided by Pontificia Universidad Católica de Valparaíso through the 'Beca de término de tesis'. Their support was essential for the successful completion of this PhD program.

I also acknowledge the use of observational data acquired in the HST/COS, obtained through the approved observational proposal 15293 (PI Tejos). I thank the institutions, facilities, and teams involved in the acquisition, reduction, and archiving of these data for making them available to the scientific community.

I would like to express my sincere gratitude to my PhD supervisor, Dr. Nicolás Tejos, for his continuous support throughout the doctoral program. His guidance, insightful discussions, and constructive feedback were fundamental to the development of this work. I am particularly grateful for his careful revisions and valuable comments on the writing, which significantly improved the clarity and quality of the thesis.

Additionally, I would like to extend my deepest gratitude to the thesis committee members for their time, expertise, and dedication in evaluating my work. Your insightful suggestions, constructive critiques, and rigorous feedback were invaluable in shaping and significantly strengthening this research.

Finally, I would like to express my sincere gratitude to all those who contributed directly or indirectly to this research, including collaborators, colleagues, and staff members, whose support and assistance were invaluable throughout the course of this work.

Contents

List of Figures

Abstract

Currently at redshift $z \leq 1$, the ΛCDM paradigm predicts that a significant fraction of baryons is located in the warm-hot intergalactic medium (WHIM), which is most likely located in cosmic web filaments. The WHIM is a low-density (n_H ~10^{-6}-10^{-4} cm^{-3}) plasma with temperatures of ($\log(T/K)$ ~$5-7$) and mild overdensities of ~$10-30$ times the mean density of the Universe. Characterizing the physical state of this dominant baryonic matter and its distribution is crucial because it allows us to complete the physical picture of baryon evolution in the low-redshift Universe.

In the current ΛCDM cosmological framework, matter in the Universe is organized into a complex network known as the cosmic web, composed of galaxy clusters, filaments, sheets, and large underdense voids. Galaxy clusters occupy the densest nodes of this network, while filaments form the interconnected structures along which matter flows under gravity.

Owing to its low density and high ionization state, this gas is most effectively probed through far-ultraviolet (FUV) absorption-line spectroscopy of background quasars, where residual neutral hydrogen and highly ionized metals produce detectable absorption features. Far-ultraviolet absorption-line spectroscopy with the Cosmic Origin Spectrograph instrument in the Hubble Space Telescope (HST/COS) is particularly effective for tracing the warm–hot intergalactic medium (WHIM) at low redshift ($z < 0.5$), where a significant fraction of the cosmic baryons is predicted to reside. In particular, absorption lines of H I Broad Lyα absorbers (BLAs; Doppler parameter $b \geq 40$ km s^{-1}) and O VI have been used as WHIM tracers.

This work focuses on probing the signatures of the WHIM by analyzing the incidence of its tracers, where cosmic web filaments connecting massive galaxy clusters may exist.

We conducted a study of FUV absorption spectroscopy acquired with the HST/COS along QSO sightlines. For this experiment, a sample of ten QSO sightlines at $z \leq 1$ was selected, based on their proximity to cluster-pairs, targeting potential cosmic web filaments that may connect massive galaxy clusters. Nine QSO sightlines were acquired from the observational proposal ID15293 (PI Tejos), designed for our study. The tenth sightline comes from the observational proposal ID12958 (PI Tejos) in the pioneering work of Tejos et al. 2016, which motivates this study. We focus our analysis on absorption

features of WHIM tracers (BLAs and O VI) and cold gas tracers (Narrow Lyα absorbers, or NLAs), which are used as control samples for temperature.

We obtain observational parameters, such as the Doppler parameter, column density (N), and redshift, for each detected absorption line. We measure the incidence and find a relative excess of ~ 1.6, ~ 2, ~ 1.4 and ~ 2.6 for total H I, NLAs ($b < 40$ km s^{-1}), BLAs, and O VI, respectively; within a rest-frame velocity window of $\Delta v = \pm 1000$ km s^{-1} from independent cluster-pairs and within an impact parameter of $\Delta d \leq 3$ Mpc. Additionally, the covering fraction for BLAs and O VI is ~ 1.5 and ~ 2.3 times larger, respectively, than for a random (field) control sample of the environment; while for NLAs, it is consistent with the random expectation. Narrowing the rest-frame velocity window to $\Delta v = \pm 500$ km s^{-1}, we found a covering fraction, for BLAs and O VI, ~ 2.3 and ~ 4.3 times larger than their respective randomly expected values. In contrast, the covering fraction for NLAs remains close to the random expectation, ~ 1.3.

The larger relative excess of WHIM tracers compared to cold gas tracers in the vicinity of independent cluster-pairs indicates that warm-hot gas predominates in that environment, which may be a signature of WHIM detection in inter-cluster filaments.

In this work, we advance on the pioneering work of Tejos et al. 2016, which provided a first statistical assessment of the presence of diffuse gas near cluster-pairs using a single QSO sightline, establishing the experimental design and methodology. In our work, we analyze a survey of ten QSO spectra, a significantly larger sample than the one used in Tejos et al. 2016. We estimate the incidence of O VI and H I sub-samples BLAs, and Narrow Lyα absorbers (NLAs, which are H I features with $b < 40$ km s^{-1}). We aim to probe WHIM signatures by analyzing the incidence of WHIM tracers, targeting putative cosmic web filaments that may connect galaxy cluster-pairs.

This thesis is organized as follows. Chapter 1 provides an overview of the state-of-the-art, outlining the relevant background for this research. Chapter 2 describes the experimental geometry, the data selection and explains the methodology used to characterize the QSO sightlines and used to search for absorption line systems. Chapter 3 indicates the results obtained in the article of Pessa et al. 2025, highlighting the detection of WHIM absorbers and a statistical validation of the method. Chapter 4 presents the results on the incidence of total H I, NLAs, BLAs, and O VI obtained in our survey and a discussion on the incidence and covering fraction of the absorption features analyzed in our survey. Chapter 5 provides a brief introduction to our future work, focused on the overdensities measured in WHIM absorbers. Finally, in Chapter 6, a summary and the conclusions of this study are presented. Here, we use the following cosmological parameters: Hubble constant $H_0 = 67.8$ km s^{-1} Mpc^{-1}, mass energy density $\Omega_m = 0.307$, dark energy density $\Omega_\Lambda = 0.691$, spatial curvature $k = 0$ (Planck Collaboration et al. 2014), and distances are in co-moving coordinates.

List of publications

The research presented in this thesis is based on or makes use of the following publications. These works constitute the primary sources of data, analytical methods, and theoretical frameworks employed throughout the study. They have been cited in the corresponding chapters as appropriate.

1. Ismael Pessa, Nicolas Tejos, **Karen Martinez-Acosta**, Sebastian Lopez, Jessica Werk, and J. Xavier Prochaska, *"A positive correlation between broad H I Lyα absorptions and local overdensities of galaxies"*. https://doi.org/10.1051/0004-6361/202450542.

2. **Karen Martínez-Acosta**, Nicolás Tejos, Ismael Pessa, J. Xavier Prochaska, Britton Smith, Jessica Werk, Nelson Padilla, Sebastián López *in prep.* Tentative title: *"Pinpointing the cosmic web between massive galaxy clusters I: Incidence of H I and O VI as tracers of the WHIM"*.

3. **Karen Martínez-Acosta**, Nicolás Tejos, et al. *in prep.* Tentative title: *"Pinpointing the cosmic web between massive galaxy clusters II: Overdensities of WHIM absorbers"*.

Where relevant, the results, figures, and interpretations derived from these publications have been integrated and further developed in this thesis.

Several parts of this thesis are based on the author's own previously published work, as listed above. Reuse of text, figures, and data from these publications is done in accordance with the copyright policies of the respective publishers.

Chapter 1

Introduction

Chapter based on the article ***Karen Martínez-Acosta****, et al. in prep. Tentative title: "Pinpointing the cosmic web between massive galaxy clusters I: Incidence of H I and O VI as tracers of the WHIM".*

1.1 Intergalactic Medium (IGM)

The intergalactic medium (IGM) is a multiphase ionized gas that constitutes the largest reservoir of baryons in the Universe. It occupies the regions between dark matter halos and surrounds the circumgalactic medium (CGM), which resides outside galaxies but within their host dark-matter halo. The IGM is physically interlinked with the CGM, and its study provides valuable insights about galaxy evolution, star formation, galactic outflows, and the formation of the large-scale structure of the Universe (Sargent et al. 1980, Haardt & Madau 1996, Davé et al. 2001, McQuinn 2016, Mandelker et al. 2019, Hu et al. 2024, Koplitz et al. 2024, Tejos 2025).

At large distances from galaxy halos, the IGM is uniformly distributed and has a typical density significantly lower than that commonly found within galaxies. Indeed, its density is roughly equivalent to a hydrogen atom per four cubic meters, which is comparable to the mean density of the Universe. Under these conditions, particle interactions in the IGM are relatively rare, and photons can travel long distances without interacting. Consequently, the IGM is a diffuse medium, generally considered optically thin, and only its densest constituents are visible. Thus, the properties of the IGM are mainly influenced by large-scale cosmological processes rather than by local interactions (Haardt & Madau 1996, McQuinn 2014, Tejos 2025).

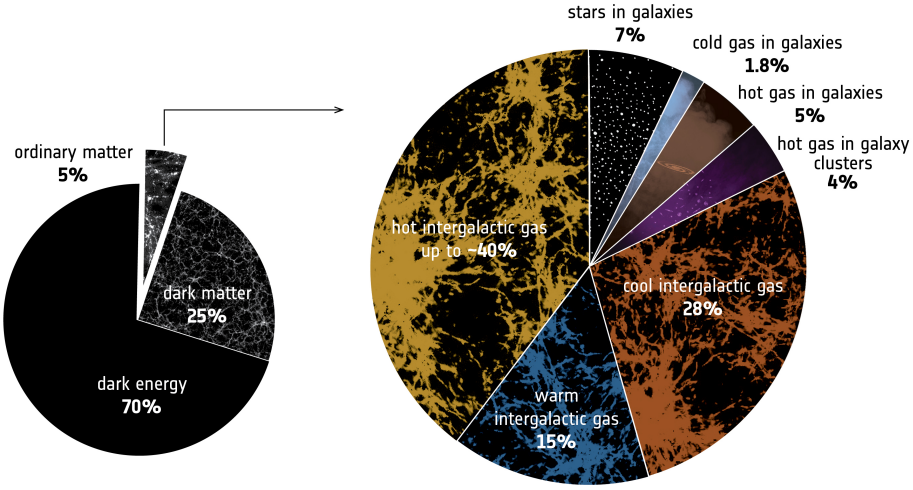

Figure 1.1: Schematic representation of the matter content of the Universe. Dark matter and dark energy make up about 25% and 70% of our cosmos, respectively. Everything we can see, from stars and galaxies to planets, is called ordinary matter, which accounts for only about 5%. It is noteworthy to highlight the dominance of the intergalactic gas over all the rest of the baryons. Credit ESA.

1.1.1 Content of baryonic matter in the Universe

The baryonic matter content in the Universe has been studied across all epochs using models of Big Bang nucleosynthesis (BBN) and the cosmic microwave background (CMB), which predict that only ~4.8% (Planck Collaboration et al. 2016, Pessa et al. 2018) of the energy content in the Universe is in the form of baryonic matter. Figure 1.1 shows a schematic representation of the distribution of the matter content of the Universe, where Dark matter and dark energy account for about 25% and 70% of the Universe, respectively. The ordinary matter makes up stars in galaxies across the Universe, intergalactic gas, and gas in galaxies and galaxy clusters. Everything we can see, from stars and galaxies to planets, is made up of ordinary or baryonic matter, which accounts for only about 5%. It is noteworthy to highlight the dominance of the intergalactic gas over all the rest of the baryons.

Baryonic matter can be categorized into four regimes based on their overdensity ($\delta \equiv \rho/\bar{\rho} - 1$ where $\bar{\rho}$ is the mean baryonic density) and temperature (T) (Davé et al. 2001, Prause et al. 2007). The first regime comprises the largest fraction of baryons that reside in the diffuse IGM with $\delta < 1000$ and $\log(T/K) < 5$, which is photoionized by the metagalactic UV background radiation (Prause et al. 2007, Meiksin 2009). The second regime, with $\delta > 1000$ and $\log(T/K) < 5$, is the condensed regime, which consists of

condensed objects, such as stars and cool galactic gas. The third regime consists of the hot gas ($\log(T/K) > 7$) that is gravitationally bound in galaxy clusters and large groups. The fourth regime consists of the warm-hot intergalactic medium (WHIM), which is a low-density plasma with high temperature (Cen & Ostriker 1999, Davé et al. 2001, Danforth et al. 2010, Savage et al. 2011, D'Odorico 2023).

1.2 Cosmic web

Analyses of structure formation predict a universe interconnected in a complex network of filamentary structures referred to as the 'cosmic web', made of dark matter and diffuse baryons (Bond et al. 1996, Davé et al. 2001, Tepper-García et al. 2012, Tejos et al. 2016, Pessa et al. 2018, Mandelker et al. 2019, Locatelli et al. 2021). In the Λ Cold Dark Matter (ΛCDM) framework, and more generally in hierarchical cosmological models, galaxy clusters correspond to the nodes of the cosmic web, where several filaments converge. In these models, matter is predicted to flow along these filamentary structures, contributing to the mass assembly of galaxy clusters (Bond et al. 1996). A warm-hot intergalactic medium, known as WHIM, is expected to reside mainly in the densest filaments of this cosmic web that connect galaxy clusters (Tejos et al. 2016, Galárraga-Espinosa et al. 2021, D'Odorico 2023, Luber et al. 2025). Cosmological dark matter simulations predict high probabilities of having filamentary structures between close (< 20 Mpc) pairs of massive ($> 10^{14} M_{\odot}$) galaxy clusters (Colberg et al. 2005, Aragón-Calvo et al. 2010, González & Padilla 2010). This probability increases for closer and more massive galaxy clusters, so a natural place to search for WHIM signatures and filaments is the volume between pairs of massive galaxy clusters. In Figure 1.2 we show an illustration of the IGM from the Millennium simulation. This figure depicts the cosmic web, structured by cluster galaxy filaments and expansive, nearly empty voids accounting for most of the cosmic volume.

1.3 Warm-Hot Intergalactic Medium

The WHIM is a low-density ($n_H \sim 10^{-6}$-10^{-4} cm^{-3}) plasma with temperatures of ($\log(T/K) \sim 5-7$) and mild overdensities of $\sim 10-30$ times the mean density of the Universe (Cen & Ostriker 1999, Davé et al. 2001, Prause et al. 2007, Danforth et al. 2010, Savage et al. 2011, D'Odorico 2023, Zhao et al. 2025). The WHIM is believed to emerge from intergalactic gas that is shock-heated to warm-hot temperatures as the medium collapses under gravity (Cen & Ostriker 1999, Davé et al. 2001, Richter et al. 2006b), by cloud–cloud collisions and/or galactic winds (Cen & Ostriker 2006, Cen & Fang 2006).

Cosmological simulations have reproduced and analyzed the formation and dynamics of the filamentary structure of the universe, using different models, such as Millennium

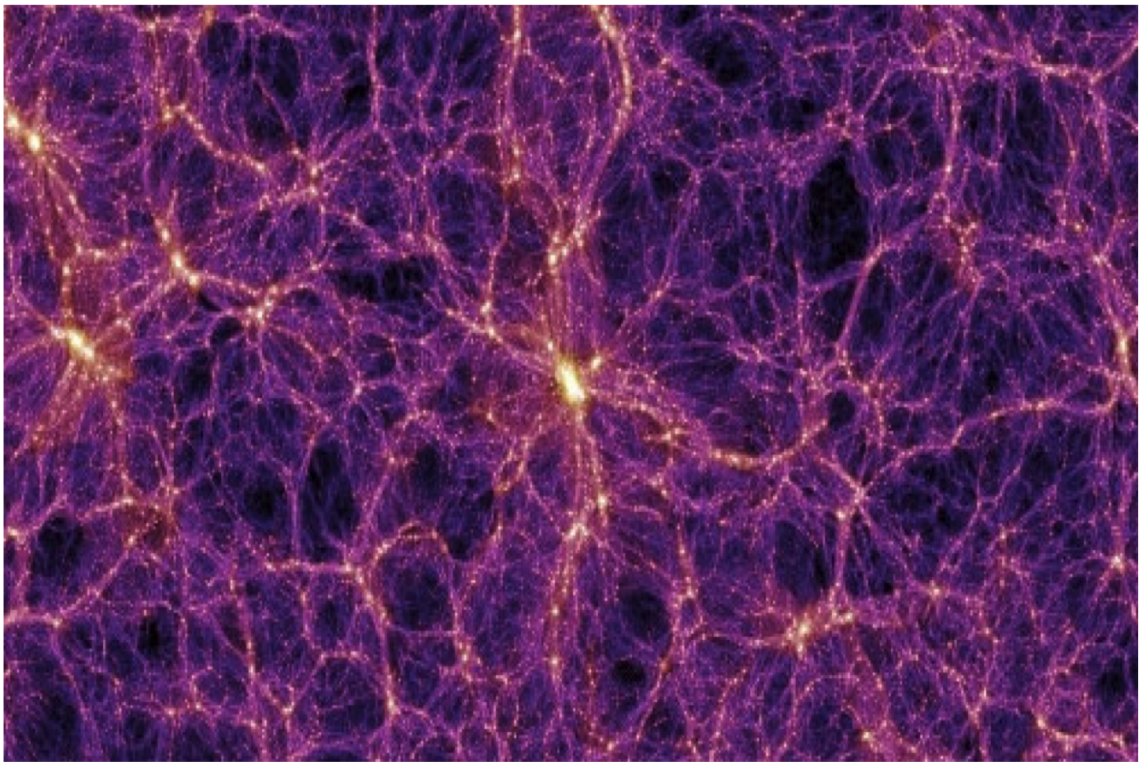

Figure 1.2: Illustration of the cosmic web using dark matter density field simulations from the Millennium simulation. This Figure shows the cosmic web structured by filaments, galaxies, and vast, nearly empty voids, which comprise most of the Universe's volume (Springel et al. 2005a, Farnes et al. 2018).

Simulations (Springel et al. 2005b), Illustris (Vogelsberger et al. 2013, Martizzi et al. 2019), EAGLE (Schaye et al. 2015), and FLAMINGO (Schaye et al. 2023), among many others. From an observational perspective, the filamentary structure of the cosmic web has been a key feature in understanding cosmic evolution (de Lapparent et al. 1986). It has been studied using different multi-wavelength methods. X-ray emission and absorption provide information on the spatial distribution of baryons (Eckert et al. 2015, Nicastro 2016, Reiprich et al. 2021, Tanimura et al. 2022, Zhang et al. 2024, Zhao et al. 2025). Observational techniques such as the thermal Sunyaev–Zel'dovich (tSZ) effect (Bonjean et al. 2018, de Graaff et al. 2019, Tanimura et al. 2020) have been employed to detect the hot phase of the WHIM, mainly around massive halos and galaxy clusters (Yang et al. 2025). These observational studies frequently present statistical significances at the $3-4\,\sigma$ level. However, in some cases, the limited optical and infrared data prevent them from establishing the cosmic environments of these signals (Bonjean et al. 2018). Given its diffuse nature, the WHIM does not emit sufficient photons to be detected in emission (aside from stacking photons from many different regions); thus, absorption-line measurements currently represent the most suitable method for studying the WHIM at low redshifts (Richter et al. 2006b, Savage et al. 2011, Tejos et al. 2016). Particular attention should be drawn to the fact that the highest density of the WHIM is similar to the lowest of the intracluster medium (ICM), in the outskirts of clusters, where it is typically not detected due to low surface brightness.

Figure 1.3 shows a simulation in a Λ-dominated cold dark matter (CDM) universe of the WHIM gas. Contours are color-coded by overdensity; low overdensities of $\rho \sim 10$ are represented in green, while high overdensities of $\rho \sim 10^4$ are represented in red (Davé et al. 2001).

Figure 1.4 shows a phase-space diagram at $z = 0$ of a ΛCDM simulation. This is a density-temperature plot of gas in a representative volume of the Universe. The WHIM region is shown in green dots (Davé 2003).

Due to its high temperature and low density, direct detection of the WHIM is challenging. Nevertheless, understanding this environment is essential to comprehend the local large-scale structure, galaxy feedback, and evolution (Lehner et al. 2007, Prause et al. 2007, Danforth et al. 2010, Richter 2010, Tejos et al. 2016). For instance, a recent work by Macquart et al. 2020 used the dispersion measure of a sample of localized fast radio bursts and measured the baryon content of the Universe to be $\Omega_b = 0.051^{+0.021}_{-0.025} h_{70}^{-1}$. This result implies that the baryons formerly referred to as 'missing' (Cen & Ostriker 1999, Bregman 2007, Shull et al. 2012) are likely to reside in the intergalactic medium (IGM), but it does not reveal their spatial distribution or physical state.

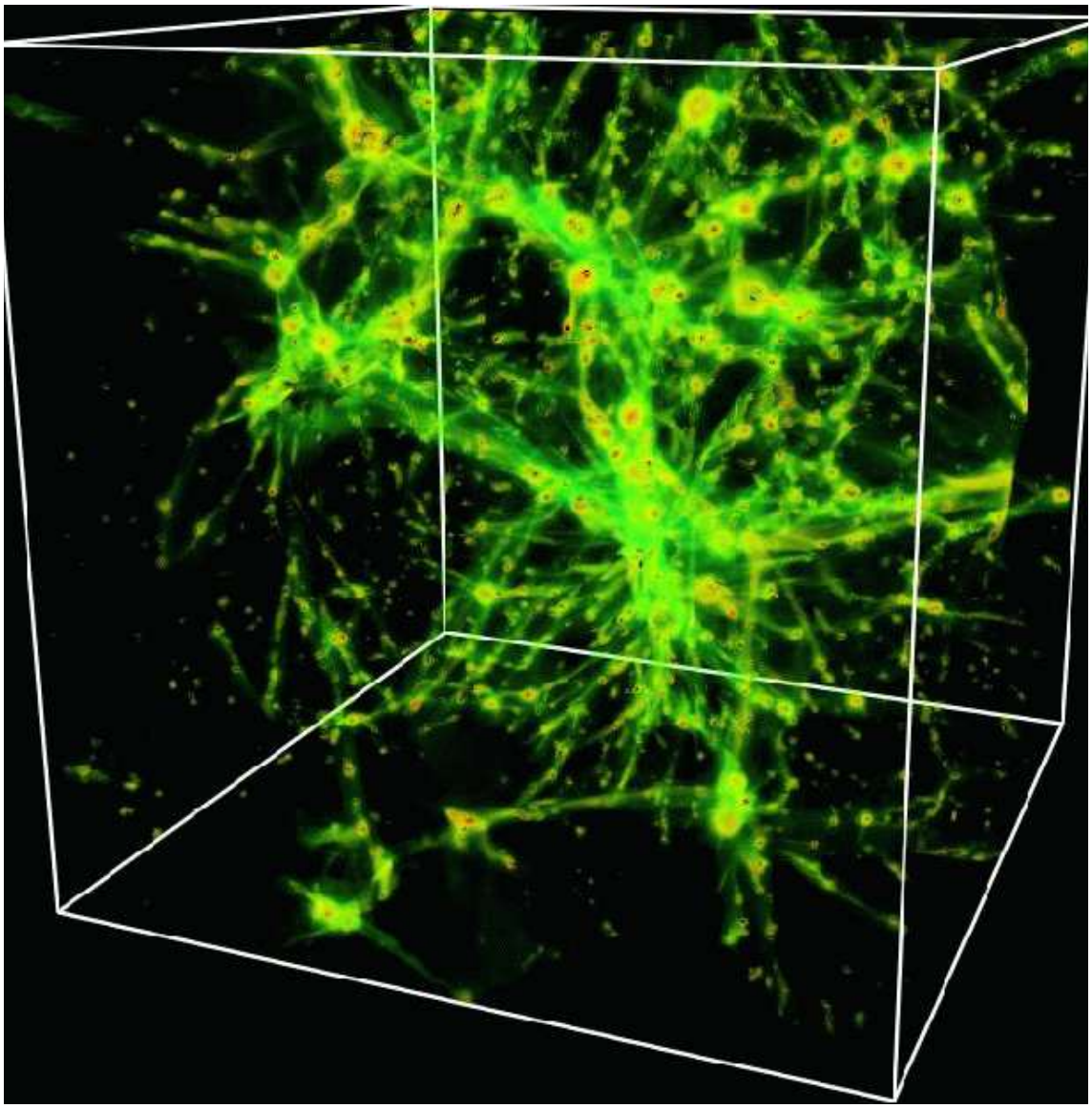

Figure 1.3: Warm - Hot Intergalactic medium (WHIM) simulation in a Λ-dominated cold dark matter (CDM) universe. Low overdensity regions are represented in green and high overdensity regions in red (Davé et al. 2001). Here, the filamentary structure of the WHIM is shown.

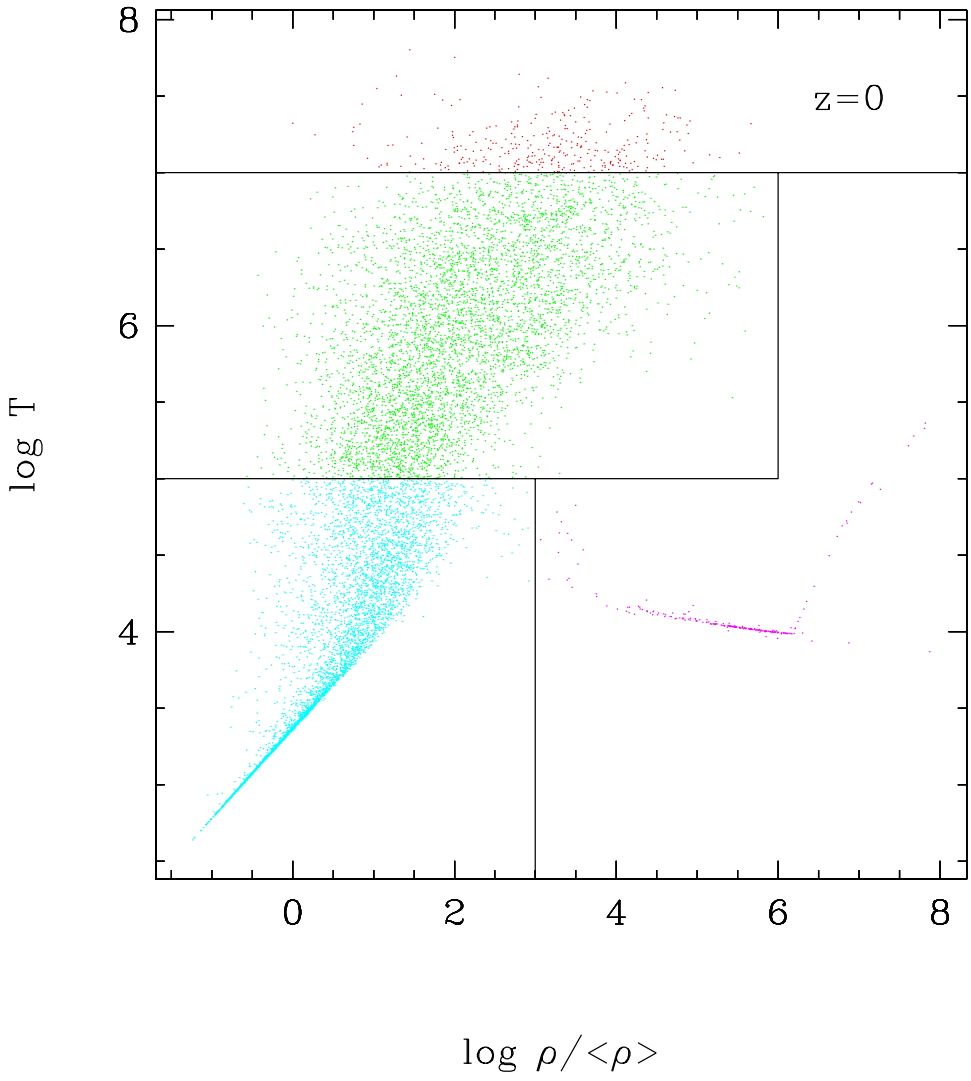

Figure 1.4: WHIM phase diagram at $z = 0$ in a Λ-dominated cold dark matter (CDM) simulation. This is a density-temperature plot of gas in a representative volume of the Universe. The WHIM region is shown in green dots (Davé 2003).

1.4 Far-Ultraviolet spectroscopy absorption

Quasar far ultraviolet (FUV-QSO) absorption spectroscopy is an observational technique that relies on bright background continuum sources, such as QSOs, to identify and characterize intervening absorption features along the sightline. It offers several advantages over attempts to detect gas using emission spectroscopy (Richter et al. 2008, Ahoranta et al. 2020). These include that absorption spectroscopy is more sensitive in a diffuse medium because of its linear dependence on the density of the absorbing gas, in contrast with the density-squared dependence for X-ray emission spectroscopy (Yao et al. 2008). Additionally, absorption lines incorporate kinematic characteristics of the gas, and the ionization state of the gas can be analyzed using multiple ions (Richter et al. 2008, Tepper-García et al. 2012, Tejos et al. 2016). Transitions of H I and O VI have been employed to search for evidence of the WHIM in filamentary structures (Richter et al. 2006b, Tejos et al. 2016, Ahoranta et al. 2020).

Whereas X-ray emission decreases proportionally to density squared, the SZ effect diminishes linearly with electron pressure, meaning that SZ observations have an advantage in detecting the hot gas further into the cluster outskirts over X-ray observations.

Figure 1.5 illustrates a schematic diagram of WHIM detection in FUV. WHIM can be detected at FUV wavelengths primarily through absorption-line spectroscopy of background bright sources, like quasars. The detection relies on identifying weak, intervening absorption features imprinted by highly ionized gas along the line of sight.

1.5 WHIM tracers

The small fraction of H I present in the intergalactic filaments is a metallicity-independent tracer of the WHIM (Danforth et al. 2016). The temperature of a medium affects the Doppler parameter (b) of absorption lines, which is composed of thermal and non-thermal broadening according to $b = \sqrt{b_{\rm th}^2 + b_{\rm non\text{-}th}^2}$.

The thermal component of a line profile can be used to infer the temperature according to $b_{th} = 0.129\sqrt{\frac{T}{A}}$ km s^{-1}, where A is the atomic weight of the element, and T is the gas temperature.

In Figure 1.6, the fraction of neutral hydrogen $f_{\rm H\,I}$ drops sharply as a function of temperature. For BLA temperatures, the fraction of neutral hydrogen is approximately $f_{\rm H\,I} \lesssim 10^{-5}$. For NLAs temperatures ($T < 10^5$ K), the fraction of neutral hydrogen is approximately $f_{\rm H\,I} \gtrsim 10^{-5}$ (Danforth et al. 2010).

The non-thermal component includes turbulence and unresolved blends. In overdense environments, turbulence is expected to be the dominant source of non-thermal physical broadening, and it is considered proportional to the thermal broadening, such that

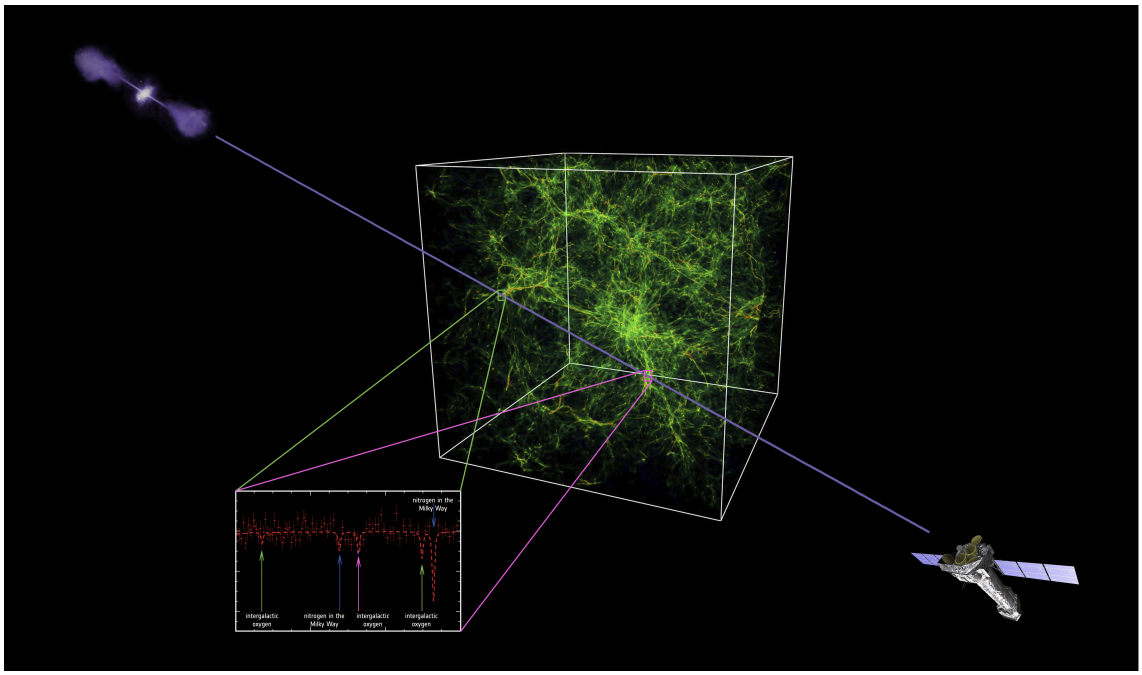

Figure 1.5: Schematic diagram of WHIM detection in FUV. WHIM can be detected at FUV wavelengths primarily through absorption-line spectroscopy of background bright sources, like quasars. The detection relies on identifying weak, intervening absorption features imprinted by highly ionized gas along the line of sight. Credit ESA

$b_{\text{non-th}} \approx b_{\text{turb}} \approx \alpha b_{\text{th}}$ (Pessa et al. 2018, Pessa et al. 2025). In Pessa et al. 2025, they found that absorptions with $b \geq 40$ km s^{-1} trace WHIM at $T > 10^5$ K without a critical dependence on the value adopted for the parameter α, which accounts for the turbulent contribution. Therefore, the identification of broad absorbers is not significantly affected by the assumed level of turbulence, and the condition on the Doppler parameter for broad Lyα absorbers (BLAs, which are H I features with $b \geq 40$ km s^{-1}) is robust with respect to this assumption.

The most important highly-ionized ion (hereafter referred to as "high-ion") absorption line to trace the WHIM at temperatures of $T \sim 3 \times 10^5$ K is O VI. Other high-ion transitions used to probe the WHIM include those of carbon, silicon, nitrogen, and neon. However, these are generally less informative, either because their accessible transitions preferentially trace gas at lower temperatures or because the abundances of these elements in the IGM are too low to yield robust detections (Lehner et al. 2007, Richter et al. 2008, Richter 2010).

Figure 1.7 illustrates the physical conditions of the O VI–bearing gas as a function of the corresponding O VI observables, namely the column density and Doppler parameter. The top-right panel displays the temperatures associated with the O VI–traced gas. Special emphasis should be placed on the top-right panel, which indicates that O VI trace temper-

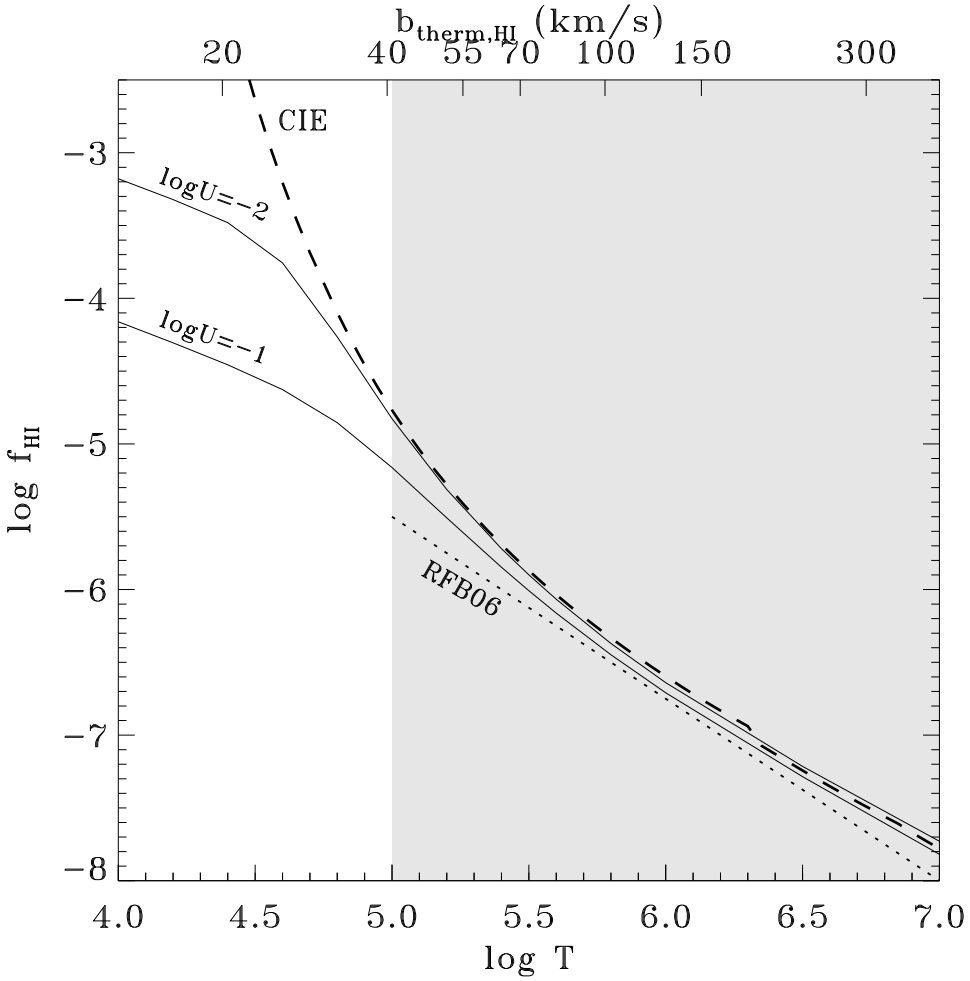

Figure 1.6: Fraction of neutral hydrogen ($f_{\rm H\,I}$) as a function of temperature. At WHIM temperature range ($T = 10^5 - 10^7$ K, shaded region), $f_{\rm H\,I} \lesssim 10^{-5}$. The thermal component of the Doppler parameter for H I is shown on the top axis (Danforth et al. 2010). The lines indicate parametrizations based on Richter et al. 2006a simulations (CIE), linear relationship with log T (RFB06), ionization models from Danforth et al. 2006 ($\log U = -2$ and -1). These models are consistent throughout the WHIM range, but deviate significantly at lower temperatures.

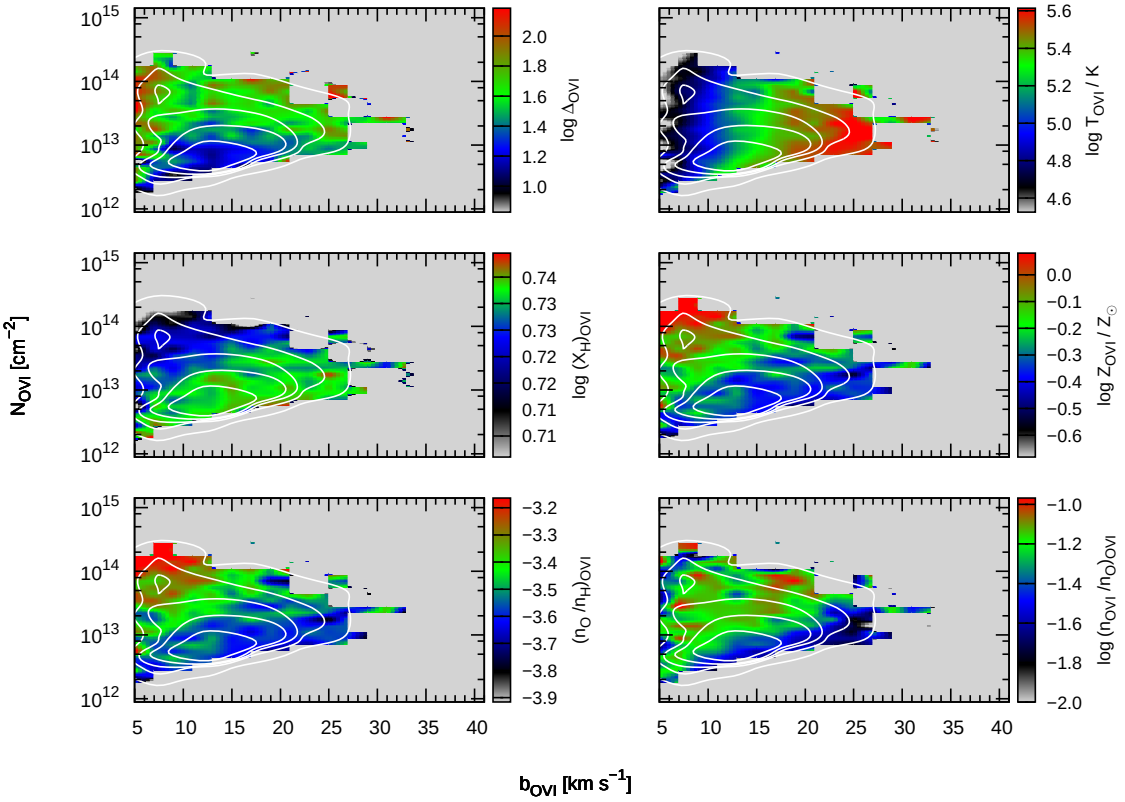

Figure 1.7: Physical conditions of the O VI bearing gas as a function of O VI observables, i.e., column density and Doppler parameter according to a work based on cosmological, hydrodynamical simulations from the OverWhelmingly Large Simulations (OWLS) project. The colour scale shows, for each ($b_{\mathrm{O\,VI}}$, $N_{\mathrm{O\,VI}}$) cell of size $b_{\mathrm{O\,VI}} = 2.0$ km s^{-1} and log $N_{\mathrm{O\,VI}} = 0.2$dex, the median overdensity (top-left), temperature (top-right), hydrogen mass fraction (middle-left), metallicity (middle-right), oxygen abundance (bottom-left) and O VI ionization fraction (bottom-right) (Tepper-García et al. 2011).

atures $T \gtrsim 10^5$ K, for absorptions with Doppler parameter $b > 10$ km s^{-1}. Consequently, it constitutes an effective tracer of the WHIM, regardless of its Doppler parameter.

Many studies suggest that FUV absorption lines of broad Lyα and O VI are reliable tracers the WHIM (Danforth & Shull 2008, Thom & Chen 2008, Tripp et al. 2008). Transitions of H I and O VI have been employed to search for evidence of the filamentary structure of the WHIM in FUV.

1.6 Advances in the current understanding of the WHIM: Contribution of this work

Significant progress has recently been achieved in resolving the long-standing 'missing baryon' problem. Notably, Macquart et al. 2020 utilized the dispersion measures of a sample of localized FRBs to successfully conduct a census of the universe's baryon con-

tent. This approach strongly indicates that the bulk of these elusive baryons resides within the intergalactic medium (IGM) by measuring the integrated column density of ionized matter. However, the detailed spatial distribution and physical state of the gas are largely unconstrained. To directly probe the WHIM —the presumed primary reservoir of these baryons— a variety of complementary observational methods are available. These include X-ray absorption and emission spectroscopy, FUV absorption spectroscopy, and measurements based on the tSZ effect. The aim of this work is to study the WHIM with FUV-QSO spectroscopy to characterize the IGM in putative cosmic web filaments.

Specifically, we advance on the pioneering work of Tejos et al. 2016, which provided a first statistical assessment of WHIM detection in inter-cluster filaments of the cosmic web using a single QSO sightline and established the experimental design and methodology. In our work, we analyze a survey of ten QSO spectra, representing a significantly larger sample than that employed by Tejos et al. 2016. We estimate the incidence of O VI and H I sub-samples BLAs, and Narrow Lyα absorbers (NLAs, which are H I features with $b < 40$ km s^{-1}). We aim to probe WHIM signatures by analyzing the incidence of WHIM tracers (BLAs and O VI) compared to those of cold gas tracers (NLAs), targeting potential cosmic web filaments that may connect massive galaxy clusters.

Chapter 2

Pinpointing the cosmic web between massive galaxy clusters

Chapter based on the article ***Karen Martínez-Acosta****, et al. in prep. "Pinpointing the cosmic web between massive galaxy clusters I: Incidence of H I and O VI".*

To reliably characterize the WHIM in the densest filaments of the cosmic web, we have to identify zones where inter-cluster filaments should reside with high probability. First, we look for pairs of massive galaxy clusters because, according to the ΛCDM framework, galaxy clusters correspond to the nodes of the cosmic web, where several filaments converge. Thus, a natural place to search for WHIM signatures and filaments is the volume between pairs of massive galaxy clusters. To achieve that, we cross-match the galaxy cluster-pairs with bright UV QSOs for feasible FUV spectroscopy. In this work, we identify absorptions along the line of sight of the FUV spectra of a survey of 10 QSOs. Specifically, we analyze the detection of broad and shallow H I, and O VI transitions to provide a robust statistical detection of the elusive WHIM signatures.

2.1 Observational Experiment

We adopt the geometry used in a previous experiment Tejos et al. 2016. In this work, we analyze a survey of ten high signal-to-noise ratio (SNR ∼10) QSO spectra, representing a significantly larger sample than that of the pioneering study, which was based on a single sightline. We estimated the incidence of the signatures of O VI and H I sub-samples Broad Lyα absorbers (BLAs; which are H I features with Doppler parameter $b \geq 40$ km s^{-1}), and Narrow Lyα absorbers (NLAs; which are H I features with $b < 40$ km s^{-1}).

In Figure 2.1, we show a schematic representation of the 3D geometry of our experiment, which is the same as Tejos et al. 2016. Additionally, in Figure 2.2, a diagram of the survey geometry projected in the sky and along the line-of-sight for a single cluster pair

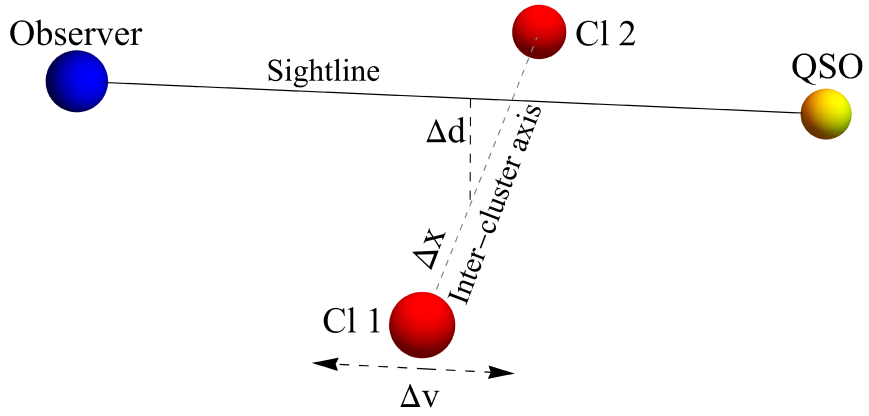

Figure 2.1: Three-dimensional schematic representation of our survey geometry. A cluster-pair that follows our criteria is shown in red. The rest-frame velocity window between the clusters is defined by Δv; the distance between the cluster sightline and the inter-cluster axis is denoted by Δd; and the projected distance between the closest cluster and the QSO sightline is indicated as Δx.

is shown.

2.2 Observational Data

Our experiment needs probing filaments with background QSOs; thus, we require a QSO-filament pair catalog, which is defined by the same methodology of Tejos et al. 2016. First, we used a galaxy cluster catalog to identify cluster-pairs to target the densest filaments in the 'cosmic web' (see Section 2.2.1). Then, we cross-matched these cluster-pairs with a UV bright QSO catalog, and the product of this cross-match is our QSO-filament catalog (see Section 2.2.2). The criteria imposed to select the galaxy clusters and QSO samples are the same as those employed in previous works (Tejos et al. 2016, Pessa et al. 2018, Pessa et al. 2025), summarized as follows.

2.2.1 Galaxy Cluster Catalog and Cluster-pairs

To build our galaxy cluster catalog, we work with the red-sequence Matched-filter Probabilistic Percolation (redMaPPer) catalog from Rykoff et al. 2014, using an extended version and under the restriction of a minimum richness (λ) of 10, which in this redMaPPer catalog corresponds to masses $M_{\rm cluster} \gtrsim 0.8 \times 10^{14} M_{\odot}$.

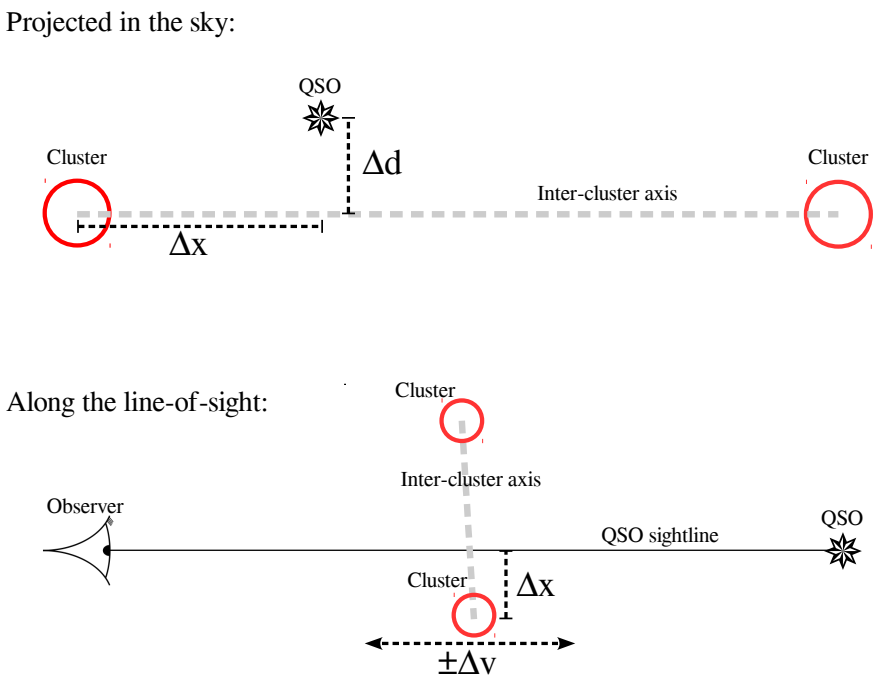

Figure 2.2: Schematic representation of the survey geometry projected in the sky (top) and along the line-of-sight (bottom), for a single cluster pair (Tejos et al. 2016). The cluster pair is represented by two red circles. The intercluster axis is represented by the grey dashed lines. The QSO is represented by the star. Definitions of Δv, Δd, and Δx are identical to those provided in Figure 2.1.

It is important to note that, although lower levels of purity and completeness characterize samples from low-richness clusters (Rykoff et al. 2014), these factors are not expected to generate a spurious signal when comparing the properties of absorption-line systems in environments traced by such cluster-pairs with those in the field, assuming the presence of genuine inter-cluster filaments. Our methodology is inherently conservative, as any impurity or incompleteness would act to attenuate the observed signal, if any, rather than artificially enhance it.

With the richness constraint, our catalog was limited to 251 093 galaxy cluster candidates. Although the redMaPPer detection algorithm is mainly based on photometry, around 50% of the clusters have spectroscopic redshifts from their Brightest Cluster Galaxy (BCG). We use the BCG spectroscopic redshift as the cluster redshift (z) when available; otherwise, we use the photometric redshift.

The criteria that we impose for our cluster-pairs catalog are (for comparison purposes, we adopted the same constraints as those employed by Tejos et al. 2016):

- The redshift of each cluster in a cluster-pair must be within $0.1 \leq z \leq 0.5$ (see Section 2.2.3 for the rationale behind the adopted limits).
- At least one of the two members has to have a spectroscopic redshift determination. If photometric redshift is used, the uncertainty must be no larger than 0.04[1]. Each cluster-pair redshift is assigned as the average redshift between the two cluster members.
- The redshift difference between the clusters of a pair has to be $< 2000\,\mathrm{km\,s^{-1}}$.
- The transverse separation (projected in the sky) between two members of a cluster-pair must be < 25 Mpc.

Using these requirements, we obtained a total of 181 926 cluster-pairs, which we cross-match with our QSO sample.

2.2.2 Selection of QSO sightlines

Our QSO data come from FUV spectroscopic observing programs on the Hubble Space Telescope (HST) with the Cosmic Origins Spectrograph (COS) instrument. The QSOs selected for each program were chosen from the combination of Sloan Digital Sky Survey Data Release 7 (SDSS DR7) (Schneider et al. 2010), the Baryon Oscillation Spectroscopic Survey (BOSS) (Pâris et al. 2012), and the UV-bright Quasar Survey (UVQS)

[1] Although this photometric uncertainty corresponds to large uncertainties in velocity $\delta v \approx 12\,000/(1+z)$ $\mathrm{km\,s^{-1}}$, we note that in most of the cluster-pairs of our sample, both clusters have spectroscopic redshift (see column (8) in Table 2.2). Additionally, for the ones with photometric redshift, most of the uncertainties fall significantly below the adopted threshold, with an average of $\delta z \approx 0.016$).

ID_{QSO}	QSO name	R.A. (deg)	Dec. (deg)	z_{QSO}	Cluster-pair ID	SNR_{QSO}	
						H I	O VI
(1)	(2)	(3)	(4)	(5)	(6)	(7)	
QSO1	J1410+2304	212.65999	23.07977	0.796	1-17	7	10
QSO2	J1456+2750	224.03606	27.83577	0.248	17-24	13	14
QSO3	J1257+4429	194.33150	44.49317	0.300	25-31	10	13
QSO4	J1410+0910	212.72264	9.17416	0.178	32-39	10	13
QSO5	J1419+3739	214.98633	37.65357	0.477	40-45	19	23
QSO6	J1216+1819	184.13986	18.31866	0.449	46-52	10	11
QSO7	J1358+0213	209.59995	2.22885	0.959	53-62	9	13
QSO8	J1210+0154	182.57646	1.90165	0.216	63	14	12
QSO9	J1120+1104	170.08905	11.07633	0.495	64-69	12	10
QSO10	J1637+4254	249.44397	42.91379	0.544	67-77	10	9

Table 2.1: (1) QSO ID. (2) Name of the QSO. (3-4) Location of each QSO. (5) Spectroscopic redshift of the QSO. (6) ID of the cluster-pair (in Table 2.2) associated with each QSO. (7) SNR per resolution element at the wavelength of the independent cluster-pairs in the QSO spectra for relevant absorption features (H I and O VI).

(Monroe et al. 2016) intersecting the volume of SDSS, imposing a magnitude limit of FUV = 18.5 AB. The FUV magnitude of the QSOs was retrieved from GALEX (Bianchi et al. 2014). These comprise a large number of reliably identified QSOs with well-known spectroscopic redshifts, which are bright enough for FUV spectroscopy in relatively short exposure times.

We then cross-matched this UV-bright QSO catalog with our cluster-pairs, imposing the following criteria:

- The redshift of the QSOs must be larger than the redshift of the cluster-pair probed, plus 3000 km s^{-1} (rest-frame) from the QSOs redshift (to avoid the proximity zone of the QSO).
- The QSO sightline must be within 3 Mpc from the inter-cluster axis. This distance is defined as the impact parameter, Δd (see Figure 2.1).

Sightlines cross-matched with at least one cluster-pair were selected for this study, minimizing exposure time per QSO-pair (see proposal ID15293). A total of ten QSO sightlines were analyzed. Nine QSO sightlines were acquired from the observational proposal ID15293 (PI Tejos), designed for our study. The tenth sightline comes from the proposal ID12958 (PI Tejos), published in Tejos et al. 2016. In Table 2.1, we summarize our QSO sample with the intervening cluster-pairs.

It is well known that galaxy clusters tend to be clustered with one another; therefore, cluster pairs should reside within the same structures (White & Frenk 1991, Benson et al. 2001). We therefore grouped the cluster-pairs within 1000 km s^{-1} (rest-frame) from one

another, and we treated these grouped pairs as independent because each group likely traces the same filamentary structures (if any). The velocity value was adopted to account for the velocity dispersion typical of galaxy clusters and the associated contribution to differences in cosmological redshift (Tejos et al. 2016). In this way, we have grouped the 77 cluster-pairs found after the crossmatch with the QSO catalog into 25 independent cluster-pairs. In Table 2.2, we show the galaxy cluster-pairs associated with their respective QSO sightlines.

The majority of the analyzed sightlines have an average SNR greater than 10 per resolution element, at the expected observed wavelength for relevant absorption features (H I and O VI). This constraint corresponds roughly to 3σ detection limits in column density of 10^{13} cm^{-2} for H I and 3×10^{13} cm^{-2} for O VI (Green et al. 2012, Butsky et al. 2019) and it is sufficient for independent constraints of the column density (N) and the Doppler parameter (b) via Voigt profile fitting.

2.2.3 HST/COS Observations

The COS instrument, in its FUV mode, is a spectrograph with medium-resolution ($\lambda/\Delta\lambda \approx 18000$, $\Delta v \approx 17$ km s^{-1}) and wavelength coverage 1135 – 1800 Å. We employed the G130M and G160M gratings, which are the two moderate-resolution FUV channels of COS. Both gratings are sensitive to H I absorption through Lyα at $z < 0.47$ and through Lyβ and higher-order Lyman transitions at $0.1 < z < 0.9$ (Danforth et al. 2016). For O VI, the G130M grating is sensitive to detect at least one transition at $z \gtrsim 0.094$, and the stronger 1032 Å O VI line can be detected at $z \gtrsim 0.100$ (Koplitz et al. 2024). To trace H I and O VI simultaneously at low redshift, in our experiment, we constrain our analysis to $0.1 \leq z \leq 0.5$.

2.2.4 QSOs data processing

We process the QSO spectra in the same fashion as in Pessa et al. 2025, which is briefly described as follows. First, we retrieved the individual exposures of our QSO spectra from the Mikulski Archive for Space Telescopes (MAST). We downloaded the reduced files `x1d.fits`, which had been previously uniformly processed by the HST/CalCOS pipeline (Hodge et al. 2007). CalCOS calibrates COS data by rectifying instrumental effects, producing a wavelength calibration tailored to each exposure, and finally extracting a one-dimensional spectrum calibrated for flux, for the entire observation (James et al. 2022). Nevertheless, we inspected the 2D spectral files to assess the quality of the spectra. Afterwards, we collate the exposures from the available gratings. Since our analysis requires a single linear wavelength scale, we used LINETOOLS[2] (Prochaska et al. 2016) to rebin

[2] https://github.com/linetools/linetools.

Pair ID (1)	QSO (2)	z pair (3)	Transverse (Mpc) (4)	LOS (km s^{-1}) (5)	Δd (Mpc) (6)	Δx (Mpc) (7)	Both spec-z? (8)	Grouped ID (9)
1	J1410+2304	0.15426	22.1	1952	0.6	0.1	y	1
2	J1410+2304	0.15883	14.7	420	0.5	0.3	y	2
3	J1410+2304	0.17598	14.7	1381	1.5	7.3	y	3
4	J1410+2304	0.34387	12.7	1192	1.8	3.4	y	4
5	J1410+2304	0.34761	24.8	1318	2.8	7.5	n	4
6	J1410+2304	0.34884	18.1	1022	2.3	9.0	y	4
7	J1410+2304	0.3743	17.4	771	2.8	4.6	n	5
8	J1410+2304	0.41487	5.3	435	1.9	2.0	y	6
9	J1410+2304	0.41631	16.7	1044	1.2	3.6	y	6
10	J1410+2304	0.41688	23.6	1287	0.0	3.8	y	6
11	J1410+2304	0.41707	13.2	1365	2.6	2.8	n	6
12	J1410+2304	0.43206	17.9	1583	2.6	6.0	n	7
13	J1410+2304	0.45491	4.1	1362	0.4	1.2	n	8
14	J1410+2304	0.45508	10.8	1430	2.8	0.8	n	8
15	J1410+2304	0.45838	11.1	68	1.0	0.7	y	8
16	J1410+2304	0.45988	16.2	682	1.2	0.2	y	8
17	J1410+2304	0.46019	21.9	807	1.0	0.7	y	8
18	J1456+2750	0.12462	12.6	881	0.6	5.2	n	9
19	J1456+2750	0.12588	17.6	207	0.9	5.2	y	9
20	J1456+2750	0.12628	10.2	5	1.6	5.0	y	9
21	J1456+2750	0.17993	15.0	312	3.0	3.5	y	10
22	J1456+2750	0.22637	7.5	24	0.8	0.8	y	11
23	J1456+2750	0.22656	15.7	116	0.8	0.8	y	11
24	J1456+2750	0.22687	9.1	267	1.0	0.4	y	11
25	J1257+4429	0.2319	12.5	687	1.8	3.2	n	12
26	J1257+4429	0.23287	17.2	32	2.3	8.1	y	12
27	J1257+4429	0.23306	11.6	123	1.7	3.3	y	12
28	J1257+4429	0.23518	21.6	1087	2.9	8.9	y	12
29	J1257+4429	0.23526	22.2	947	2.4	2.8	y	12
30	J1257+4429	0.23536	16.5	996	1.1	3.5	y	12
31	J1257+4429	0.23591	24.0	1506	2.2	8.2	n	12
32	J1410+0910	0.10781	13.2	390	1.4	3.6	y	13
33	J1410+0910	0.10817	18.7	196	1.6	3.5	y	13
34	J1410+0910	0.10868	23.2	84	2.0	3.3	y	13
35	J1410+0910	0.10889	22.9	197	2.0	3.3	y	13
36	J1410+0910	0.11097	13.7	1315	0.5	3.8	y	13
37	J1410+0910	0.11178	16.1	1751	0.1	3.8	y	13
38	J1410+0910	0.11194	22.9	791	2.6	9.7	y	13
39	J1410+0910	0.14801	25.0	1341	1.9	5.1	y	14
40	J1419+3739	0.13551	1.8	323	2.5	0.3	y	15
41	J1419+3739	0.13683	16.0	1017	2.7	1.1	y	15
42	J1419+3739	0.15687	11.2	766	1.0	5.4	y	16
43	J1419+3739	0.15889	17.1	1812	2.9	4.7	y	16
44	J1419+3739	0.15985	13.9	775	2.3	5.4	y	16
45	J1419+3739	0.16187	21.1	270	2.4	8.5	y	16
46	J1216+1819	0.15306	22.0	1342	1.2	8.0	y	17
47	J1216+1819	0.15556	11.2	39	1.6	3.3	y	17
48	J1216+1819	0.18143	6.2	798	2.3	0.5	y	18
49	J1216+1819	0.18237	21.9	1274	0.3	6.2	y	18
50	J1216+1819	0.18394	16.2	477	2.3	0.6	y	18
51	J1216+1819	0.1866	6.7	1820	0.3	2.3	y	18
52	J1216+1819	0.31771	24.7	1455	1.8	9.8	y	19
53	J1358+0213	0.25746	13.2	473	1.7	5.7	y	20
54	J1358+0213	0.26055	20.9	481	2.0	5.5	y	20
55	J1358+0213	0.2612	11.0	169	1.4	5.4	y	20
56	J1358+0213	0.26136	20.8	246	0.3	5.5	y	20
57	J1358+0213	0.26209	16.8	255	1.5	5.6	y	20
58	J1358+0213	0.26425	17.7	1615	0.2	5.5	n	20
59	J1358+0213	0.26514	23.4	1191	1.0	11.2	n	20
60	J1358+0213	0.43152	11.9	714	2.0	1.8	n	21
61	J1358+0213	0.43522	19.9	833	1.5	2.3	n	21
62	J1358+0213	0.4353	19.4	865	2.0	1.8	n	21
63	J1210+0154	0.19083	13.0	1242	1.1	5.7	y	22
64	J1120+1104	0.24151	20.7	484	2.8	7.5	y	23
65	J1120+1104	0.24219	14.3	814	0.4	6.3	y	23
66	J1120+1104	0.24322	19.2	317	1.1	6.2	y	23
67	J1120+1104	0.38859	19.8	500	1.1	2.5	n	24
68	J1120+1104	0.38862	20.1	490	1.6	2.2	n	24
69	J1120+1104	0.39072	17.4	1419	1.1	0.0	y	24
70	J1637+4254	0.22277	15.5	512	1.9	4.8	y	25
71	J1637+4254	0.22366	15.2	773	2.5	6.6	y	25
72	J1637+4254	0.22372	18.6	802	1.2	8.8	y	25
73	J1637+4254	0.22453	12.2	349	0.6	5.1	y	25
74	J1637+4254	0.22459	14.9	378	0.7	5.1	y	25
75	J1637+4254	0.22521	19.0	1705	1.5	8.1	y	25
76	J1637+4254	0.22697	15.4	845	0.1	7.1	y	25
77	J1637+4254	0.22703	17.7	816	1.9	8.0	y	25

Table 2.2: (1) Pair ID. (2) QSO associated with a cluster-pair. (3) Redshift of the cluster-pair. (4) Transverse separation between cluster-pairs. (5) Separation between the cluster-pairs in rest-frame velocity along the QSO sightline (LOS). (6) Impact parameter (Δd). (7) Distance to the closest cluster of the pair, along the inter-cluster axis (Δx). (8) Whether both members of a cluster-pair have spectroscopic redshift. (9) Grouped independent cluster-pairs.

the original spectra into a coarser one of 0.0395 Å pixel^{-1}, which corresponds roughly to two pixels per resolution element (Tejos et al. 2016). In spectral regions covered by both gratings, we average the spectra with the `smash_spectra` function from LINETOOLS which ensures the conservation of total flux in the process. The calibrated one-dimensional final spectra were further analyzed using the LINETOOLS `lt_continuumfit` script to fit a global pseudo-continuum to it[3].

2.3 Quality of the survey

Figures 2.3 and 2.4 show the SNR of the spectra of the QSO sightlines of our survey. In each sightline, the colored regions belong to the expected observed wavelength for H I (Figure 2.3, in brown) and O VI (Figure 2.4, in green) absorptions, at the location of independent cluster-pairs.

2.4 Spectral lines identification

We search for intervening absorption lines in each QSO spectrum and characterize their observational parameters via Voigt profile fitting. We focus our analysis on total H I, NLAs, BLAs, and O VI absorption lines.

We first identify all the absorption lines in every QSO sightline using the software IGM-Guesses[4], not only in the wavelength regions corresponding to the redshifts of known structures. This software is a graphical user interface (GUI) available as part of the PYIGM package[5] and facilitates the search for and identification of absorption features in the spectra of background sources. However, IGM-Guesses only produces initial guesses for the redshift, column density, Doppler parameter, and ion identification for subsequent Voigt profile fitting.

To characterize all absorption lines, we followed the algorithm described in Tejos et al. 2016 (see also Holguin Luna et al. 2024 and Pessa et al. 2025), which is summarized as follows.

First, we must specify a confidence category for identifications. We do this through qualitative categories that indicate the reliability of the detection. Category 'a' (reliable) is assigned to the detections with multiple transitions of a given ion where at least two of them are available and clearly visible in the spectrum. Category 'b' (possible) is assigned when we have absorption components from single transition ions that are at the

[3] i.e., including intrinsic broad emission lines and Galaxy's damped Lyα system wings (Tejos et al. 2016).

[4] https://pyigm.readthedocs.io/en/latest/igmguesses.html.

[5] https://github.com/pyigm/pyigm.

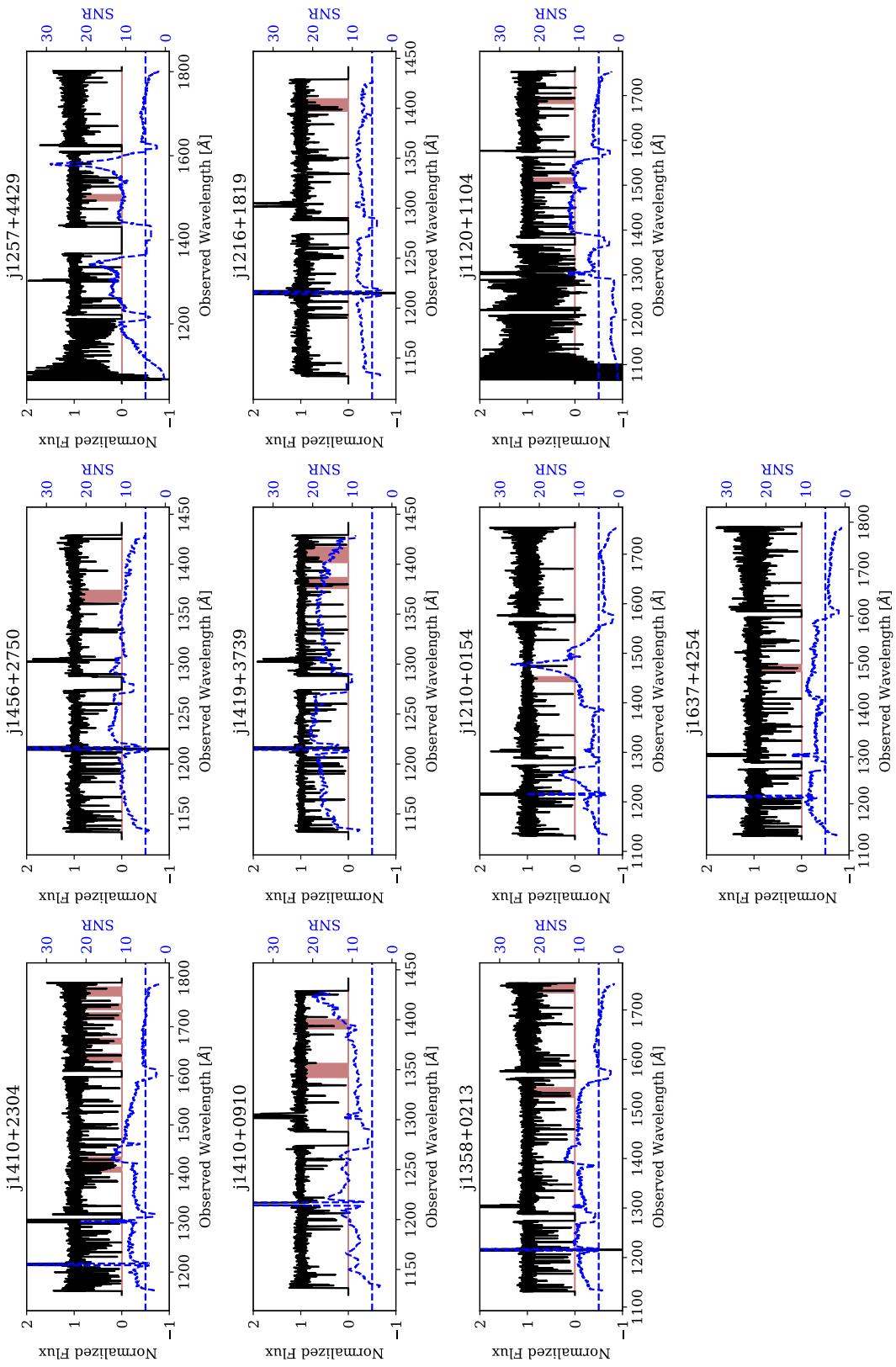

Figure 2.3: The SNR is shown in blue (values shown on the rightward y-axis) to indicate the quality of the spectra (shown in black) of our survey for H I. The straight blue-dashed line corresponds to an SNR = 5. The regions where the independent cluster-pairs are located in the spectra for the H I are shown in brown.

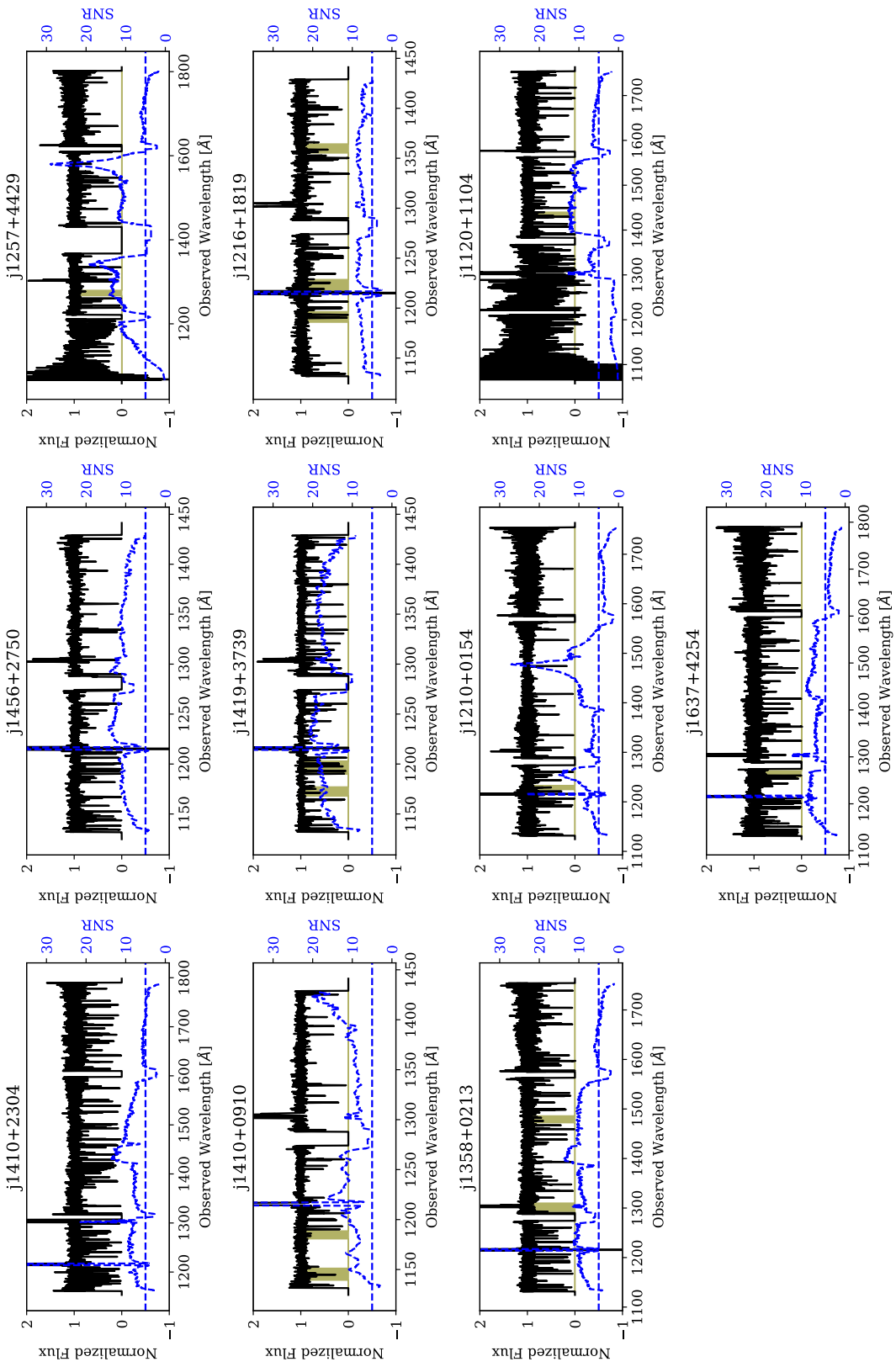

Figure 2.4: The SNR is shown in blue (values shown on the rightward y-axis) to indicate the quality of the spectra (shown in black) of our survey for O VI. The straight blue-dashed line corresponds to an SNR = 5. The regions where the independent cluster-pairs are located in the spectra for the O VI are shown in green.

same redshift as another certain component or when ion components have several possible transitions, but for some reason, only one of them is clearly detected. Category 'c' (uncertain) is initially assigned when components, based on the user experience, are likely to be misidentified or to exhibit an unknown feature. Additionally, we imposed a detection significance criterion based on the equivalent width (W_r) and its uncertainty (δW_r). Absorptions with reliability 'b' with $W_r/\delta W_r < 3$ are reassigned to reliability 'c'.

With these criteria, we use the 5-step IGM-Guesses algorithm (Tejos et al. 2016):

1. Step 1: We identify all absorption components available at redshift $z = 0$ with a velocity window of ± 500 km s^{-1} in order to ensure the identification of the lines from the interstellar medium (ISM) of the Milky Way and/or Local Group Systems.

2. Step 2: This step replicates Step 1, but at the redshift of the QSO (z_{QSO}) with a velocity window of ± 1500 km s^{-1} to ensure the identification of the lines associated with the QSO environment.

3. Step 3: We search for absorption lines from the IGM. To do so, we identify H I with at least two transitions, starting at $z = z_{QSO}$ and scanning down to $z = 0$, and assign them to the reliability 'a'. This step involves identifying the entire Lyman series covered by the spectrum of a given component.

4. Step 4: We search for metal lines in the well-identified H I absorption detected in the previous step. When the wavelength coverage allows detection of multiple transitions of a single ion, we require that their relative positions coincide; in cases of multiple adjacent components blending, we require them to have consistent kinematic structures across multiple transitions of the same ion.

5. Step 5: We assume all unidentified absorption features to be H I Lyα starting from $z = z_{QSO}$ down to $z = 0$, and assign them to the 'b' category. Then we repeat the previous step, and if metal lines are found, we re-assign the corresponding identification and reliability, and categorize the H I line as category 'a'.

Finally, we save these absorption features and the initial guesses on (z, N, b).

2.4.1 Observational parameters estimation

We use the VEEPER[6] Voigt profile fitting software based on our initial guesses described above. Veeper is a collection of tools for generating and fitting Voigt profiles of absorption lines, particularly in QSO spectra, accounting for the non-Gaussian line spread function

[6] https://github.com/jnburchett/veeper

(LSF) of COS. We fit Voigt profiles to all absorption lines in the QSO spectrum, yielding definitive values for z, $\log N$, and b, along with their uncertainties.

With the results from the Voigt profile fitting, we estimate the rest-frame equivalent width of the strongest transition for each detected component with LINETOOLS. For this purpose, we used the approximation based on fitted values for N and b, as given by Draine 2011 (see their equation 9.27). Its uncertainty was calculated as in Tejos et al. 2016 (see their Section 4.3). It is of particular importance to recognize that for saturated lines, our method leads to unrealistically large δW_r due to the poor column density constraint, but these lines are usually in the 'a' category.

2.5 Methodological Context Within This Work

The methodology presented in this chapter was previously validated within the framework of a collaborative study based on the analysis of a single sightline toward QSO SDSSJ161940.56+254323.0, which constitutes the focus of Chapter 3. In that work, the procedures described here were implemented and tested to ensure their robustness and internal consistency.

Furthermore, both the methodological approach and the dataset detailed in the present chapter form the foundation of the central component of this thesis, corresponding to the article currently in preparation (*Pinpointing the cosmic web between massive galaxy clusters I: The incidence of H I and O VI*). The results derived from this application, together with their associated analysis and discussion, are presented comprehensively in Chapter 4.

Chapter 3

A positive correlation between broad H I Lyα absorptions and local overdensities of galaxies

Chapter based on the article of Pessa et al. 2025, et al.: A positive correlation between broad H I Lyα absorptions and local overdensities of galaxies

This chapter outlines the contributions of the Ph.D. candidate to the aforementioned article; however, it does not present the results in their entirety. The purpose of this chapter is to highlight the specific aspects to which the candidate contributed, which focused on the methodology for detecting absorption lines in the sightline of QSO SDSSJ161940.56+254323.0, the detection and characterization of intervening gas absorption features, and the statistical validation of the identified detections.

Particularly, for a subset of the BLAs identified in this spectrum, we apply the Bayesian Information Criterion (BIC) to compare alternative candidate best-fit models for the associated absorption features. In addition, we provide a detailed discussion of the treatment and characterization of saturated BLAs.

It is important to note that, in this Chapter, only a single sightline was used. In contrast, the full study includes 10 characterized sightlines (see Chapter 4), resulting in a more robust sample. This chapter also serves to validate the absorption-line detection methodology applied throughout the broader study.

3.1 Overview

A large fraction of the baryon budget at $z < 1$ resides in large-scale filaments in the form of diffuse intergalactic gas, and numerous studies have reported a significant correlation between the strength of the absorptions produced by this gas in the spectra of bright

background sources and the impact parameter to cosmic filaments intersected by these sightlines (Wakker et al. 2015, Tejos et al. 2016, Pessa et al. 2018, Bouma et al. 2021, Vernstrom et al. 2021). However, a similar relation is harder to determine for the warm-hot phase of the intergalactic gas, since its higher Doppler parameter and significantly lower neutral gas fraction make this gas difficult to detect in absorption; thus, high-quality spectra are required.

We use a sample of 13 broad Lyα absorbers (BLAs) detected in the HST/COS spectrum of a single QSO ($z \sim 0.2685$), whose sightline intersects several inter-cluster axes, to study the relation between BLAs and the large-scale structure of the Universe. Given their Doppler parameters of $b > 40\,\mathrm{km\,s^{-1}}$, BLAs are good tracers of warm-hot intergalactic gas.

Local overdensities of galaxies at the redshifts of the BLAs were inferred from VLT/MUSE and VLT/VIMOS data to assess the potential association of the BLAs with nearby galaxies (see Pessa et al. 2025 for further details). Out of the 13 BLAs identified in our sample, four are associated with a strong overdensity of galaxies, and four with tentative overdensities. The remaining five are located at redshifts where an excess of galaxies was not identified. These overdensities of galaxies at the redshift of BLAs ($\pm 1000\,\mathrm{km\,s^{-1}}$) are local, and they vanish when larger cosmic volumes are considered, in terms of a larger velocity offset to the BLA or larger impact parameter to the QSO sightline. See Pessa et al. 2025 for further details.

Finally, in this work, we find a positive correlation between the total hydrogen column densities inferred from the BLAs and the relative excess of galaxies at the same redshifts, consistent with the picture where warm-hot gas resides deep within the gravitational potential well of cosmic filaments. However, this chapter does not focus on the determination of overdensities from the galaxy survey. Instead, it concentrates on the methodology employed to identify absorption features in QSO spectra, the statistical validation of the fitting procedure used to characterize these features, and the derivation of observational parameters from the resulting fits.

3.2 Detection of BLAs

In this section, we present the methodology employed for the identification of absorption lines in the SDSSJ161940.56+254323.0 normalized spectrum, and describe how we deal with possible ambiguities. The characterization of the absorption lines in the spectrum of SDSSJ161940.56+254323.0 of the HST/COS was carried out throughout the full line-of-sight, not only limiting ourselves to the regions where known structures exist. In this way, we minimize possible misidentifications and better handle possible interloper absorption.

We employ the same criteria to identify and characterize these absorption features

as in Tejos et al. (2016) (see their section 4 for details). For this, we used the custom software `IGM_guesses`[1]. This software facilitates the visualization and Gaussian fitting of absorption features, ultimately yielding initial parameters for subsequent Voigt profile fitting (see below); these include redshift (z), column density (N), and Doppler parameter (b) for the ions identified.

To characterize absorption lines in the QSO SDSSJ161940.56+254323.0, we applied the 5-step IGM-Guesses algorithm described in 2.4.

Later, we used these initial guesses as inputs for an automatic Voigt profiling process using the software VEEPER [2], taking into account the non-Gaussian COS line spread function (LSF) and restricting the sample to absorption lines having $W_r > 0.01$ Å.

From this analysis, we obtained a sample of 13 identified reliable BLAs for which we measured their redshift, neutral hydrogen column density $N_{\rm HI}$, and Doppler parameter $b_{\rm HI}$. In this work, we identify as BLA any hydrogen absorption with an observed Doppler parameter larger than $40\,{\rm km\,s^{-1}}$ (see, e.g., Danforth et al. 2010, 2016), however, we acknowledge that due to the presence of non-thermal broadening, a $b > 40\,{\rm km\,s^{-1}}$ does not necessarily always imply gas at $T \gtrsim 10^5$ K (see, e.g., Sameer et al. 2024). These BLAs are shown in Fig. 3.1. When characterizing absorption lines, there is always the possibility of introducing biases and/or systematics.

Table 3.1 summarizes the physical properties of the gas inferred from each one of the BLAs in our sample. While this work focuses primarily on BLAs, for completeness and comparison purposes, we also proceed in the same manner with the detected NLAs. Table 3.2 summarizes the physical properties of the gas derived for the NLAs. In total, ten NLAs (and zero BLAs) fall in the low-reliability category 'c'. These transitions were excluded from further analyses. For further details in the calculation of each column of Tables 3.1 and 3.2, see Pessa et al. 2025.

3.2.1 Statistical validation of the detection method

BLAs modeled as a single absorption could alternatively be modeled as multiple narrow components. To choose the best model, while avoiding overfitting, we use the Bayesian information criterion (BIC).

The BIC quantifies the goodness of fit of a model while explicitly penalizing the model complexity. Thus, balancing the likelihood of the data given the model and the number of free parameters. The BIC imposes a penalty that increases with the number of model parameters to avoid overfitting. Models with lower BIC values are preferred (Schwarz 1978).

[1] https://github.com/pyigm/pyigm.
[2] https://github.com/jnburchett/veeper.

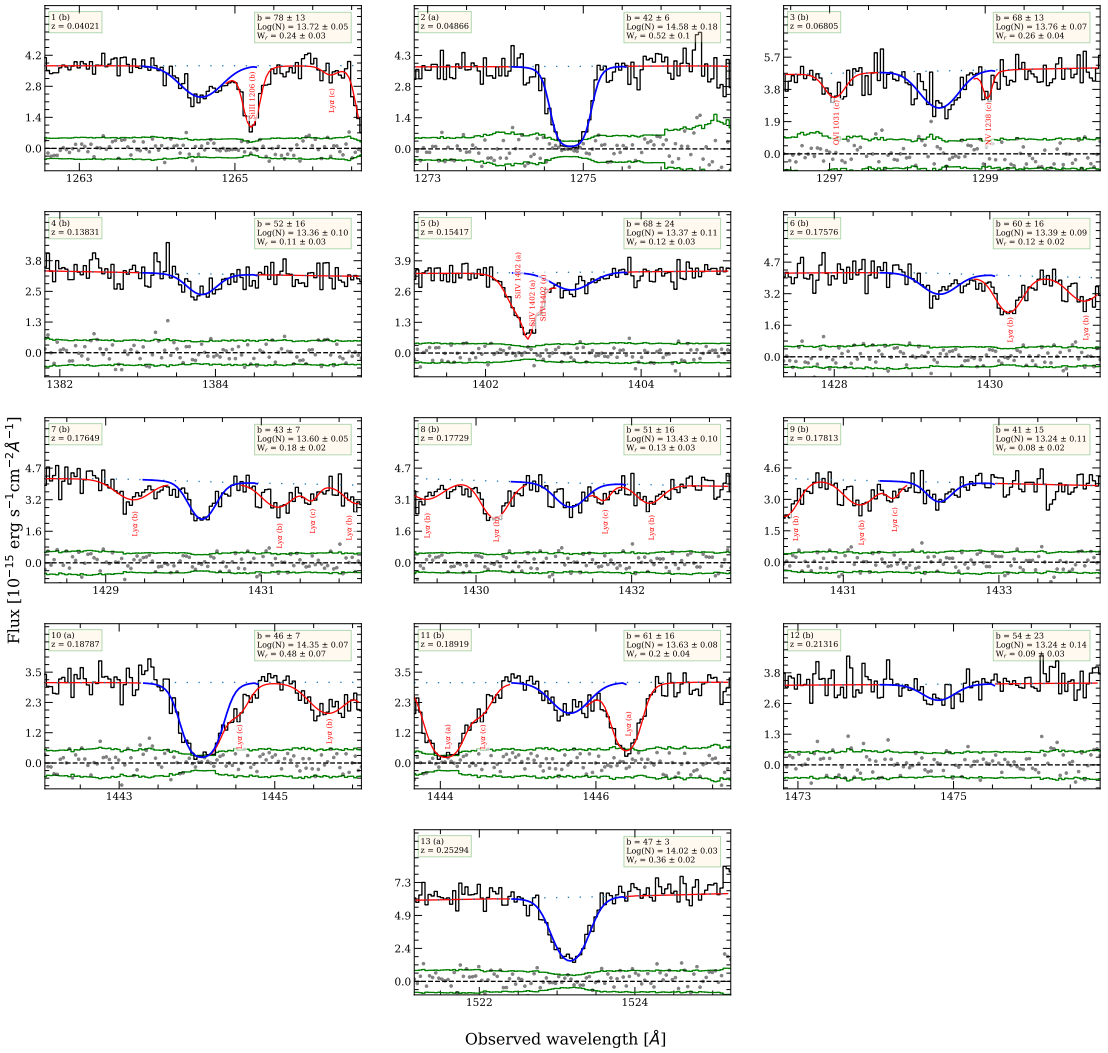

Figure 3.1: Identified BLAs in the HST/COS spectrum of SDSSJ161940.56+254323.0. The panels show the best-fitting Voigt profile for each BLA in blue and the full model of the QSO spectrum in red. The dotted line shows the continuum level. Additional modeled transitions in the same wavelength range are labeled in red. The derived observational parameters column density $\log(N/\mathrm{cm}^{-2})$, Doppler parameter in km s^{-1}, equivalent width in Å, and redshift are indicated in each panel, together with the reliability of the identification (see Sec. 3.2 for details). For saturated lines, our method leads to unrealistically large W_r uncertainties due to the poor column density constraint.

ID	z	b/km s^{-1}	log($N_{\rm H\,I}$ / cm^{-2})	log($N_{\rm H\,II}$ / cm^{-2})	Δlog(N$_{\rm H\,II}$/ cm^{-2})	Δlog(T/K)	Δlog $f_{\rm ion}$	Reliability	Metals
(1)	(2)	(3)	(4)	(5)	(6)	(7)	(8)	(9)	(10)
1	0.04021	78±13	13.72±0.05	19.71±0.18	19.93 - 19.29	5.6 - 5.1	6.21 - 5.57	b	-
2	0.04866	42±6	14.58±0.18	19.90±0.24	20.11 - 19.47	5.0 - 4.5	5.53 - 4.89	a	Si III, Si IV, C IV
3	0.06805	68±13	13.76±0.07	19.60±0.22	19.82 - 19.18	5.4 - 4.9	6.06 - 5.42	b	-
4	0.13831	52±16	13.36±0.10	18.90±0.36	19.11 - 18.47	5.2 - 4.7	5.75 - 5.11	b	-
5	0.15417	68±24	13.37±0.11	19.20±0.40	19.42 - 18.78	5.4 - 4.9	6.05 - 5.41	b	-
6	0.17576	60±16	13.39±0.09	19.09±0.30	19.31 - 18.67	5.3 - 4.8	5.92 - 5.28	b	-
7	0.17649	43±7	13.60±0.05	18.93±0.18	19.15 - 18.51	5.0 - 4.5	5.55 - 4.91	b	-
8	0.17729	51±16	13.43±0.10	18.97±0.36	19.18 - 18.54	5.2 - 4.7	5.75 - 5.11	b	-
9	0.17813	41±15	13.24±0.11	18.54±0.41	18.75 - 18.11	5.0 - 4.5	5.51 - 4.87	b	-
10	0.18787	46±7	14.35±0.07	19.75±0.17	19.97 - 19.33	5.1 - 4.6	5.62 - 4.98	a	O VI
11	0.18919	61±16	13.63±0.08	19.35±0.30	19.57 - 18.93	5.4 - 4.8	5.94 - 5.30	b	-
12	0.21316	54±23	13.24±0.14	18.82±0.48	19.03 - 18.39	5.2 - 4.7	5.79 - 5.15	b	-
13	0.25294	47±3	14.02±0.03	19.47±0.08	19.68 - 19.04	5.1 - 4.6	5.66 - 5.02	a	-

Table 3.1: Physical properties of the gas inferred from each one of the BLAs in our sample. Columns (1)-(4) indicate ID of the identification, redshift (z), Doppler parameter (b), and neutral hydrogen column density (log $N_{\rm H\,I}$), respectively. The ionized hydrogen column densities (log $N_{\rm H\,II}$) in column (5) have been calculated using a constant α (turbulent-to-thermal Doppler contribution ratio) of 0.7. The uncertainties in column (5) reflect only the statistical uncertainties propagated from the line fitting. However, the inferred ionized hydrogen column densities are subject to systematic uncertainties due to the assumptions made to compute them. Columns (6), (7), and (8) show the range of variation of the determined log($N_{\rm H\,II}$), log(T), and ionization fraction of the gas ($f_{\rm ion}$), respectively, when using α values in the range [$\alpha_{\rm low}$ - $\alpha_{\rm high}$], with $\alpha_{\rm low}$ = 0, and $\alpha_{\rm high}$ = 1.5. Column (9) shows the reliability of the Voigt profile fitting, and column (10) indicates the metal transitions found at the same redshift of each BLA.

In Figures 3.2-3.4, we discuss possible alternative best-fitting solutions for some of the BLAs in our sample. For some of the BLAs identified in our analysis, models incorporating multiple absorption components were compared against single-component models.

The BLA #1 ($z \sim 0.04021$, see Figure 3.2) could be alternatively modeled as three separate narrow components. Naturally, this could potentially reproduce the data better than our one-component fitting. Thus, to choose the best model, while avoiding overfitting, we use the Bayesian information criterion (BIC), which introduces an additional penalty term for the number of parameters in the model (Schwarz 1978) [3]. For this BLA, the BIC is significantly lower for the one-component fitting, and thus, a one-component model is the preferred solution.

The BLA #3 ($z \sim 0.06805$, see Figure 3.3) could also be modeled as two separate narrower components. However, the measured BIC value is significantly lower for the one-component model, and thus, a one-component model is the preferred solution.

The BLA #6 ($z \sim 0.17576$, see Figure 3.4) could be alternatively modeled as two separate narrow components. However, similar to BLA #3, the BIC is significantly lower

[3]The BIC is also sensitive to the improvement of the fitting, and the goodness of fit will generally increase when more parameters are added to the model. In that sense, in principle, an arbitrarily high number of components could be added to fit any given BLA; thus, here we use the BIC to determine up to which point the data support a more complex model.

ID	z	b/km s^{-1}	log($N_{\rm H\,I}$ / cm^{-2})	log($N_{\rm H\,II}$ / cm^{-2})	Δlog(N$_{\rm H\,II}$/ cm^{-2})	Δlog(T/K)	Δlog $f_{\rm ion}$	Reliability
(1)	(2)	(3)	(4)	(5)	(6)	(7)	(8)	(9)
1	0.00869	35±24	12.97±0.19	18.08±0.77	18.29 - 17.65	4.9 - 4.3	5.32 - 4.68	c
2	0.01702	13±16	12.74±0.21	16.79±1.31	17.01 - 16.37	4.0 - 3.5	4.27 - 3.63	a
3	0.01982	13±18	12.67±0.24	16.70±1.56	16.92 - 16.28	4.0 - 3.5	4.25 - 3.61	c
4	0.02893	26±3	14.08±0.08	18.88±0.15	19.09 - 18.45	4.6 - 4.1	5.01 - 4.37	b
5	0.04157	28±32	12.70±0.31	17.56±1.31	17.78 - 17.14	4.7 - 4.2	5.08 - 4.44	c
6	0.04197	29±4	14.17±0.09	19.09±0.16	19.31 - 18.67	4.7 - 4.2	5.14 - 4.50	b
7	0.04246	30±4	14.33±0.13	19.27±0.21	19.48 - 18.84	4.7 - 4.2	5.15 - 4.51	b
8	0.08051	20±15	12.93±0.18	17.43±0.84	17.64 - 17.00	4.4 - 3.9	4.71 - 4.07	c
9	0.12490	25±9	16.91±2.14	21.65±2.18	21.86 - 21.22	4.6 - 4.1	4.95 - 4.31	a
10	0.12506	19±53	17.06±2.24	21.52±3.74	21.74 - 21.10	4.3 - 3.8	4.68 - 4.04	a
11	0.12529	32±29	14.79±1.30	19.80±1.64	20.02 - 19.38	4.8 - 4.3	5.23 - 4.59	a
12	0.14246	26±16	12.94±0.17	17.74±0.69	17.95 - 17.31	4.6 - 4.1	5.01 - 4.37	c
13	0.14850	27±6	13.42±0.06	18.26±0.25	18.47 - 17.83	4.6 - 4.1	5.05 - 4.41	b
14	0.17764	20±18	12.90±0.26	17.43±1.01	17.65 - 17.01	4.4 - 3.9	4.75 - 4.11	c
15	0.18494	32±22	13.00±0.19	18.04±0.77	18.25 - 17.61	4.8 - 4.3	5.25 - 4.61	c
16	0.18824	35±22	13.38±0.28	18.48±0.75	18.70 - 18.06	4.9 - 4.3	5.32 - 4.68	c
17	0.18978	36±5	14.10±0.07	19.25±0.17	19.47 - 18.83	4.9 - 4.4	5.37 - 4.73	a
18	0.19203	29±30	13.10±0.31	18.00±1.17	18.22 - 17.58	4.7 - 4.2	5.12 - 4.48	c
19	0.24255	21±7	13.27±0.08	17.83±0.36	18.05 - 17.41	4.4 - 3.9	4.78 - 4.14	b
20	0.24922	8±9	12.96±0.16	16.45±1.19	16.67 - 16.03	3.6 - 3.1	3.71 - 3.07	c
21	0.25696	28±4	13.94±0.05	18.82±0.17	19.04 - 18.40	4.7 - 4.2	5.10 - 4.46	a
22	0.25728	32±4	14.04±0.04	19.07±0.14	19.29 - 18.65	4.8 - 4.3	5.25 - 4.61	b

Table 3.2: Physical properties of the gas inferred from each one of the NLAs in our sample. Same as Table 3.1, for the NLAs ($b < 40\,{\rm km\,s^{-1}}$) detected in the QSO sightline (except for the last column, which is not included since we do not discuss NLAs case-by-case, as for BLAs).

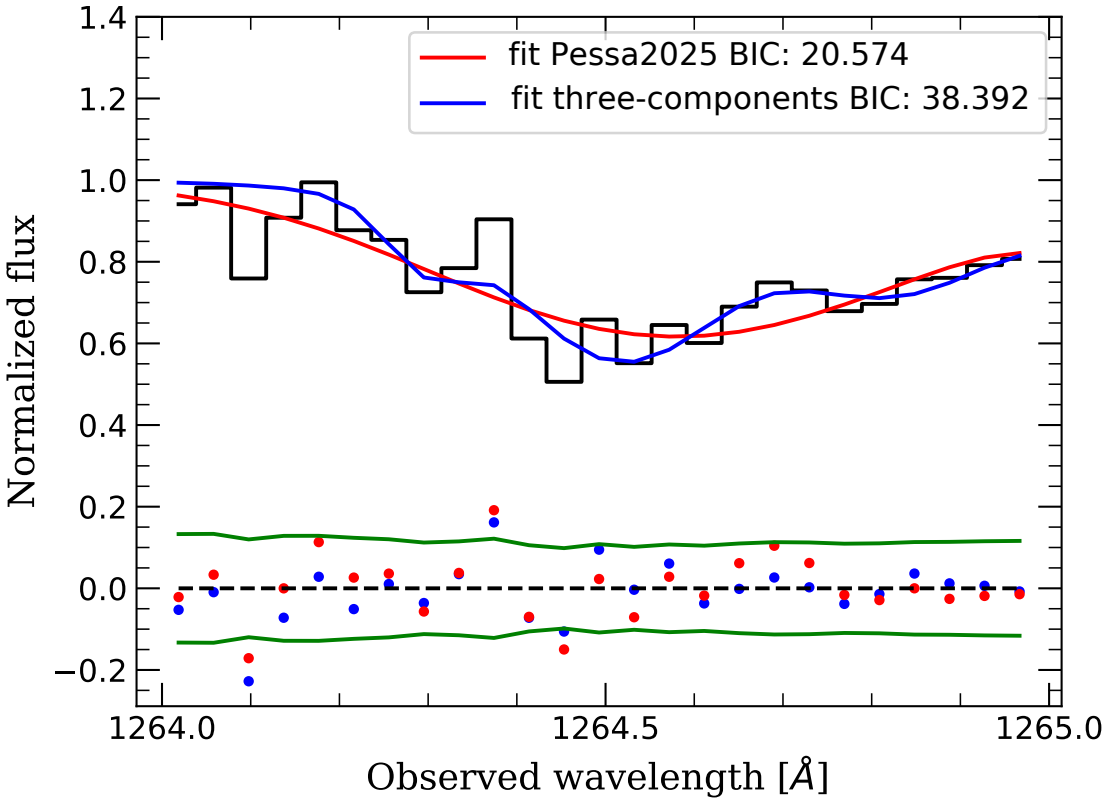

Figure 3.2: Comparison of the BIC value for a one-component fitting model (Pessa et al. 2025, in red) against a three-component fitting model (in blue) for the BLA detected at $z = 0.04021$. The red and blue dots indicate the residuals of the one-component and two-component fitting models, respectively. The green line shows the $1 - \sigma$ uncertainty of the spectrum. The fit with the lowest BIC value is considered the best fit.

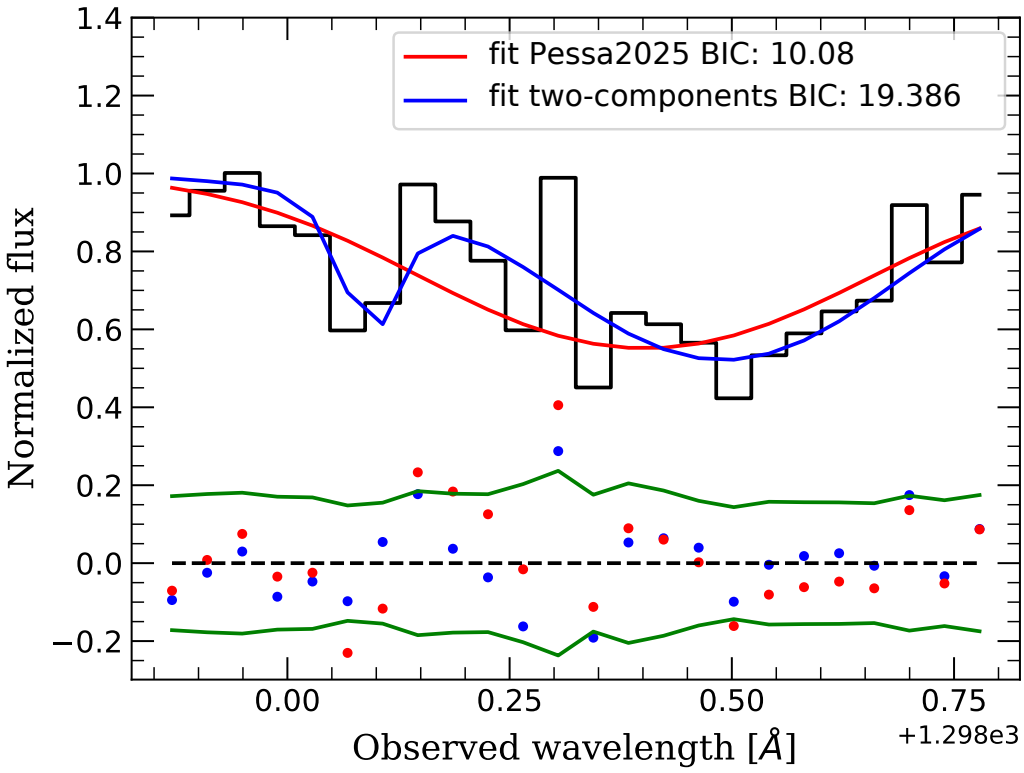

Figure 3.3: Comparison of the BIC value for a one-component fitting model (Pessa et al. 2025, in red) against a two-component fitting model (blue) for the BLA detected at $z = 0.06805$. The red and blue dots indicate the residuals of the one-component and two-component fitting models, respectively. The green line shows the $1 - \sigma$ uncertainty of the spectrum. The fit with the lowest BIC value is considered the best fit.

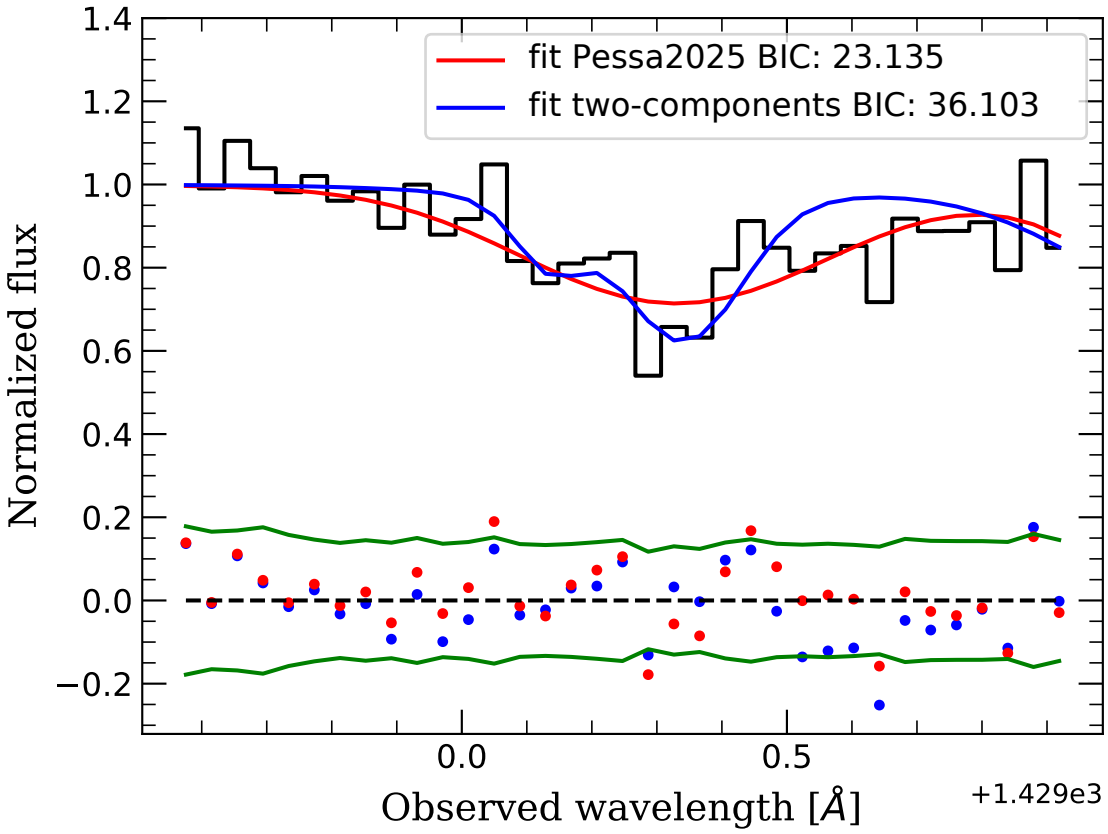

Figure 3.4: Comparison of the BIC value for a one-component fitting model (Pessa et al. 2025, in red) against a two-component fitting model (in blue) for the BLA detected at $z = 0.17576$. The red and blue dots indicate the residuals of the one-component and two-component fitting models, respectively. The green line shows the $1-\sigma$ uncertainty of the spectrum. The fit with the lowest BIC value is considered the best fit.

for the one-component fitting, and thus, we keep a one-component model as the preferred solution.

3.3 Saturated BLAs and associated metals

In this section, we present the plots of the saturated BLAs with the metals associated with their detection.

Since constraining b and N becomes degenerate for saturated lines ($N_{\rm H\,I} \gtrsim 10^{14}\,{\rm cm}^{-2}$), we present here a closer examination of our fits for the saturated BLAs in our sample (IDs 2, 10, and 13 in Fig. 3.1), as well as the fits of their associated metals and/or other H I absorption found at the same redshift, if any. Figures 3.5-3.7 show the BLAs that present saturation and their associated metals.

The BLA #2 ($z \sim 0.04866$, see Figure 3.5), shown in Fig. 3.5, exhibits Si III, Si IV

and C IV absorption at the same velocity, none of which show any sign of asymmetry, therefore we find it unlikely that this BLA is an artifact produced by the blending of narrower absorptions. Unfortunately, Lyβ is not available at this redshift, however, fitting the absorption profile with a narrower Doppler parameter (1-σ lower than best-fitting value) produces a qualitatively worse fit that does not reproduce the spectral profile of the BLA. Thus, we conclude that the identification of this absorption as BLA is not a result of an unconstrained Doppler parameter.

The BLA #10 ($z \sim 0.18787$, see Figure 3.6) is shown in Fig. 3.6. This H I absorption feature presents an asymmetry that we model with an additional narrower component. Lyβ and Lyγ coverage are available at this redshift, and the spectra show consistency with absorption (although the latter is extremely shallow), further constraining the Doppler parameter and column density of the BLA. The detection of a O VI absorption is also consistent with the presence of warm-hot gas at this redshift. Overall, we believe that although there is a blend, the detection of this BLA is robust, and the parameters of the Voigt profile are well-constrained. Indeed, we find that fitting the BLA with a 1-σ narrower b produces a model that is not consistent with the observed absorption profile.

The BLA #13 ($z \sim 0.25294$, see Figure 3.7) is shown in Fig. 3.7. This BLA does not present any sign of asymmetry in its spectral profile. Lyβ and Lyγ are also available at this redshift, although similar to the BLA #10, the latter is very shallow (Lyβ, on the other hand, represents a more clear detection). We also find that fitting the BLA with a 1-σ narrower b produces a model that is not consistent with the data. Altogether, we find that this BLA is a robust identification and that the parameters of the Voigt profile are well-constrained.

3.4 Summary and Conclusions

This chapter focuses on the methodology used to identify absorption components along the spectra of a QSO sightline acquired in the FUV range in the HST/COS for QSO SDSSJ161940.56+254323.0. We focus our analysis on H I detections characterized by the Doppler parameter, column density, equivalent width, and redshift. Since the interest of the work is to probe WHIM, we focus on BLA features and further analyze metal absorptions in the QSO spectra at the same redshift, providing further evidence of the galactic origin of these features. Additionally, we present statistical validation of the detection method, evaluating different fitting approaches using the BIC to determine whether single- or multiple-component models are better suited to the observed spectra.

In this work, a sample of 13 BLAs identified on the HST/COS FUV spectra of the QSO SDSSJ161940.56+254323.0 was used to infer the physical properties of the WHIM. We have also further identified 12 NLAs that we include in our analyses for comparison

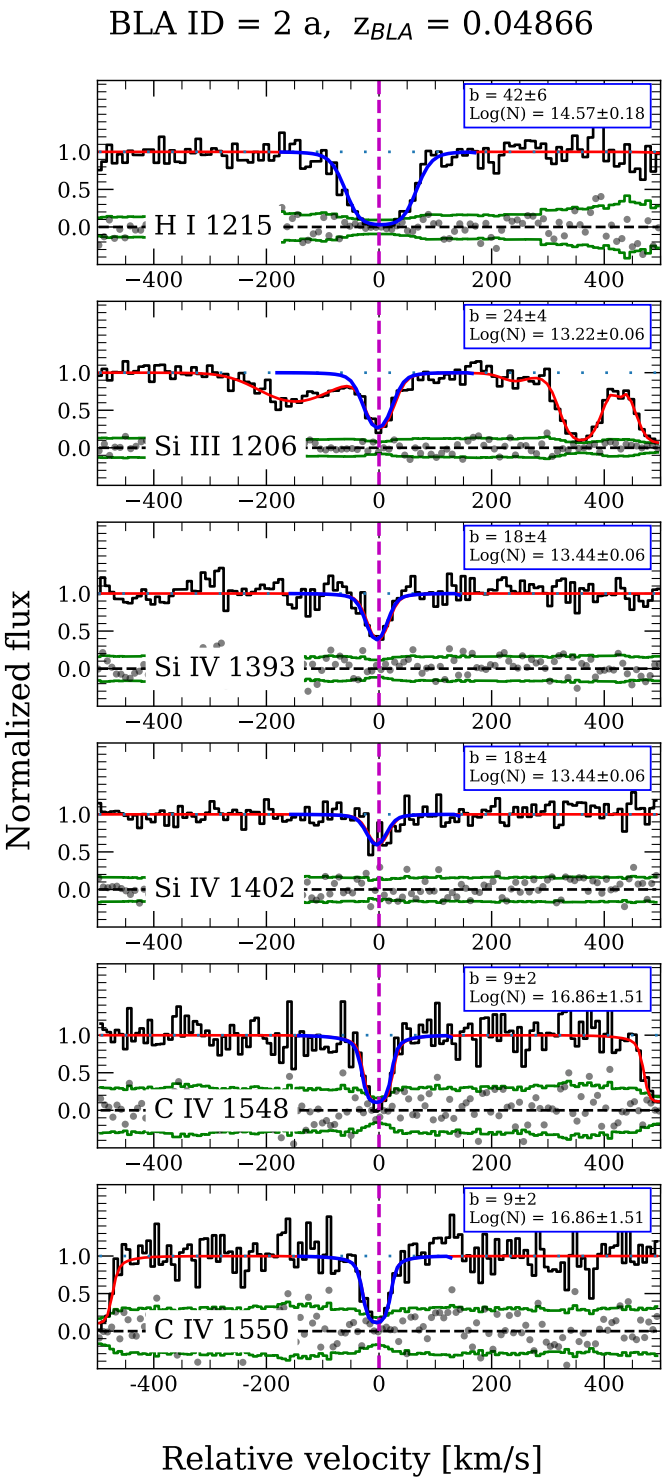

Figure 3.5: H I absorption feature for ID 2 with $z = 0.0486$. The metals detected in this H I absorption associated kinematically aligned are shown under the BLA (only transitions with reliability 'a' and 'b' are shown, see Sec. 3.2 for details of the reliability categories). The spectrum is shown in black, and the continuum is shown in blue dots. The best Voigt profile fit is shown in blue. The observational parameters of the Doppler parameter in km s^{-1} and column density log(N/cm^{-2}) are shown in the upper right part of the panels.

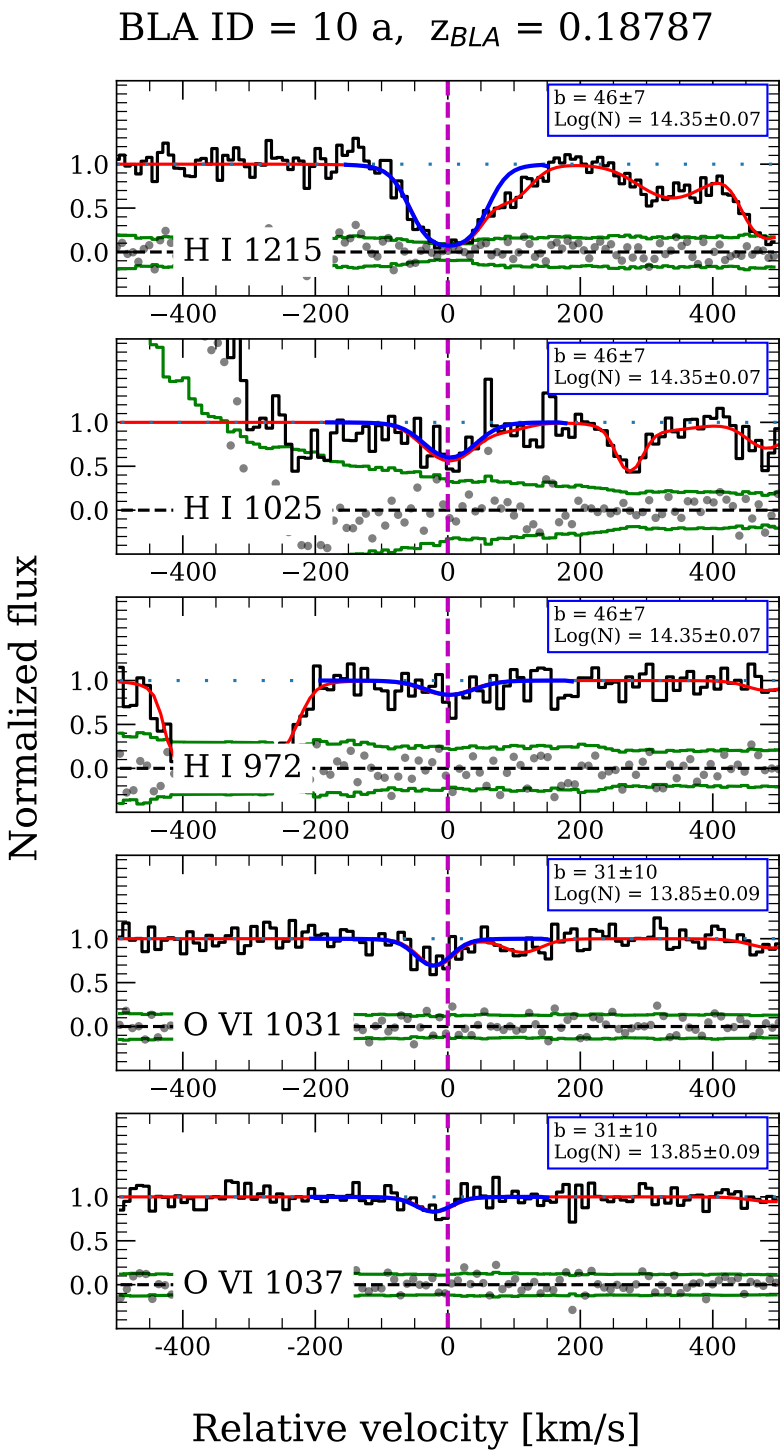

Figure 3.6: H I absorption feature for ID 10 with $z = 0.18787$. The metals detected in this H I absorption associated kinematically aligned are shown under the BLA (only transitions with reliability 'a' and 'b' are shown, see Sec. 3.2 for details of the reliability categories). The spectrum is shown in black, and the continuum is shown in blue dots. The best Voigt profile fit is shown in blue. The observational parameters of the Doppler parameter in km s^{-1} and column density log(N/cm^{-2}) are shown in the upper right part of the panels.

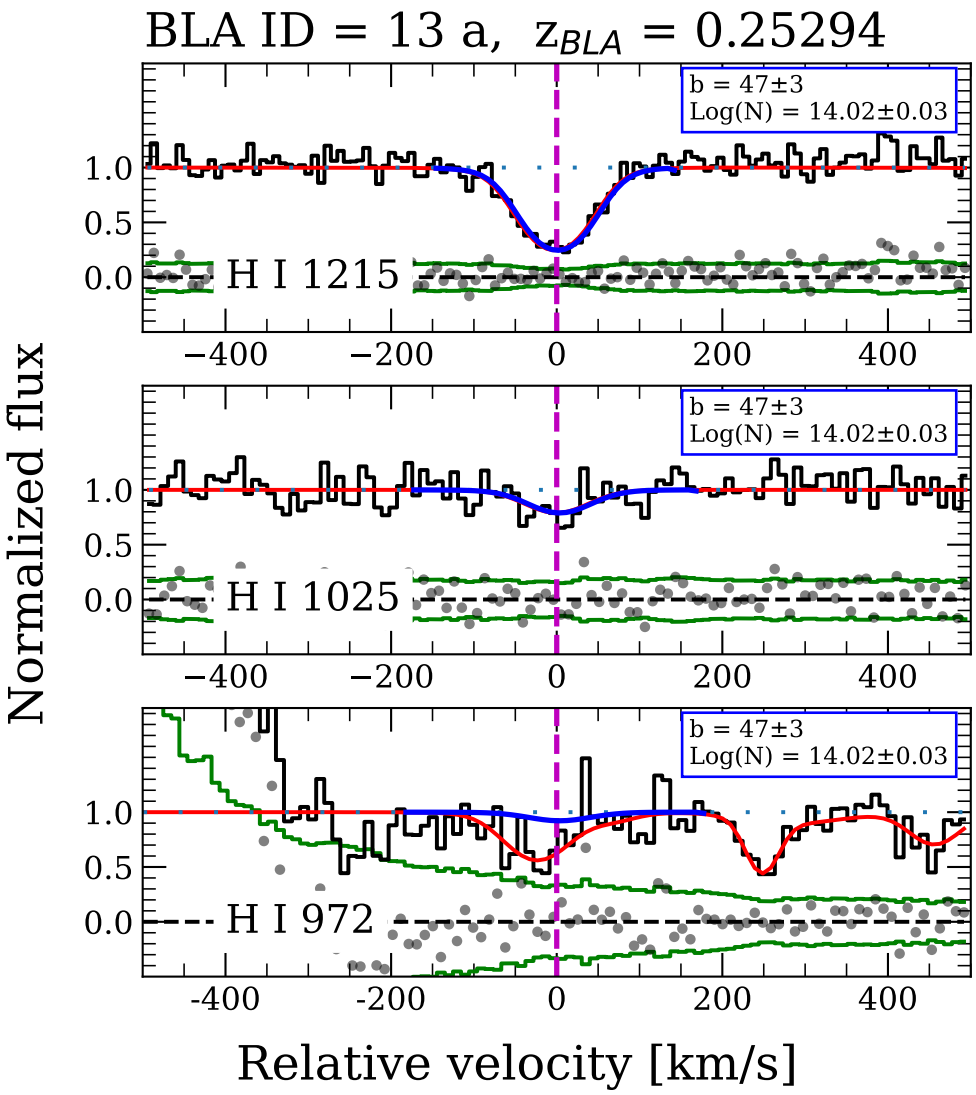

Figure 3.7: H I absorption feature for ID 13 with $z = 0.25294$. The metals detected in this H I absorption associated kinematically aligned are shown under the BLA (only transitions with reliability 'a' and 'b' are shown, see Sec. 3.2 for details of the reliability categories). The spectrum is shown in black, and the continuum is shown in blue dots. The best Voigt profile fit is shown in blue. The observational parameters of the Doppler parameter in km s^{-1} and column density log(N/cm^{-2}) are shown in the upper right part of the panels.

purposes. This QSO is targeted because its sightline maximizes the number of inter-cluster filaments intersected. In this work, the presence of galaxies was studied (using VLT/MUSE and VLT/VIMOS data, see Pessa et al. 2025 for further details) at the redshift of the BLAs to infer if the BLAs could potentially be produced by gas gravitationally bound to a galaxy, or, alternatively, if both, BLAs and galaxies are tracing the same large-scale filament of galaxies but are otherwise not directly associated.

Altogether, this work shows that most of the BLAs identified in the FUV spectra of QSO SDSSJ161940.56+254323.0 are really tracing WHIM, and that WHIM properties correlate with the distribution of galaxies within its local volume, where denser intergalactic gas correlates with a stronger local excess of galaxies, relative to the cosmic expectancy (see Figure 14 from Pessa et al. 2025). This provides an alternative observational perspective to similar correlations reported in the literature, derived using cosmological simulations, between properties of cosmic filaments and properties of the intergalactic gas residing in them.

Chapter 4

Pinpointing the cosmic web between massive galaxy clusters I: The incidence of H I and O VI

Chapter based on the article ***Karen Martínez-Acosta****, et al. in prep. Tentative title: "Pinpointing the cosmic web between massive galaxy clusters I: Incidence of H I and O VI as tracers of the WHIM".*

4.1 Estimation of Incidences

We search for intervening absorption lines in each QSO spectrum and characterize their observational parameters. We focus our analysis on total H I, narrow Lyα absorbers ($b < 40$ km s^{-1}) known as NLAs, broad Lyα absorbers ($b \geq 40$ km s^{-1}) known as BLAs, and O VI absorption lines which characterize the IGM towards the line of sight of QSOs.

Following the analysis described in Section 2.4 for our survey of ten QSO sightlines, we detected 99, 83 and 141 NLAs with reliabilities 'a', 'b' and 'c', respectively; 11, 76 and 66 BLAs with reliabilities 'a', 'b' and 'c', respectively; and 34, 6 and 4 O VI with reliabilities 'a', 'b' and 'c', respectively. However, in this work, we restrict our analysis only to absorption features with reliabilities 'a' and 'b'.

The observational parameters, derived from the absorption lines detected and fitted in all QSO sightlines of our survey, will be available in an online repository after publication of the article. Here we show, as an example, the table of observational parameters for a subset of the absorption components in Table 4.1.

In Figures 4.1-4.4, we show the NLAs (in blue), BLAs (in red), and O VI (in green) absorptions that we found at a velocity window of $\Delta v = \pm 1000$km s^{-1} and at impact parameters $\Delta d \leq 3$ Mpc from the cluster-pairs axes. These are the fiducial values under consideration in this study, which are identical to those used in Tejos et al. 2016 and are

ID	ion	wavelength$_{obs}$/Å	z	log(N/cm^{-2})	b/km s^{-1}	EW	SNR	reliability
(1)	(2)	(3)	(4)	(5)	(6)	(7)	(8)	(9)
1	N I	1199.5	−0.00006 ± 0.00001	16.46 ± 1.03	7 ± 1	0.155 ± 0.051	12 ± 1	a
2	C II*	1335.6	−0.00006 ± 0.00001	13.99 ± 0.08	24 ± 7	0.133 ± 0.027	9 ± 1	b
3	Fe II	1608.4	−0.00005 ± 0.00001	14.56 ± 0.06	27 ± 5	0.292 ± 0.044	5 ± 1	a
4	S II	1259.5	−0.00005 ± 0.00001	15.03 ± 0.03	16 ± 2	0.139 ± 0.014	20 ± 1	a
5	Al II	1670.7	−0.00004 ± 0.00001	13.49 ± 0.10	44 ± 7	0.598 ± 0.108	6 ± 1	b
6	Si IV	1393.7	−0.00003 ± 0.00001	13.67 ± 0.04	59 ± 6	0.315 ± 0.030	13 ± 1	a
7	Si III	1206.5	−0.00003 ± 0.00008	13.94 ± 0.72	51 ± 21	0.574 ± 0.570	11 ± 2	a
8	C IV	1548.2	−0.00003 ± 0.00004	13.96 ± 0.13	45 ± 15	0.278 ± 0.086	8 ± 1	a
9	C II	1334.5	−0.00002 ± 0.00001	15.23 ± 0.24	43 ± 8	0.630 ± 0.165	9 ± 1	b
10	Si II	1260.4	−0.00000 ± 0.00001	14.53 ± 0.03	37 ± 1	0.574 ± 0.016	20 ± 1	a
11	N I	1199.6	0.00006 ± 0.00001	13.70 ± 0.18	22 ± 15	0.070 ± 0.033	12 ± 1	a
12	Si III	1206.7	0.00016 ± 0.00062	13.54 ± 1.74	72 ± 83	0.491 ± 0.780	11 ± 1	c
13	Fe II	1608.8	0.00021 ± 0.00001	13.56 ± 0.23	10 ± 18	0.041 ± 0.043	5 ± 1	a
14	C IV	1548.6	0.00028 ± 0.00005	13.81 ± 0.18	43 ± 19	0.210 ± 0.088	8 ± 1	a
15	C II	1335.0	0.00032 ± 0.00002	14.12 ± 0.12	25 ± 9	0.182 ± 0.055	9 ± 1	b
16	H I	1221.0	0.00440 ± 0.00002	13.95 ± 0.05	43 ± 7	0.316 ± 0.042	10 ± 2	b
17	H I	1221.7	0.00493 ± 0.00005	13.17 ± 0.17	43 ± 25	0.074 ± 0.031	11 ± 1	c
18	H I	1224.5	0.00724 ± 0.00006	13.21 ± 0.13	68 ± 28	0.083 ± 0.026	12 ± 1	b
19	H I	1229.1	0.01104 ± 0.00001	13.57 ± 0.05	28 ± 5	0.149 ± 0.020	12 ± 1	b
20	H I	1239.1	0.01925 ± 0.00005	13.34 ± 0.09	82 ± 21	0.112 ± 0.023	14 ± 1	b
21	H I	1241.3	0.02106 ± 0.00002	13.31 ± 0.07	44 ± 10	0.099 ± 0.016	15 ± 1	b
22	H I	1250.5	0.02868 ± 0.00009	13.31 ± 0.30	69 ± 17	0.104 ± 0.068	20 ± 1	c
23	H I	1251.5	0.02949 ± 0.00002	13.19 ± 0.06	32 ± 8	0.075 ± 0.012	20 ± 1	b
24	H I	1251.9	0.02981 ± 0.00002	13.06 ± 0.08	24 ± 8	0.056 ± 0.011	20 ± 1	b
25	H I	1256.2	0.03336 ± 0.00008	13.05 ± 0.12	98 ± 35	0.060 ± 0.017	20 ± 1	b
26	H I	1257.5	0.03438 ± 0.00006	12.84 ± 0.15	51 ± 25	0.037 ± 0.013	20 ± 1	c
27	H I	1260.9	0.03719 ± 0.00003	12.66 ± 0.20	10 ± 17	0.022 ± 0.018	20 ± 1	c
28	H I	1264.6	0.04024 ± 0.00002	13.23 ± 0.07	31 ± 8	0.080 ± 0.013	17 ± 1	b
29	H I	1271.5	0.04593 ± 0.00009	13.23 ± 0.18	67 ± 36	0.087 ± 0.037	10 ± 2	c
30	H I	1291.8	0.06260 ± 0.00004	13.03 ± 0.16	26 ± 17	0.053 ± 0.021	10 ± 1	c
31	H I	1292.5	0.06317 ± 0.00002	13.50 ± 0.07	43 ± 10	0.144 ± 0.026	10 ± 1	b
32	H I	1292.9	0.06353 ± 0.00004	12.73 ± 0.32	6 ± 17	0.024 ± 0.029	10 ± 1	c
33	H I	1307.7	0.07568 ± 0.00006	12.86 ± 0.24	28 ± 26	0.037 ± 0.023	10 ± 1	c
34	H I	1309.4	0.07706 ± 0.00001	13.86 ± 0.06	26 ± 5	0.223 ± 0.038	10 ± 1	b
35	H I	1309.7	0.07736 ± 0.00004	13.29 ± 0.14	36 ± 18	0.093 ± 0.033	10 ± 1	c
36	H I	1324.5	0.08955 ± 0.00003	13.36 ± 0.12	38 ± 14	0.107 ± 0.031	9 ± 1	b
37	H I	1341.8	0.10375 ± 0.00005	12.93 ± 0.21	26 ± 22	0.042 ± 0.023	9 ± 1	c
38	H I	1347.6	0.10850 ± 0.00011	13.26 ± 0.16	92 ± 43	0.095 ± 0.036	9 ± 1	c
39	H I	1366.7	0.12427 ± 0.00008	13.11 ± 0.18	57 ± 32	0.066 ± 0.027	10 ± 1	c
40	H I	1373.3	0.12968 ± 0.00007	13.12 ± 0.18	49 ± 28	0.068 ± 0.029	9 ± 1	c
41	H I	1375.9	0.13178 ± 0.00001	13.15 ± 0.14	18 ± 11	0.063 ± 0.025	9 ± 1	c
42	H I	1376.4	0.13225 ± 0.00001	13.94 ± 0.04	65 ± 8	0.347 ± 0.036	9 ± 1	b
43	H I	1393.1	0.14595 ± 0.00001	13.26 ± 0.21	210 ± 1	0.096 ± 0.046	13 ± 1	c
44	H I	1405.5	0.15617 ± 0.00001	13.62 ± 0.04	60 ± 7	0.193 ± 0.019	14 ± 1	b
45	N III	1150.2	0.16203 ± 0.00009	13.74 ± 0.21	49 ± 34	0.054 ± 0.027	8 ± 1	c
46	H I	1412.7	0.16204 ± 0.00002	13.00 ± 0.11	23 ± 10	0.049 ± 0.013	13 ± 1	a
47	O VI	1203.4	0.16613 ± 0.00004	13.88 ± 0.08	58 ± 15	0.087 ± 0.017	12 ± 1	a
48	Si III	1407.0	0.16617 ± 0.00004	12.04 ± 0.23	16 ± 19	0.021 ± 0.040	14 ± 1	c
49	H I	1417.8	0.16624 ± 0.00001	14.54 ± 0.04	39 ± 2	0.473 ± 0.033	15 ± 1	a
50	H I	1418.1	0.16654 ± 0.00004	13.10 ± 0.27	21 ± 13	0.059 ± 0.037	15 ± 1	c
51	H I	1418.7	0.16703 ± 0.00004	12.94 ± 0.14	36 ± 17	0.044 ± 0.014	15 ± 1	a
52	H I	1448.7	0.19172 ± 0.00007	13.34 ± 0.08	106 ± 26	0.112 ± 0.022	16 ± 1	b
53	H I	1472.6	0.21131 ± 0.00001	13.01 ± 0.04	16 ± 4	0.047 ± 0.006	30 ± 1	b
54	C III	1184.6	0.21246 ± 0.00007	13.15 ± 0.11	79 ± 27	0.084 ± 0.022	11 ± 1	b
55	H I	1474.0	0.21254 ± 0.00001	14.69 ± 0.05	17 ± 1	0.253 ± 0.010	33 ± 3	a
56	H I	1474.8	0.21318 ± 0.00004	12.39 ± 0.17	24 ± 17	0.013 ± 0.005	34 ± 2	c
57	H I	1656.2	0.36241 ± 0.00003	13.24 ± 0.18	15 ± 13	0.072 ± 0.043	5 ± 1	c
58	H I	1688.4	0.38882 ± 0.00006	13.04 ± 0.22	27 ± 22	0.054 ± 0.030	6 ± 1	c

continue online...

Table 4.1: Table of the observational parameters of the absorption features detected in our survey. For each identification, we report the (1) ID, (2) name of the ion, (3) wavelength of observation, (4) redshift, (5) column density, (6) Doppler parameter, (7) equivalent width, (8) signal-to-noise ratio, and (9) reliability. We show only the first few rows, corresponding to absorption features on the QSO J1210+0154 sightline; the complete table will be available in a digital repository after publication of the article.

retained for comparison. The fiducial value for Δv is in agreement with the third constraint from Section 2.2.1 to account for the typical velocity dispersion of galaxy clusters and a contribution from a cosmological redshift difference (Tejos et al. 2016). And the selection of the fiducial value for Δd is directly motivated by observational results (see Section 4.1.1).

Additionally, in Figure 4.5 we show transitions O VI 1031 Å and O VI 1037 Å for each O VI absorption line detected in our survey with reliability 'a' or 'b'. We have included only absorption lines detected within a rest-frame velocity window of $\Delta v = \pm$ 1000 km s^{-1} and at impact parameter $\Delta d \leq 3$ Mpc from the cluster-pairs. The spectrum is shown in black, the continuum in blue dots, and the Voigt profile fit in green. The observational parameters, Doppler parameter in km s^{-1}, column density log(N/cm^{-2}), and rest-frame equivalent width W_r in Å, are shown in the upper right part of the first panel. The detection ID, reliability, and redshift are shown in the upper-left corner of the first panel. Notice that for QSO J1456+2750, a gap in the spectrum is identified at the wavelength corresponding to the O VI 1037 Å transition.

After conducting our analysis, we utilized the derived Doppler parameters, column density, and equivalent width to identify correlations between the observational parameters, considering the samples of interest: total H I, BLAs, NLAs, and O VI.

We show the Doppler parameter distribution b as a function of the column densities N, for our sample of H I (black circles) in Figure 4.6 and O VI (green circles) in Figure 4.7, between $0.1 \leq z \leq 0.5$. The uncertainties are shown in the background, and the gray dashed horizontal line represents our limit in the Doppler parameter of 40 km s^{-1}, which we use to split BLA in the upper part of the H I plot and NLA samples in the bottom part.

4.1.1 Redshift path sensitivity function

Given that our survey compiles the absorber path lengths of several quasar sightlines, we needed to estimate the redshift path sensitivity function $g(z)$. This function quantifies the effective redshift path over which a survey is sensitive to detect a given absorption line. For an ideal spectrum, the function $g(z)$ is defined according to equation (4.1):

$$g(z) = \sum_{k=1}^{M} H(z - z_k^{min}) H(z_k^{max} - z), \tag{4.1}$$

here, the sum is over all QSO sightlines, M is number of quasars in the survey, the kth quasar has a redshift path ranging from z_k^{min} to z_k^{max}, and $H(t)$ is the Heaviside step function defined by the equation:

$$H(t) = \begin{cases} 0 & : \quad t < 0 \\ 1 & : \quad t \geq 0 \end{cases} \tag{4.2}$$

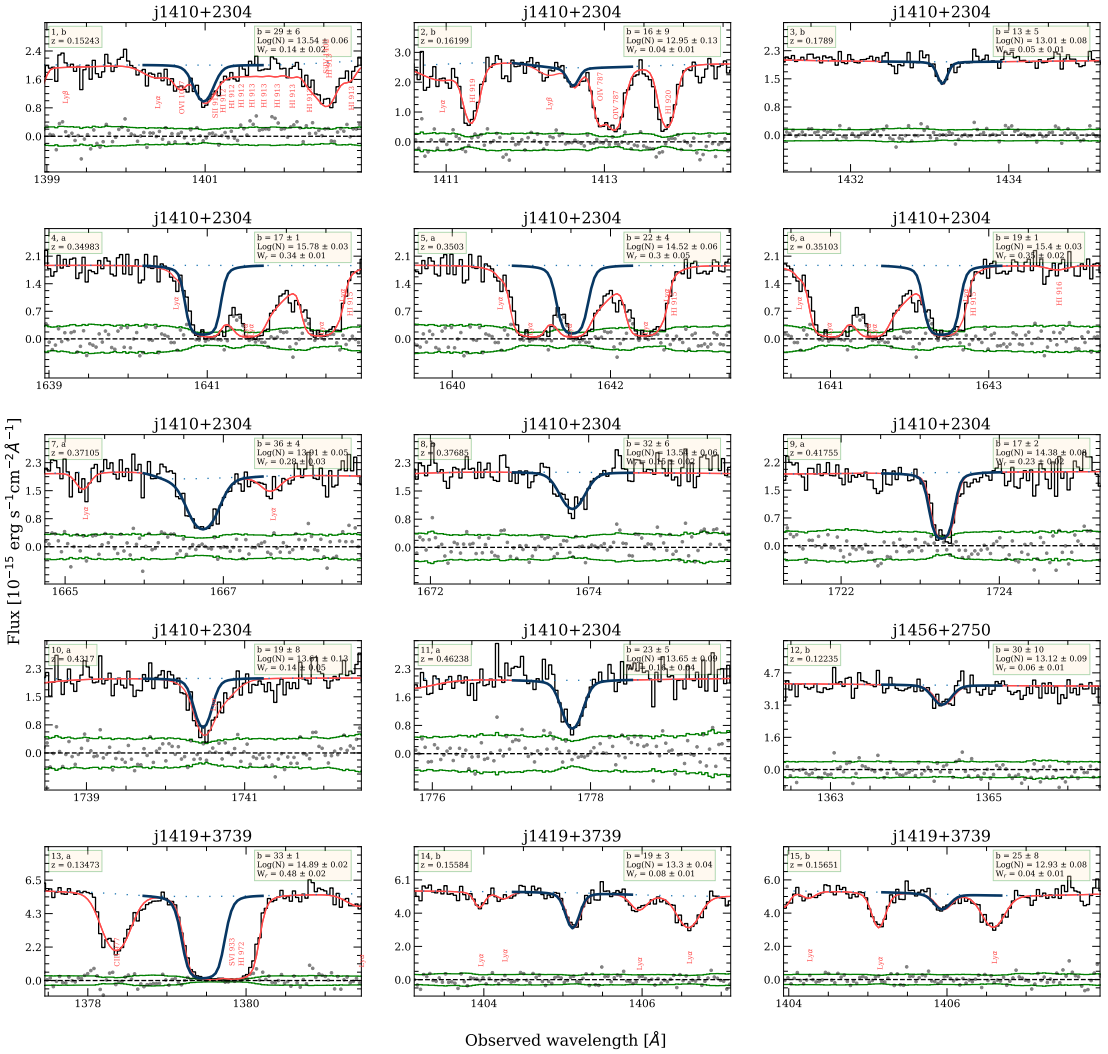

Figure 4.1: Identified NLAs in a velocity window of $\Delta v = \pm$ 1000km s^{-1} and at impact parameter $\Delta d \leq 3$ Mpc from the cluster-pairs. The panels show the best-fitting Voigt profile for each NLA (thick blue line) and the full QSO spectrum model (thin red line). The dotted blue line shows the continuum level. The additional transitions identified in the same wavelength range are labeled in red. At the top-right corner of each panel, we show the derived observational parameters: column density $\log(N/cm^{-2})$, Doppler parameter in km s^{-1}, and equivalent width in Å. In the top-left corner of each panel, we show the ID, reliability, and redshift of each identified absorption. Each plot title specifies the QSO to which the absorption feature corresponds. The last two panels show the spectra of QSO J1410+0910 at the redshift of the cluster-pairs, where no transitions are detected. These panels continue on Figure 4.2.

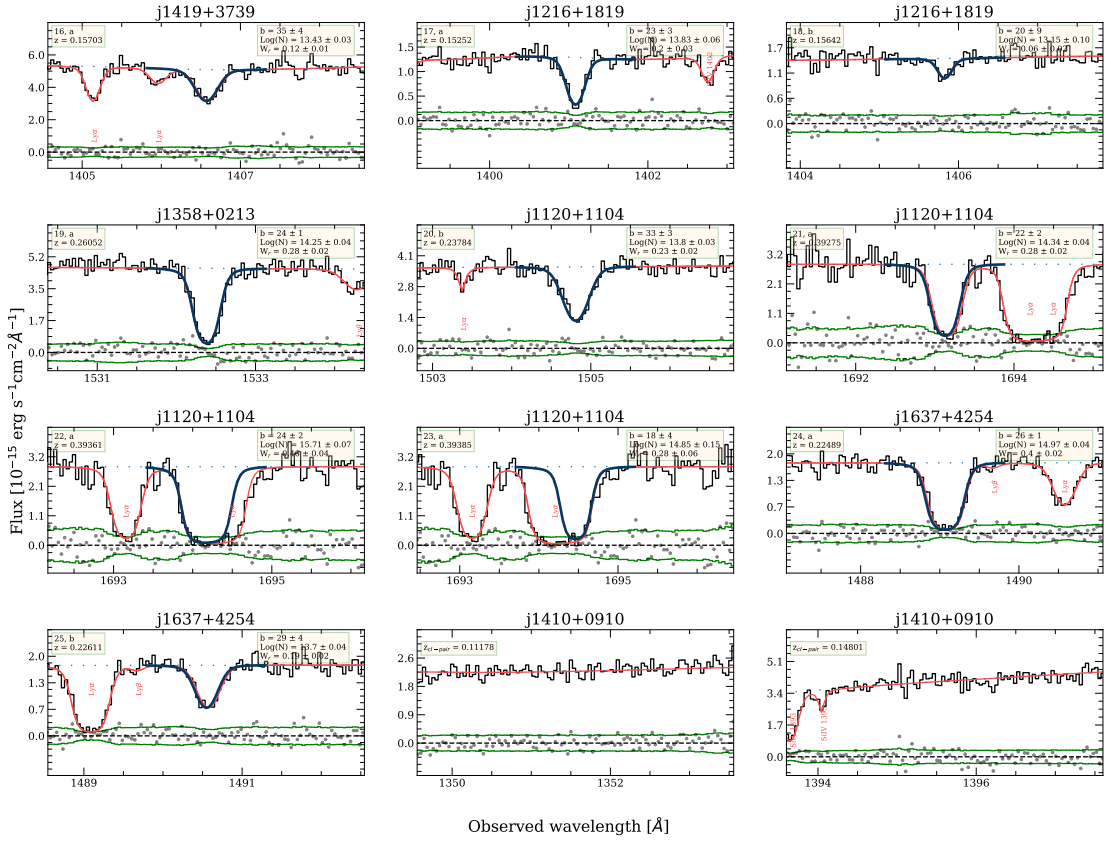

Figure 4.2: Continuation of Figure 4.1

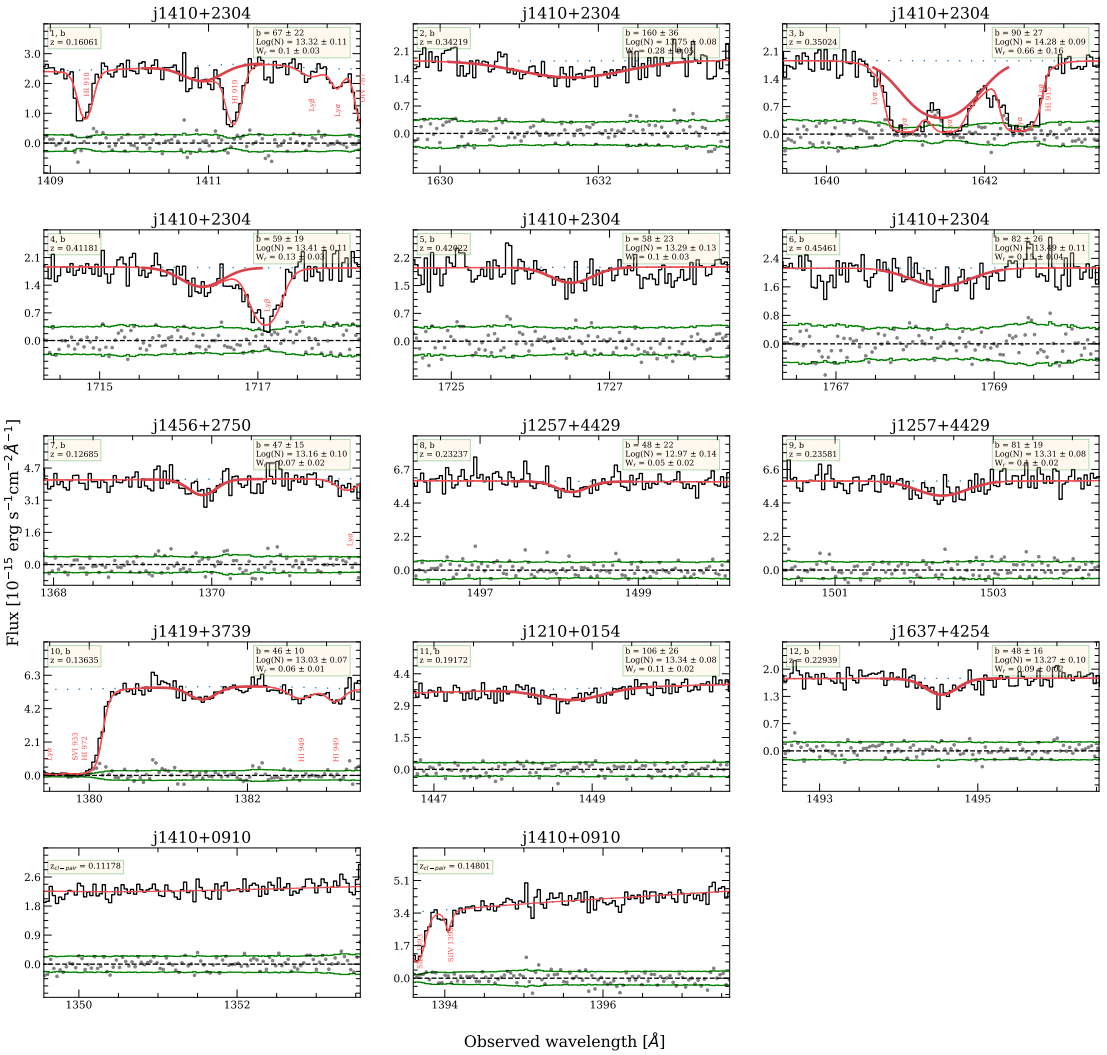

Figure 4.3: Identified BLAs in a velocity window of $\Delta v = \pm$ 1000km s^{-1} and at impact parameter $\Delta d \leq 3$ Mpc from the cluster-pairs. The panels show the best-fitting Voigt profile for each BLA (thick red line) and the full QSO spectrum model (thin red line). The dotted blue line shows the continuum level. The additional transitions identified in the same wavelength range are labeled in red. At the top-right corner of each panel, we show the derived observational parameters: column density $\log(N/cm^{-2})$, Doppler parameter in km s^{-1}, and equivalent width in Å. In the top-left corner of each panel, we show the ID, reliability, and redshift of each identified absorption. Each plot title specifies the QSO to which the absorption feature corresponds. The last two panels show the spectra of QSO J1410+0910 at the redshift of the cluster-pairs, where no transitions are detected.

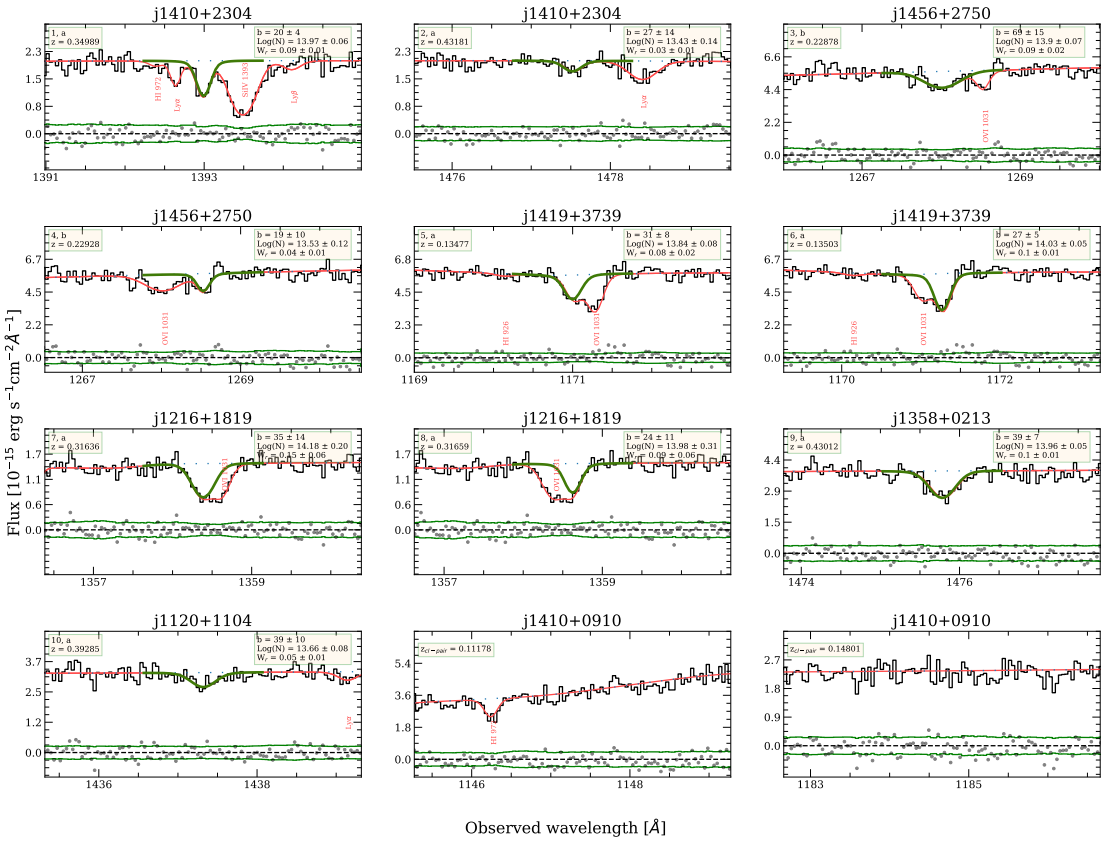

Figure 4.4: Identified O VI in a velocity window of $\Delta v = \pm$ 1000 km s^{-1} and at impact parameter $\Delta d \leq 3$ Mpc from the cluster-pairs. The panels show the best-fitting Voigt profile for each O VI (thick green line) and the full QSO spectrum model (thin red line). The dotted blue line shows the continuum level. The additional transitions identified in the same wavelength range are labeled in red. At the top-right corner of each panel, we show the derived observational parameters: column density $\log(N/cm^{-2})$, Doppler parameter in km s^{-1}, and equivalent width in Å. In the top-left corner of each panel, we show the ID, reliability, and redshift of each identified absorption. Each plot title specifies the QSO to which the absorption feature corresponds. The last two panels show the spectra of QSO J1410+0910 at the redshift of the cluster-pairs, where no transitions are detected.

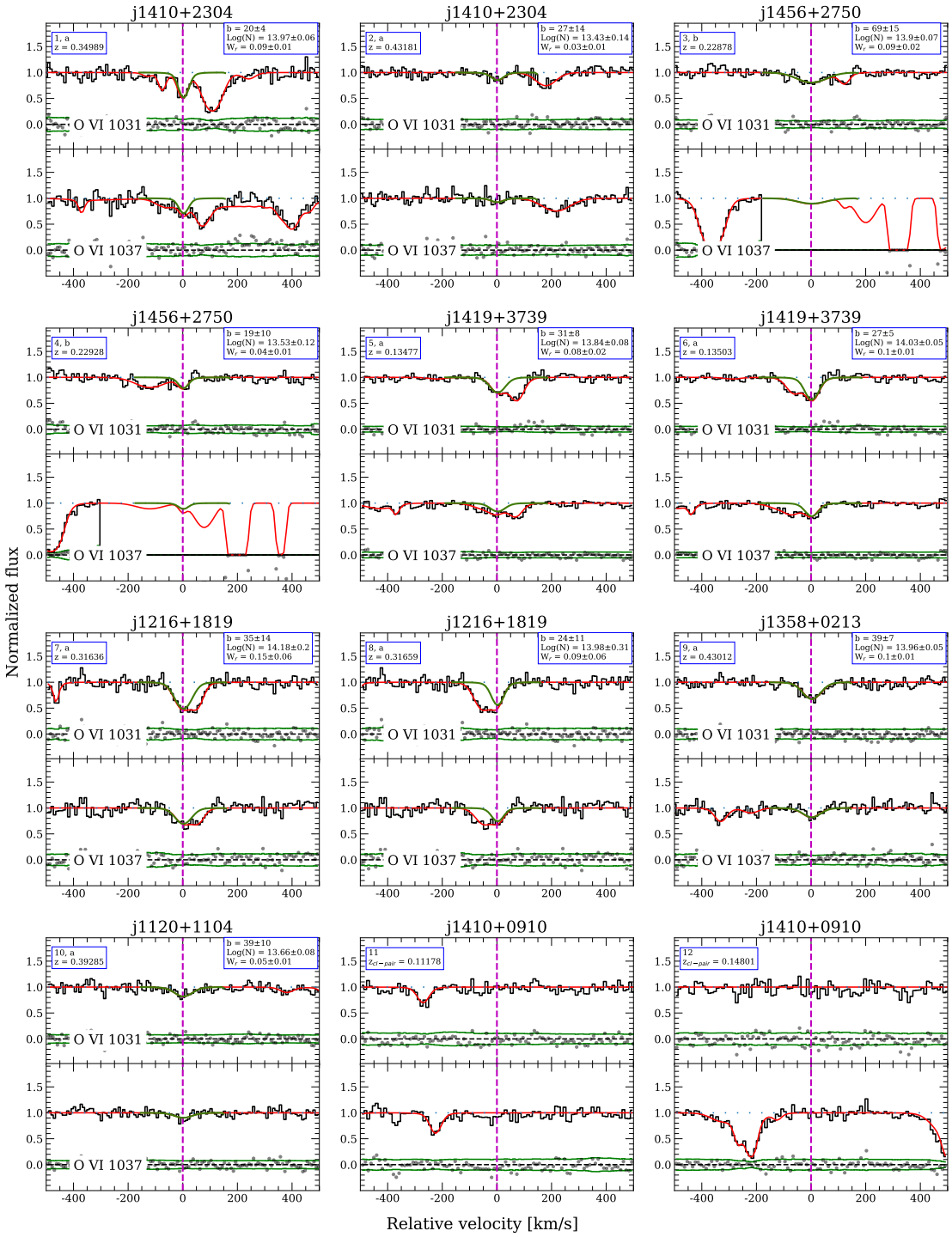

Figure 4.5: Transitions O VI 1031 Å and O VI 1037 Å are shown in relative velocity for each O VI absorption line detected in our survey with reliability 'a' or 'b'. We have included only absorption lines detected within a rest-frame velocity window of $\Delta v = \pm 1000$ km s^{-1} and at impact parameter $\Delta d \leq 3$ Mpc from the cluster-pairs. The spectrum is shown in black, the continuum in blue dots, and the Voigt profile fit in green. The observational parameters, Doppler parameter in km s^{-1}, column density log(N/cm^{-2}), and rest-frame equivalent width W_r in Å, are shown in the upper right part of the first plot in each panel. The id of the detection, reliability, and redshift are shown in the upper left part of the first plot in each panel.

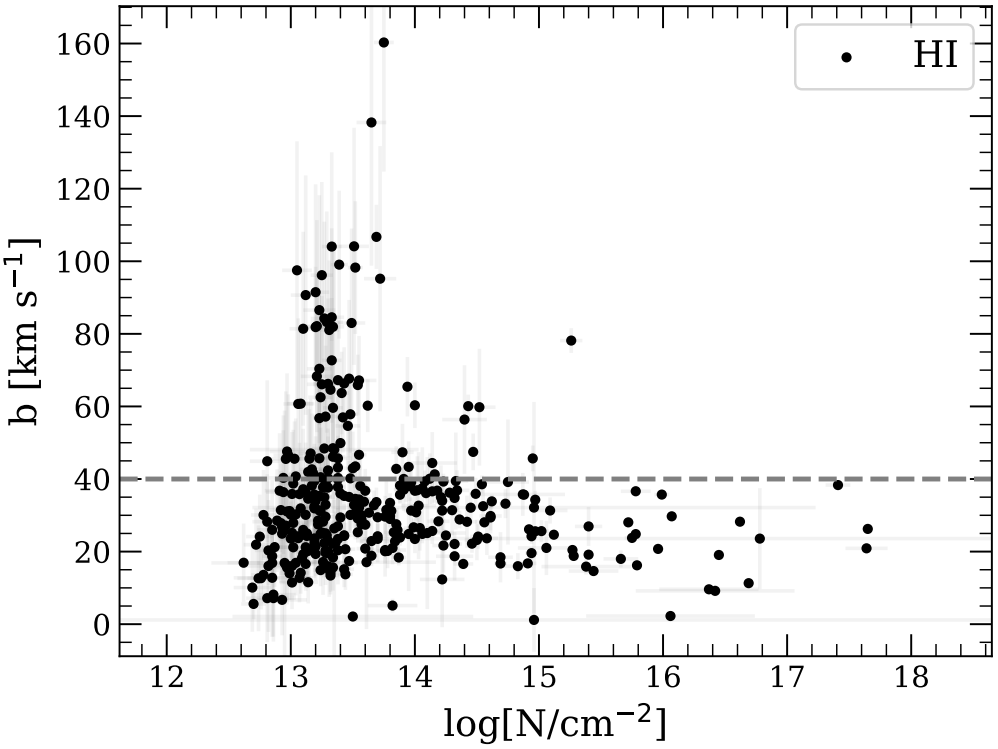

Figure 4.6: Doppler parameter distribution as a function of the column densities for our sample of H I. The uncertainties are shown in the background, and the gray dashed horizontal line represents our limit on the Doppler parameter of 40 km s^{-1}.

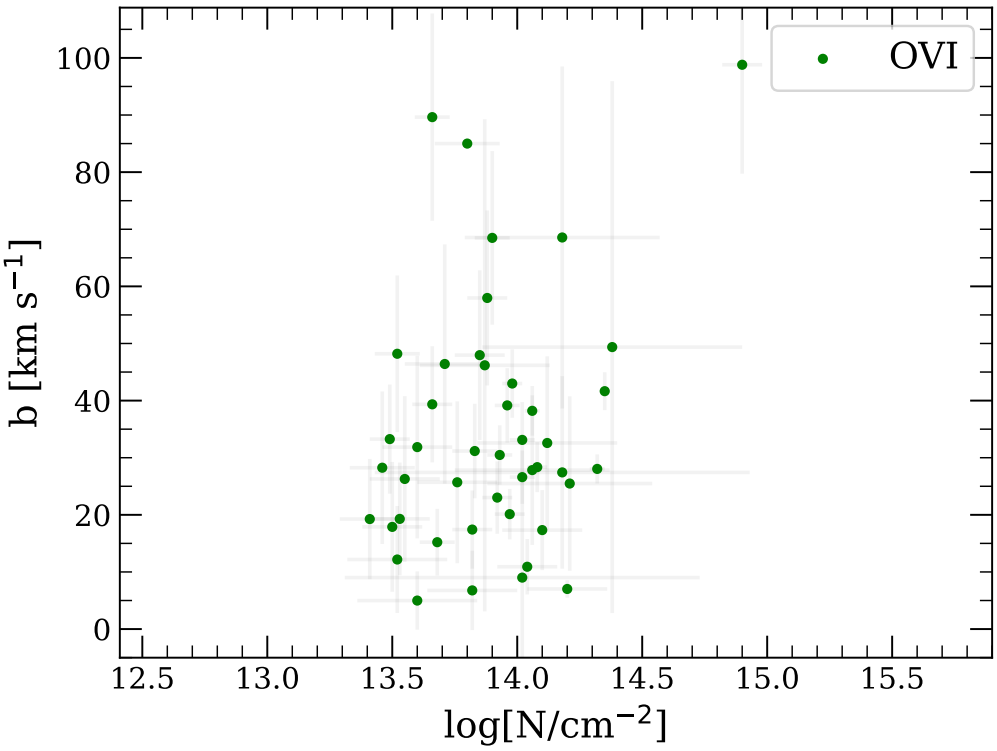

Figure 4.7: Doppler parameter distribution as a function of the column densities for our sample of O VI. The uncertainties are shown in the back.

Considering an ideal spectrum, the redshift path for each sightline, according to equation (4.1) is $\Delta z = z_{max} - z_{min}$. However, for a real observed spectrum, several factors must be accounted for when calculating the redshift path to exclude regions of the spectrum where absorptions cannot be detected. In particular, we followed the constraints reported in Appendix C of Tejos et al. 2016. In summary, we considered only regions where the QSO spectrum covers the redshift range of $0.1 \leq z \leq 0.5$ for the absorption of interest (H I and O VI). We mask out regions with fluxes below 50% of the value of the continuum fit; this is because of biases against detecting absorption systems on top of strong absorption lines. We also masked out regions within ± 200 km s^{-1} from expected strong Galactic absorption. After that, we estimated the minimum rest-frame equivalent width to observe a transition at rest-frame wavelength, λ_0, along the spectrum by the relation of equation (4.3).

$$W_{r,\lambda_0}^{min} = 3\frac{\lambda_0 R}{\langle S/R \rangle}, \tag{4.3}$$

with R the resolution of the COS spectrograph (taken to be $R = 20000$), and $\langle S/R \rangle$ is the signal-to-noise ratio per resolution element of the spectrum. Then we identified portions of the spectrum satisfying the criteria given in equation 4.4.

$$W_{r,\lambda_0}^{min} \geq W_r^{min}. \tag{4.4}$$

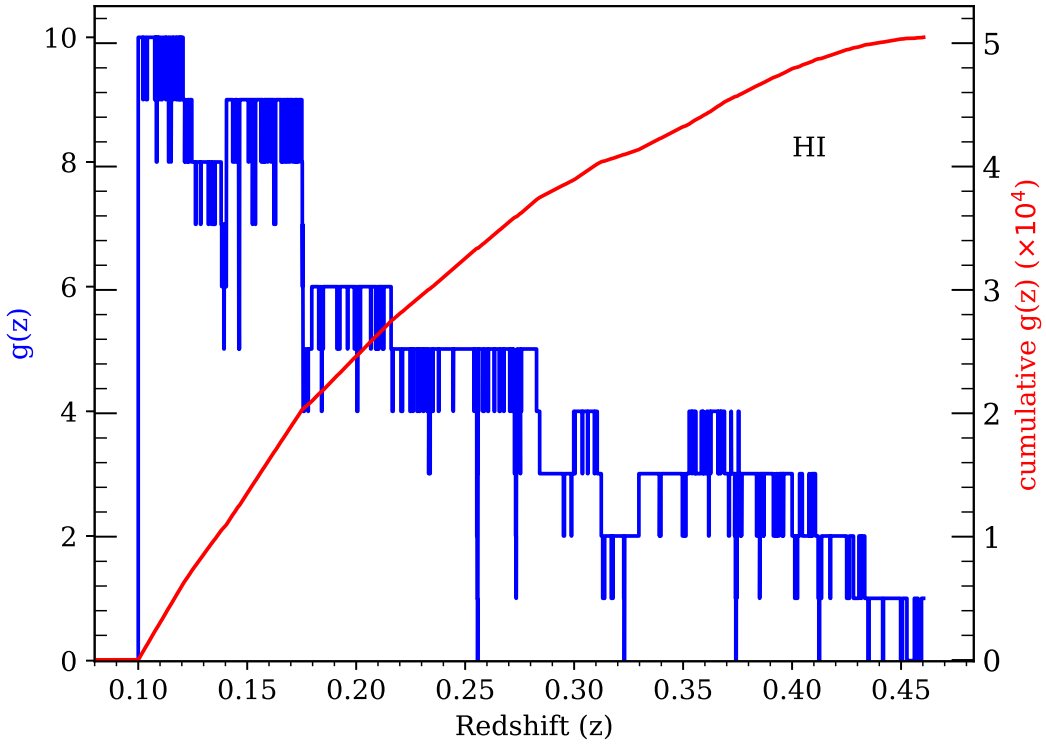

Figure 4.8: We show the full sightlines redshift path sensitivity function for our survey for H I (in blue) and cumulative $g(z)$ (in red) as a function of redshift for W_{min} = 0.03 Å.

Considering only the contribution to the redshift path of the portions of the spectrum that satisfy the constraints described in this subsection, we calculated the redshift path for each sightline. To calculate the redshift path of the survey, the contributions from each sightline were added. Consequently, we obtained the redshift path sensitivity functions and the cumulative $g(z)$, shown in Figures 4.8 (for H I) and 4.9 (for O VI).

Figure 4.8 depicts the redshift path sensitivity function ($g(z)$) for our survey (in blue) and its cumulative curve (in red) for neutral hydrogen (H I), considering the minimum equivalent width of W_{min} = 0.03 Å. In Figure 4.9, we show the redshift path sensitivity function for O VI. The $g(z)$ function is represented in a histogram, and the bins have the size of a single pixel of the spectrum. This function indicates the coverage at low redshifts, in the range $0.1 \leq z \leq 0.5$ for both ions, where our transitions are observed. For instance, Figure 4.8 shows that in our survey, at redshifts smaller than ≈ 0.12, we can find H I in the ten QSO sightlines, but O VI only in eight QSO sightlines, for the same redshifts. We also find a greater total coverage of O VI than of H I in our survey.

The total redshift path (Δz) of the survey is calculated by adding the contribution of the redshift path of each QSO, according to equation (4.5).

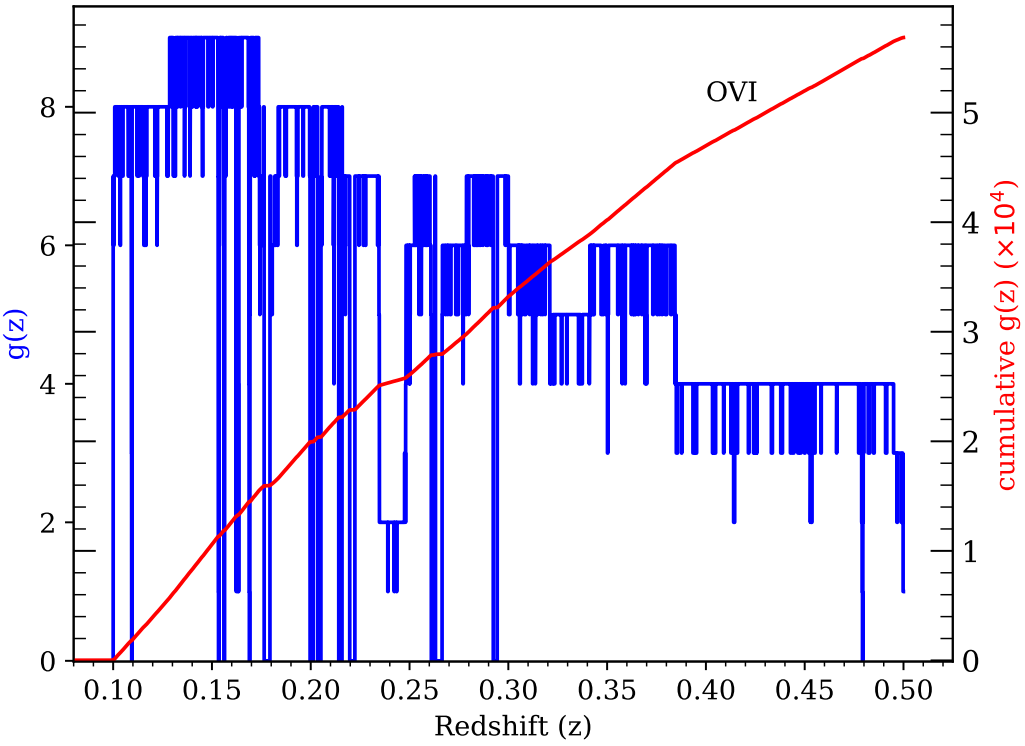

Figure 4.9: We show the full sightlines redshift path sensitivity function for our survey for O VI (in blue) and cumulative $g(z)$ (in red) as a function of redshift for W_{min} = 0.03 Å.

$$\Delta z = \int_0^\infty g(z)\mathrm{d}z, \tag{4.5}$$

where $\mathrm{d}z = \Delta\lambda_{pix}/\lambda_r$, is the redshift value corresponding to a single pixel, $\Delta\lambda_{pix} = 0.0395$ Å, λ_r is the rest-frame wavelength of the transition representing the system being surveyed, in our case H I ($\lambda_r = 1215.67$ Å) and O VI ($\lambda_r = 1031.9261$ Å), and $g(z)$ is the redshift path sensitivity function calculated for the survey, following the constrains indicated above in this section.

Figure 4.10 shows the total redshift path of the survey across the entire sample for H I and O VI detections, shown in black and green, respectively. In Figure 4.11, we show the total redshift path corresponding to regions of our survey spectra within rest-frame velocity differences $\Delta v = \pm 1000$ km s^{-1} from their cluster-pairs at impact parameter $\Delta d \leq 3$ Mpc. It is important to highlight that the dependence on the equivalent width in Figures 4.10 and 4.11 comes from the restriction of equations (4.3) and (4.4) because of the relationship between W_r and the S/N of the spectra. The redshift path is shown as a function of the minimum rest-frame equivalent width W_r^{min}. The vertical dashed line marks the minimum rest-frame equivalent width selected to analyze our detections, 0.03 Å. This value corresponds to high completeness levels, which means that we choose the W_r^{min} so that Δ_z is approximately constant for $W_r > W_r^{min}$. For that reason, we adopted it as the minimum equivalent width for our analysis. The targeted redshift path of our survey, at the selected minimum equivalent width, is 1.64 for H I, and 2.18 for O VI.

4.1.2 Redshift number density

We estimated the redshift number density of absorption lines ($d\mathcal{N}/dz$), which is the number of absorbers detected for a given species per unit redshift. We used this to characterize inter-cluster filaments, as a function of a rest-frame velocity window (Δv) around the redshift of the 25 independent cluster-pairs. Following Tejos et al. 2016, to estimate the redshift number density, we counted $\mathcal{N}(\Delta d, \Delta v, W_r^{min})$ as the number of absorption components found within Δv from the identified cluster-pair, having rest-frame equivalent widths $W_r \geq W_r^{min}$, and considering only cluster-pairs with a distance between the intercluster-axis and QSO sightline smaller than Δd. Then the redshift number density is calculated by equation (4.6):

$$\frac{\mathrm{d}\mathcal{N}}{\mathrm{d}z}(\Delta d, \Delta v, W_r^{min}) = \frac{\mathcal{N}(\Delta d, \Delta v, W_r^{min})}{\Delta z(\Delta d, \Delta v, W_r^{min})} \tag{4.6}$$

The uncertainty in the redshift number density is dominated by the Poissonian uncertainty in $\mathcal{N}$ (Tejos et al. 2016). For low-number statistics, we approximate the upper ($\sigma^+_{\mathcal{N}}$) and lower ($\sigma^-_{\mathcal{N}}$) uncertainties in the number of absorption components by equation (4.7)

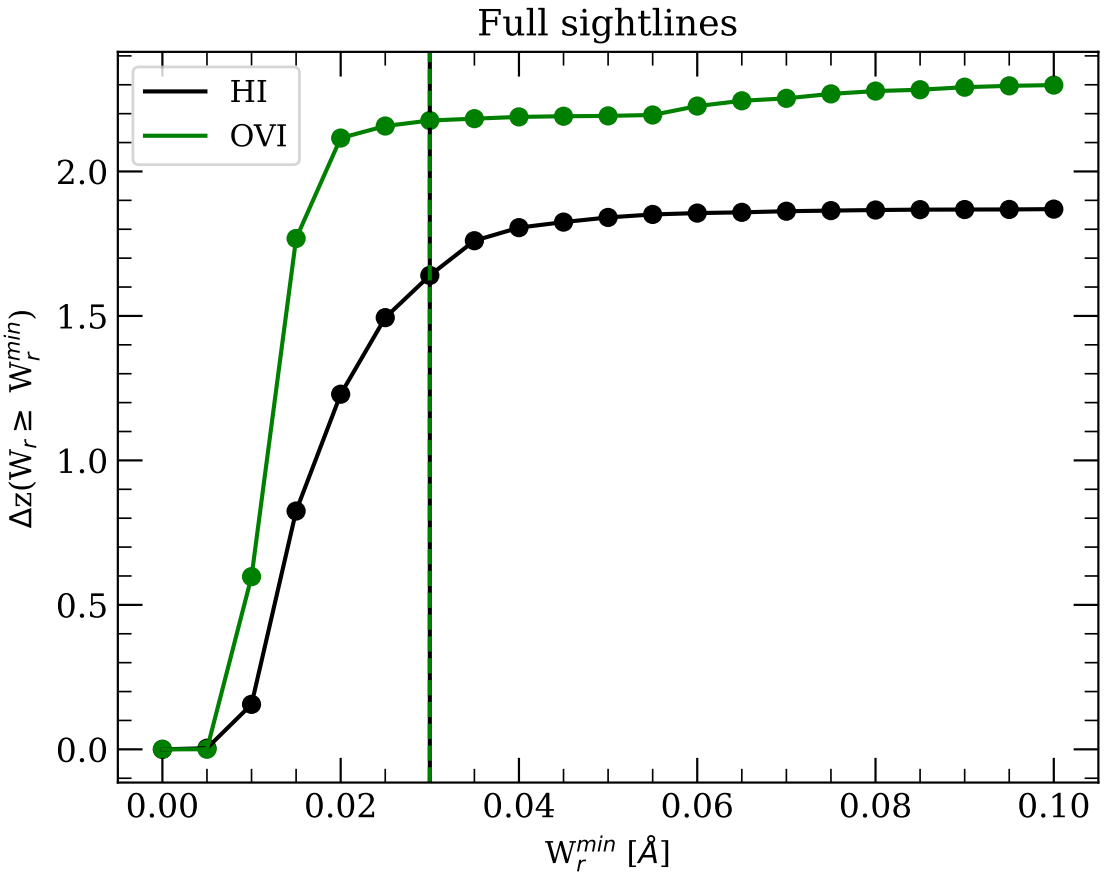

Figure 4.10: Redshift path of H I in black, and O VI in green, shown as a function of the minimum rest-frame equivalent width, W_r^{min}, across the entire sample. The vertical dashed line marks the minimum rest-frame equivalent width that we include in our analysis, 0.03 Å.

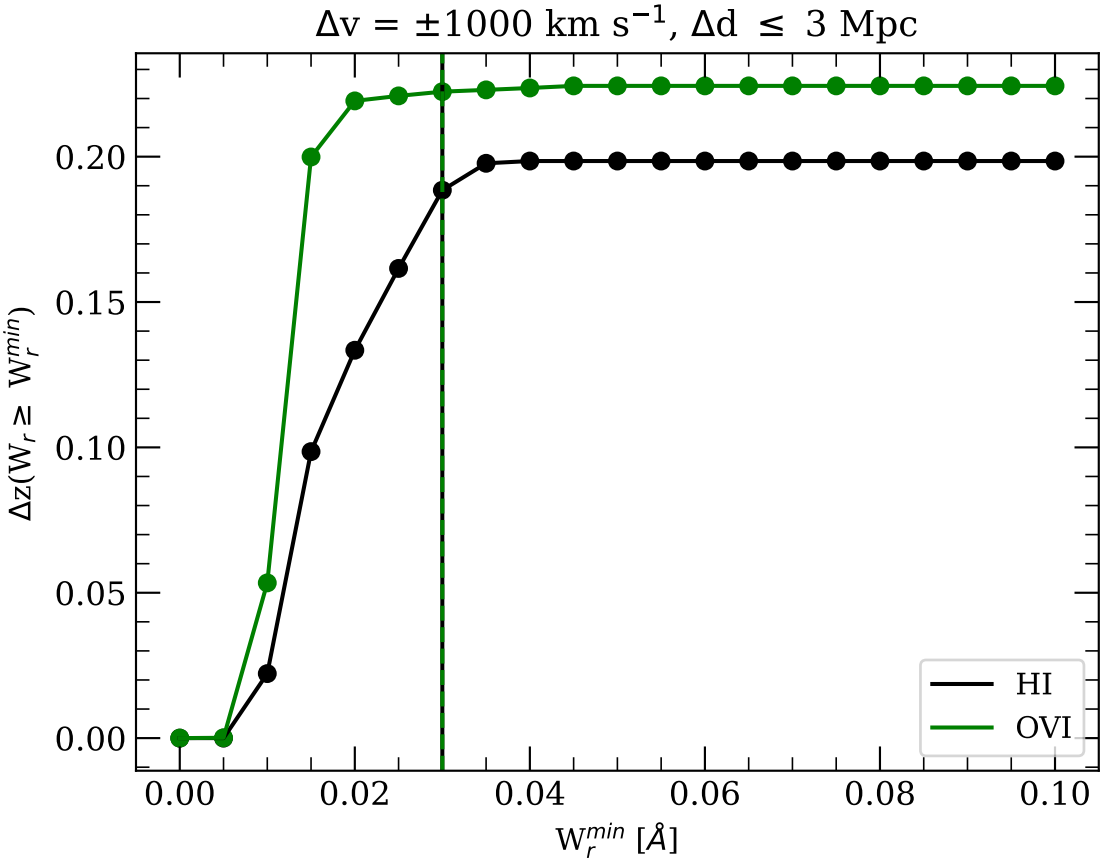

Figure 4.11: Corresponding redshift path of H I in black, and O VI in green, shown as a function of the minimum rest-frame equivalent width, W_r^{min}, associated with regions of our sample spectra with rest-frame velocity differences of $\Delta v = \pm 1000$ km s^{-1} from their cluster-pair at impact parameters smaller than $\Delta d = 3$Mpc. The vertical dashed line marks the minimum rest-frame equivalent width that we include in our analysis, 0.03 Å.

(Gehrels 1986):

$$\sigma_N^+ \approx \sqrt{N + 3/4} + 1\sigma_N^- \approx \sqrt{N - 1/4} \tag{4.7}$$

The redshift number density of the field ($d\mathcal{N}/dz|_{field}$) characterizes the specific absorption strength of a given species in the IGM, and it is determined from randomly selected sightlines. This value allows for a comparison of $d\mathcal{N}/dz$ for a particular species with the typical level of absorption expected in the field for that same species. To estimate the expected field value for our survey, we used equation (4.8).

$$\left.\frac{d\mathcal{N}}{dz}\right|_{field} \approx \frac{\mathcal{N}_{tot}}{\Delta z_{full}}, \tag{4.8}$$

where $\mathcal{N}_{tot}$ is the total number of absorption lines of the analyzed absorber in the survey, restricted to the range $0.1 \leq z \leq 0.5$, and Δz_{full} is the redshift path also at those redshift limits [1]. The estimation of the statistical uncertainty in the expected field is taken from the contribution of the Poissonian uncertainty of $\mathcal{N}_{tot}$ using equation (4.7).

Additionally, we have estimated the $d\mathcal{N}/dz|_{field_D}$ for H I, which is the redshift number density of the expected field according to the survey of Danforth et al. 2016, which was calculated with equation (4.9) from a sample of 82 UV-bright active galactic nuclei (AGN). We used this quantity as a comparison with our own estimation, based on equation (4.8).

$$\left.\frac{d\mathcal{N}(>N)}{dz}\right|_{field} = C_{14}\left(\frac{N}{10^{14} cm^{-2}}\right)^{-(\beta-1)}, \tag{4.9}$$

where N is the average column density of the lowest 5% absorptions of a specific ion species (the average was taken to avoid outliers). We consider absorptions with a significance level (SL) ≥ 10 (Danforth et al. 2016) and with a fit concern of 0, indicating that there is no doubt the detection corresponds to the specific identified ion species (Danforth et al. 2016). The normalization constant C_{14} and β are fitting parameters. The best-fitting values for these constants have been reported in the literature for studies of differential distribution of absorbers for $12 \leq \log(N/cm^2) \leq 17$. For H I, the reported values are $\beta = 1.67 \pm 0.01$, and $C_{14} = 23 \pm 1$ (Danforth et al. 2016). The uncertainties are calculated using error propagation of the uncertainties in the fit parameters following equation (4.9). For O VI, the expected field is derived directly from Danforth et al. 2016 [2].

[1] Because the survey sightlines were selected to probe filaments, the expected field could alternatively be calculated by excluding regions near cluster pairs. Nevertheless, our current estimations of the expected field remain consistent with established literature (Danforth et al. 2016). Furthermore, an analysis excluding these cluster-adjacent regions yields values that are consistent with the reported results within the calculated uncertainties. Notably, such an exclusion would reduce the expected field value, thereby amplifying the observed relative excesses, particularly for BLAs and O VI, and further reinforcing the primary conclusions of this study.

[2] Since Danforth et al. 2016 does not provide explicit values for the fitting parameters to calculate the

We determine the incidence of the tracers as the redshift number density of the total neutral hydrogen H I, O VI, BLAs, and NLAs. The results and discussion of our analysis and characterization are shown in the next sections.

4.2 Results and Discussion

We obtained the redshift number density of our survey for the total H I, NLA, BLA, and O VI components around cluster-pairs and determined the relative excesses of these samples with respect to their respective expected field values.

4.2.1 Redshift number density of the survey

Figures 4.12- 4.15 present the redshift number density of our survey (total H I is shown in brown while O VI in green). In Figures 4.12 and 4.14, we show the redshift number density as a function of the rest-frame velocity window (Δv), for a fixed $\Delta d \leq 3$ Mpc. In Figures 4.13 and 4.15, we observe the redshift number density as a function of the impact parameter (Δd), for a fixed velocity window of $\Delta v = \pm 1000$ km s^{-1}. The ranges selected for the maximum velocity window and the maximum impact parameter[3] were chosen to cover most of the spectrum in each sightline. The bins are not independent of each other, as emphasized by the colored areas. The $d\mathcal{N}/dz|_{field_D}$ with associated uncertainties given by Danforth et al. 2016 is shown in a black hashed region, and our $d\mathcal{N}/dz|_{field}$, from equation (4.9), is shown in gray. Our estimate of the expected field is consistent with that obtained from Danforth et al. 2016.

Fixing $\Delta v = \pm 1000$ km s^{-1} for H I and O VI, the redshift number density reaches its maximum approximately value when $\Delta d \leq 3$ Mpc. This behavior motivated our adopted fiducial value of 3 Mpc for the maximum impact parameter. For O VI, the trend decreases with decreasing Δd in the region $\Delta d \leq 3$ Mpc. Fixing the impact parameter, the redshift number density generally decreases with increasing velocity window. We also show that when the rest-frame velocity window and the impact parameter increase, the $d\mathcal{N}/dz$ approaches the average field value, as expected.

Figures 4.16-4.19 show the redshift number density for a sample of BLAs and NLAs as a function of the velocity window and impact parameter. In Figures 4.16 and 4.17, we

redshift number density of the field, we estimate it using the $\log N$ ranges, the number of O VI absorptions identified, $\mathcal{N}_{OVI}$, and the redshift path for O VI, Δz_{OVI}, reported in Table 5 of Danforth et al. 2016. Within the range of $\log N$ adopted in this work, using the corresponding values of $\mathcal{N}_{OVI}$, and Δz_{OVI}, we compute the redshift number density of O VI according to $\left.\frac{d\mathcal{N}(>N)}{dz}\right|_{field_D} = \sum_{j=1}^{\mathcal{N}_{OVI}} \frac{1}{\Delta z_{\mathrm{O\,VI},\,j}}$, and we estimate the uncertainties using $\sigma^2 = \sum_{j=1}^{\mathcal{N}_{OVI}} \frac{1}{\Delta z^2_{\mathrm{O\,VI},\,j}}$.

[3] A greater impact parameter threshold increases the number of identified cluster-pairs associated with a QSO sightline, which increases the spectral coverage.

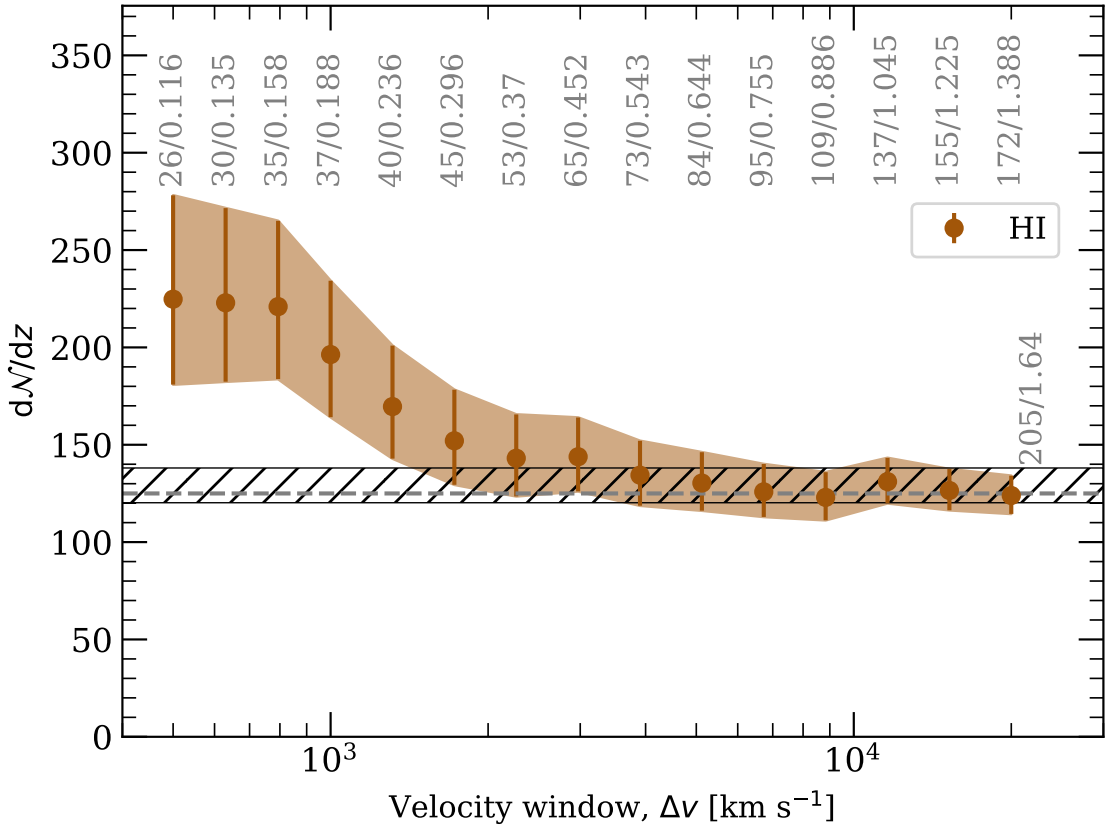

Figure 4.12: Redshift number density of our survey for total H I in brown. Here, we show the redshift number density as a function of the rest-frame velocity window (Δv), for a fixed $\Delta d \leq 3$ Mpc. At the top of each datapoint, we indicate the total number of absorption lines detected and the redshift paths per bin in gray numbers. The expected field value estimated for our survey, $d\mathcal{N}/dz|_{field}$, is shown in the gray horizontal dashed line, and its value is indicated in the gray numbers at the end of the dashed line. The expected field value estimated from Danforth et al. 2016 is shown in the black hashed region for comparison.

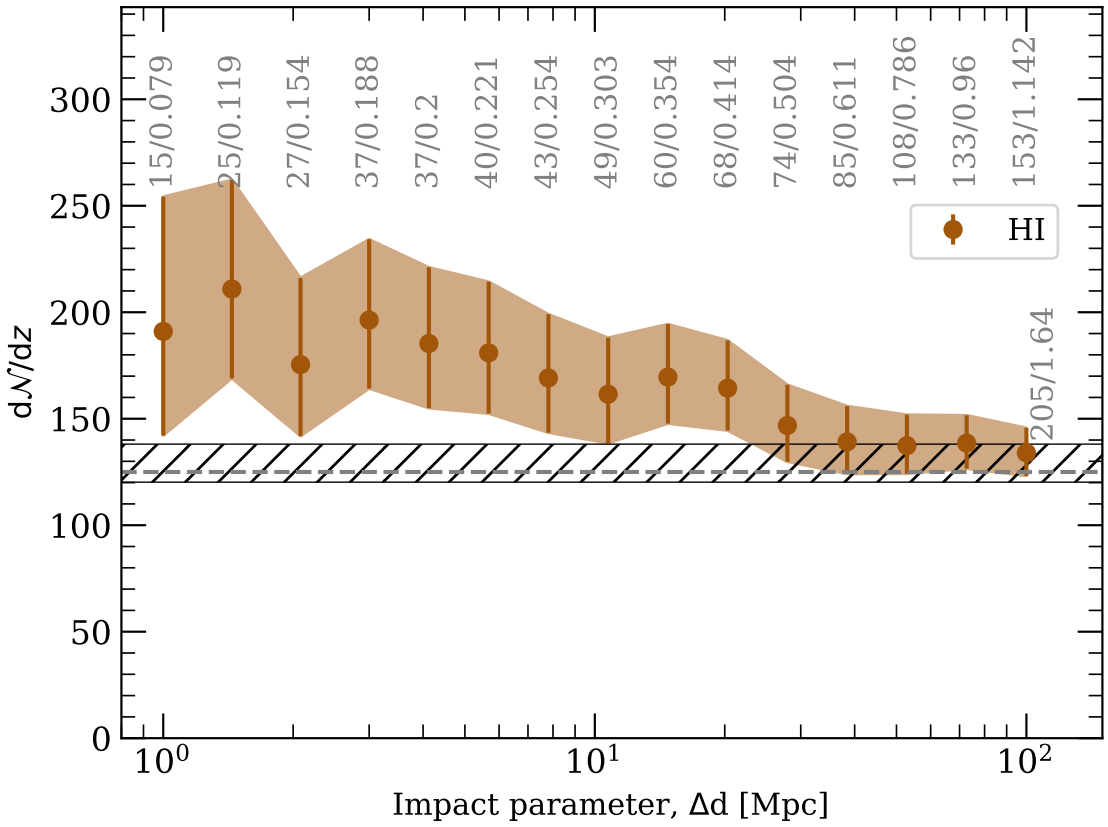

Figure 4.13: Redshift number density of our survey for total H I in brown, we show the redshift number density as a function of the impact parameter (Δd), for a fixed value of rest-frame velocity window $\Delta v = \pm 1000$ km s^{-1}. At the top of each datapoint, we indicate the total number of absorption lines detected and the redshift paths per bin in gray numbers. The expected field value estimated for our survey, $d\mathcal{N}/dz|_{field}$, is shown in the gray horizontal dashed line, and its value is indicated in the gray numbers at the end of the dashed line. The expected field value estimated from Danforth et al. 2016 is shown in the black hashed region for comparison.

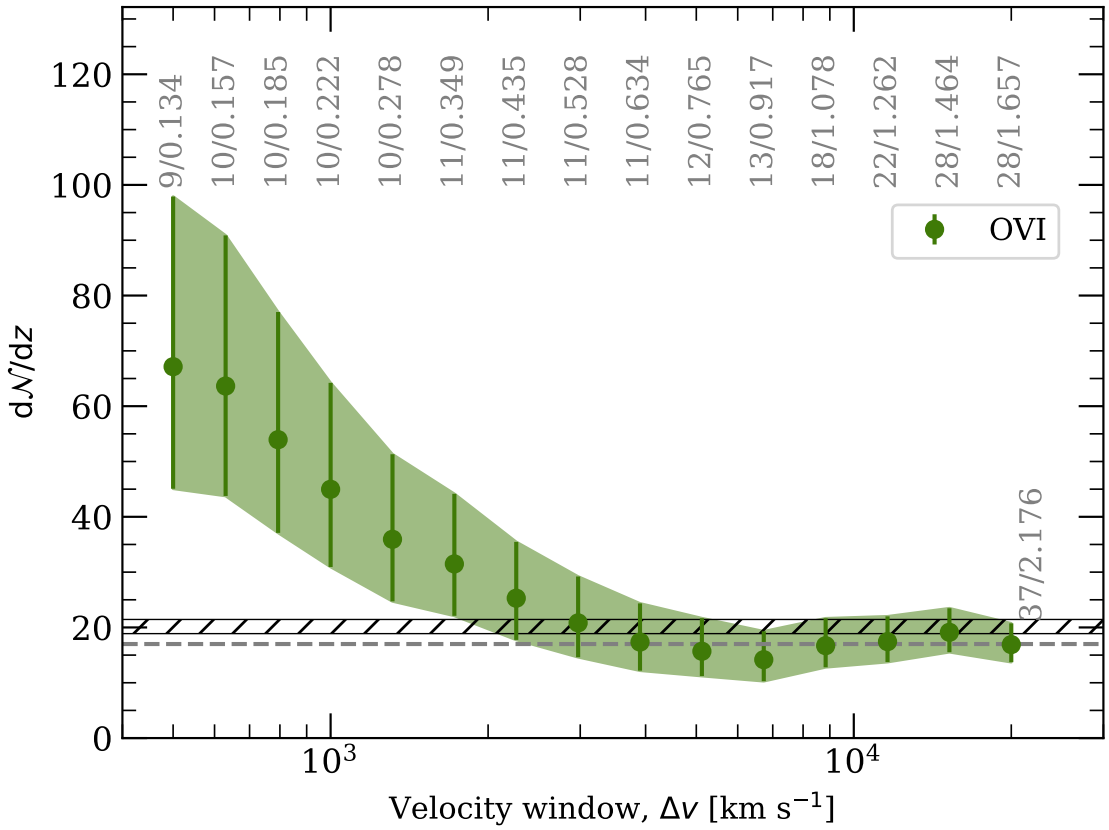

Figure 4.14: Redshift number density of our survey for O VI in green. We show the redshift number density as a function of rest-frame velocity window (Δv), for a fixed $\Delta d \leq 3$ Mpc. At the top of each datapoint, we indicate the total number of absorption lines detected and the redshift paths per bin in gray numbers. The expected field value estimated for our survey, $dN/dz|_{field}$, is shown in the gray horizontal dashed line, and its value is indicated in the gray numbers at the end of the dashed line. The expected field value estimated from Danforth et al. 2016 is shown in the black hashed region for comparison.

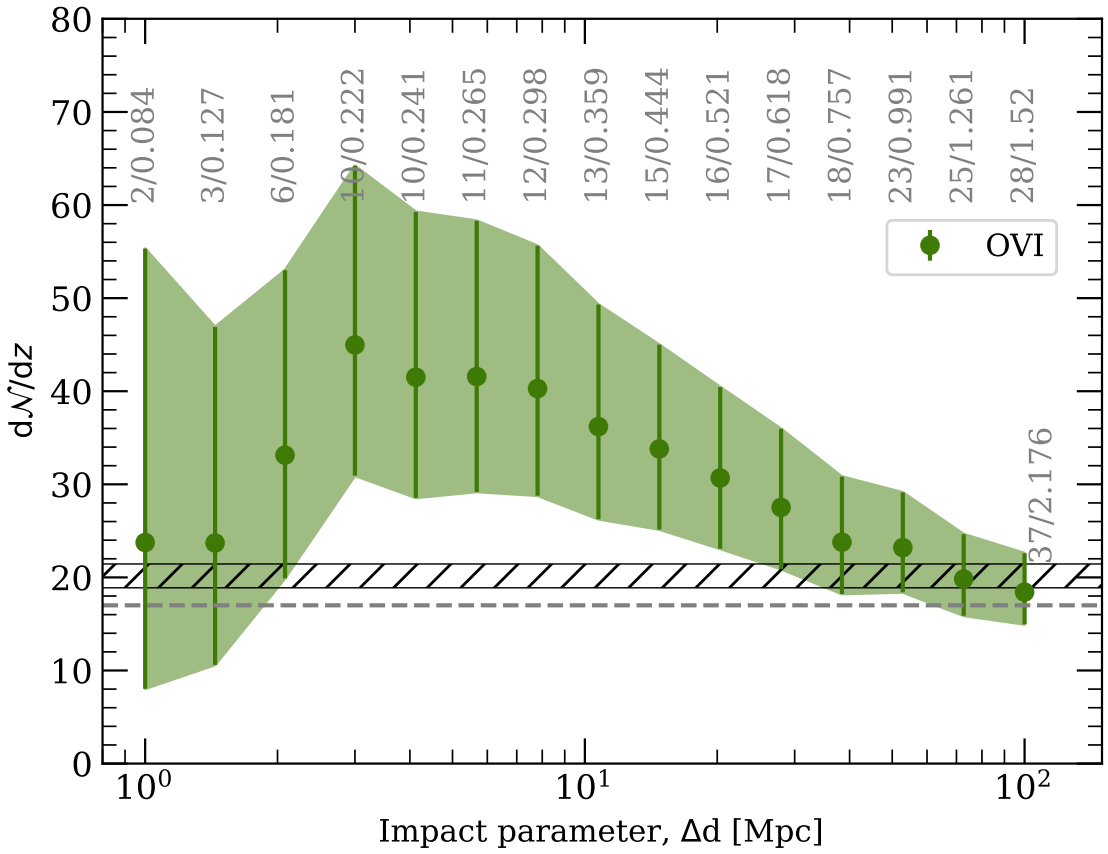

Figure 4.15: Redshift number density of our survey for O VI in green, we show the redshift number density as a function of the impact parameter (Δd), for a fixed value of rest-frame velocity window $\Delta v = \pm 1000$ km s^{-1}. At the top of each datapoint, we indicate the total number of absorption lines detected and the redshift paths per bin in gray numbers. The expected field value estimated for our survey, $dN/dz|_{field}$, is shown in the gray horizontal dashed line, and its value is indicated in the gray numbers at the end of the dashed line. The expected field value estimated from Danforth et al. 2016 is shown in the black hashed region for comparison.

show the redshift number density for the sample of NLAs colored in blue. In Figures 4.18 and 4.19, we show the redshift number density for the sample of BLAs colored in red. In Figures 4.17 and 4.19, we show $d\mathcal{N}/dz$ as a function of the rest-frame velocity window Δv for a fixed value of the impact parameter $\Delta d \leq 3$ Mpc. And in Figures 4.17 and 4.19, we show the redshift number density as a function of the impact parameter Δd for a fixed velocity window $\Delta v = \pm 1000$ km s^{-1}. For the NLAs sample, the uncertainties are smaller than for the BLAs sample because we detected more absorptions: NLAs (154) and BLAs (59). Here, we also show that for a fixed value of $\Delta d \leq 3$ Mpc, the redshift number density generally decreases as the rest-frame velocity window increases. Finally, it is worthwhile to highlight that in Figures 4.12- 4.19, the $d\mathcal{N}/dz$ approaches the expected field as both the rest-frame velocity window and impact parameter increase, as expected. This behaviour arises because increasing the rest-frame velocity window or the impact parameter corresponds to analyzing a broader portion of the sightline, thereby reducing the restriction to regions around the cluster-pairs and corresponding more to the field (see equation (4.8)).

4.2.2 Relative excess of the survey with respect to the field

Using the redshift number density of each sample of interest (H I, O VI, BLAs, and NLAs), we estimate the relative excess of our absorption line samples compared to their respective field expectations. Following Tejos et al. 2016, we defined this as $\frac{d\mathcal{N}}{dz}/\frac{d\mathcal{N}}{dz}|_{field}$. In Figures 4.20-4.23, we show these excesses for the four samples of study.

We present the relative excess of the redshift number densities as a function of the rest-frame velocity window (in Figures 4.20 and 4.22), and the impact parameter around the independent cluster-pairs (in Figures 4.21 and 4.23). In Figures 4.20 and 4.21, we show the excess for the total H I (colored in brown filled circles) and O VI (colored in green filled circles). In Figures 4.22 and 4.23, we show the excess for the sample of NLAs (blue filled circles) and BLAs (red filled circles). Colored-shaded areas show the $\pm 1\sigma$ statistical uncertainties. For the fiducial values ($\Delta v = \pm 1000$ km s^{-1} and $\Delta d \leq 3$ Mpc), the excess is approximately ~ 1.6 for the sample of H I and ~ 3 for the sample of O VI, with respect to each expected field. Figures 4.22 and 4.23 indicate that the excess of BLAs is slightly (but consistently) greater compared to the excess of NLAs at any velocity window and impact parameter, particularly at the fiducial values, $\Delta v = \pm 1000$ km s^{-1} and $\Delta d \leq 3$ Mpc. Additionally, the error bars for NLAs are smaller than those for BLAs because we detected more NLAs than BLAs in our survey.

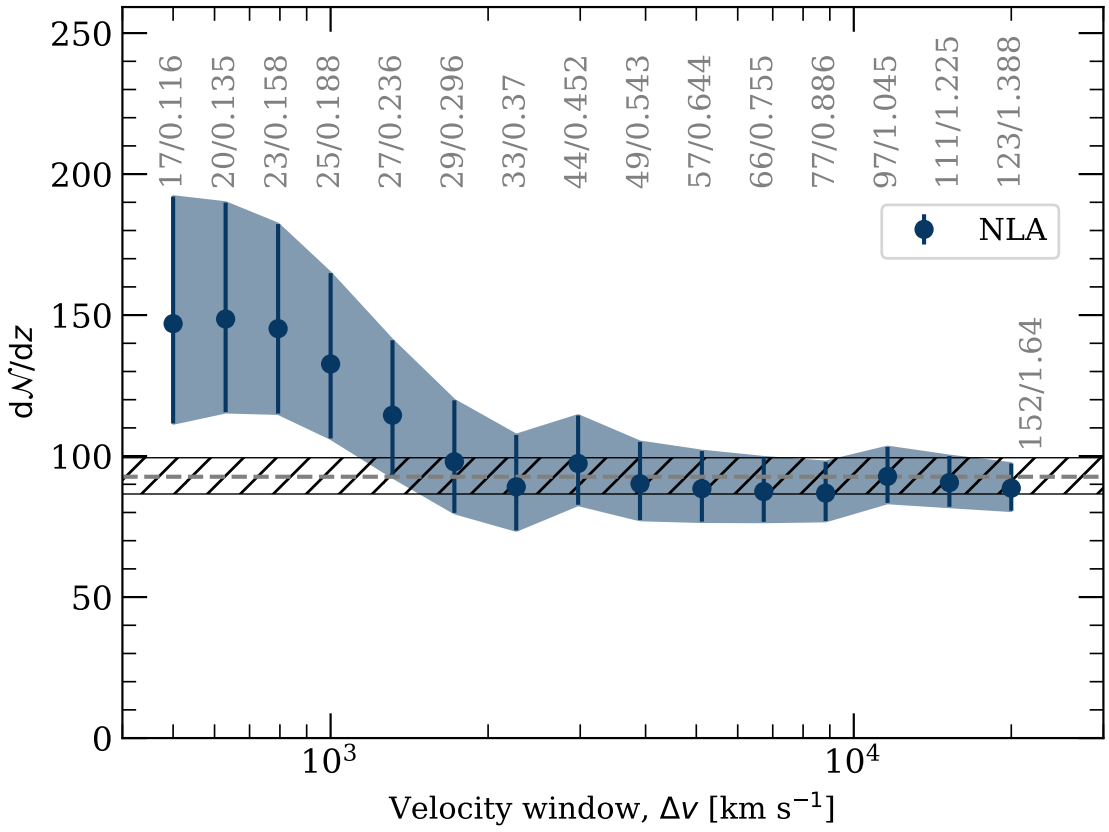

Figure 4.16: Redshift number density of our survey for NLA in blue. We show the redshift number density as a function of rest-frame velocity window (Δv), for a fixed $\Delta d \leq 3$ Mpc. At the top of each datapoint, we indicate the total number of detected absorption lines and the redshift paths per bin in gray numbers. The expected field value estimated for our survey, $d\mathcal{N}/dz|_{field}$, is shown in the gray horizontal dashed line, and its value is indicated in the gray numbers at the end of the dashed line. The expected field value estimated from Danforth et al. 2016 is shown in the black hashed region for comparison.

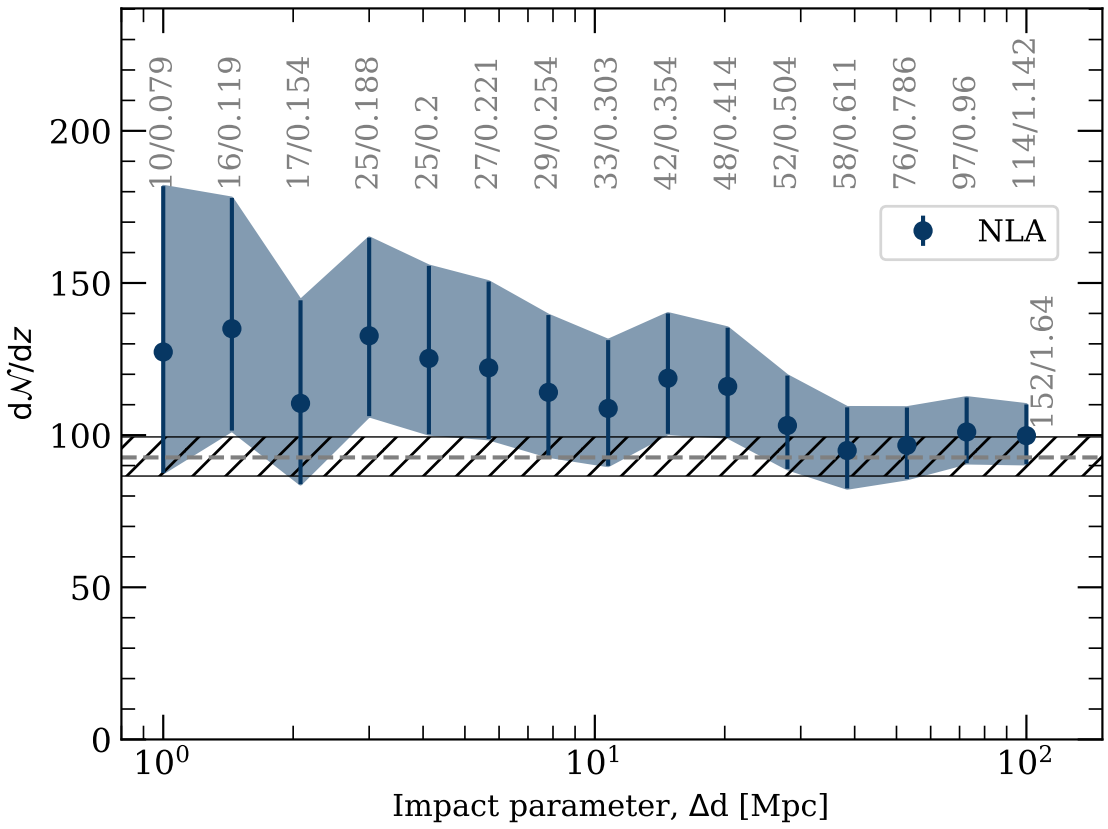

Figure 4.17: Redshift number density of our survey for NLA in blue. We show the redshift number density as a function of the impact parameter (Δd) for a fixed rest-frame velocity window of $\Delta v = \pm 1000$ km s^{-1}. At the top of each datapoint, we indicate the total number of detected absorption lines and the redshift paths per bin in gray numbers. The expected field value estimated for our survey, $d\mathcal{N}/dz|_{field}$, is shown in the gray horizontal dashed line, and its value is indicated in the gray numbers at the end of the dashed line. The expected field value estimated from Danforth et al. 2016 is shown in the black hashed region for comparison.

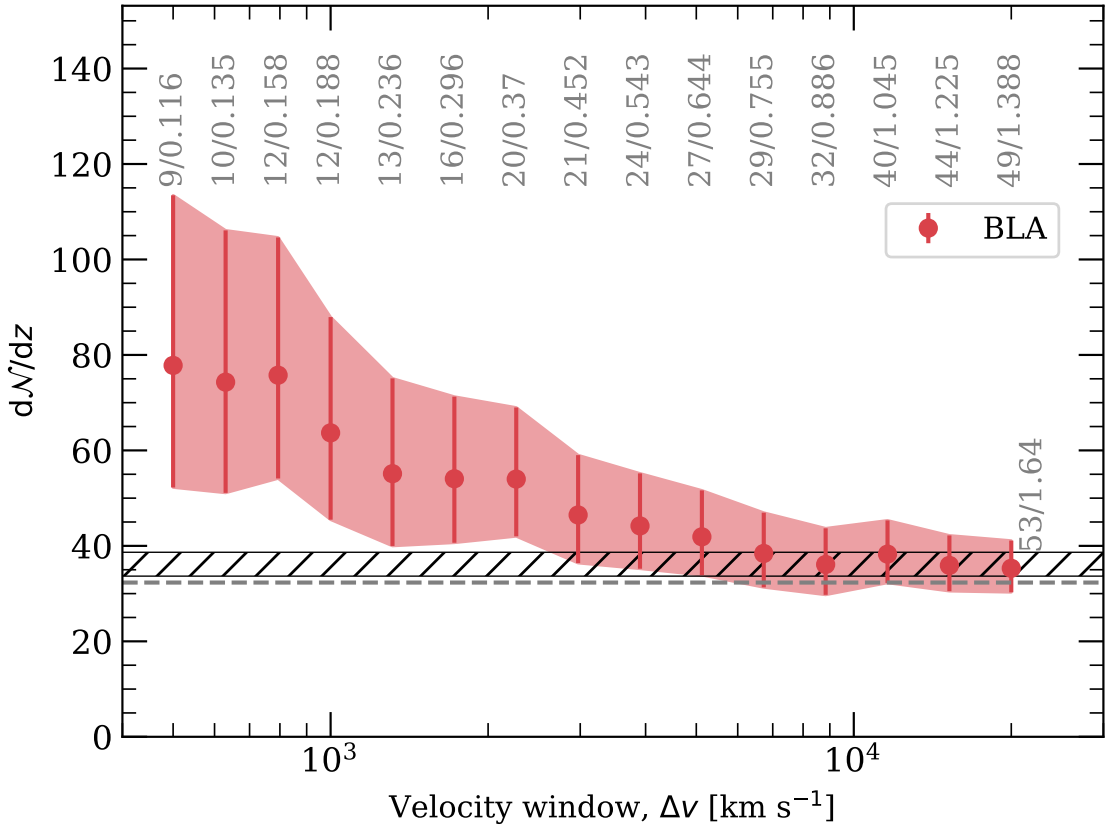

Figure 4.18: Redshift number density of our survey for BLA in red. We show the redshift number density as a function of rest-frame velocity window (Δv), for a fixed $\Delta d \leq 3$ Mpc. We show the redshift number density as a function of the impact parameter (Δd) for a fixed rest-frame velocity window of $\Delta v = \pm 1000$ km s^{-1}. At the top of the datapoints in each panel, we indicate the total number of detected absorption lines and the redshift paths per bin in gray numbers. The expected field value estimated for our survey, $d\mathcal{N}/dz|_{field}$, is shown in the gray horizontal dashed line, and its value is indicated in the gray numbers at the end of the dashed line. The expected field value estimated from Danforth et al. 2016 is shown in the black hashed region for comparison.

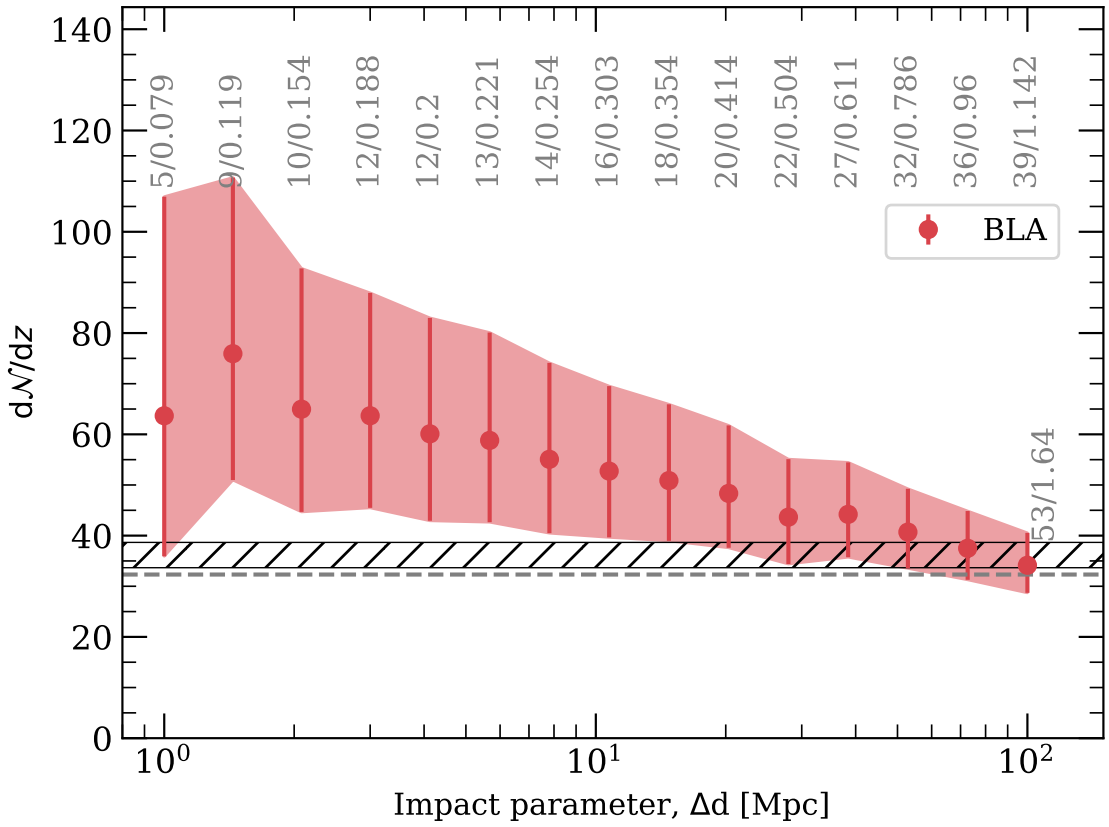

Figure 4.19: Redshift number density of our survey for BLA in red. We show the redshift number density as a function of the impact parameter (Δd) for a fixed rest-frame velocity window of $\Delta v = \pm 1000$ km s^{-1}. At the top of each datapoint, we indicate the total number of detected absorption lines and the redshift paths per bin in gray numbers. The expected field value estimated for our survey, $dN/dz|_{field}$, is shown in the gray horizontal dashed line, and its value is indicated in the gray numbers at the end of the dashed line. The expected field value estimated from Danforth et al. 2016 is shown in the black hashed region for comparison.

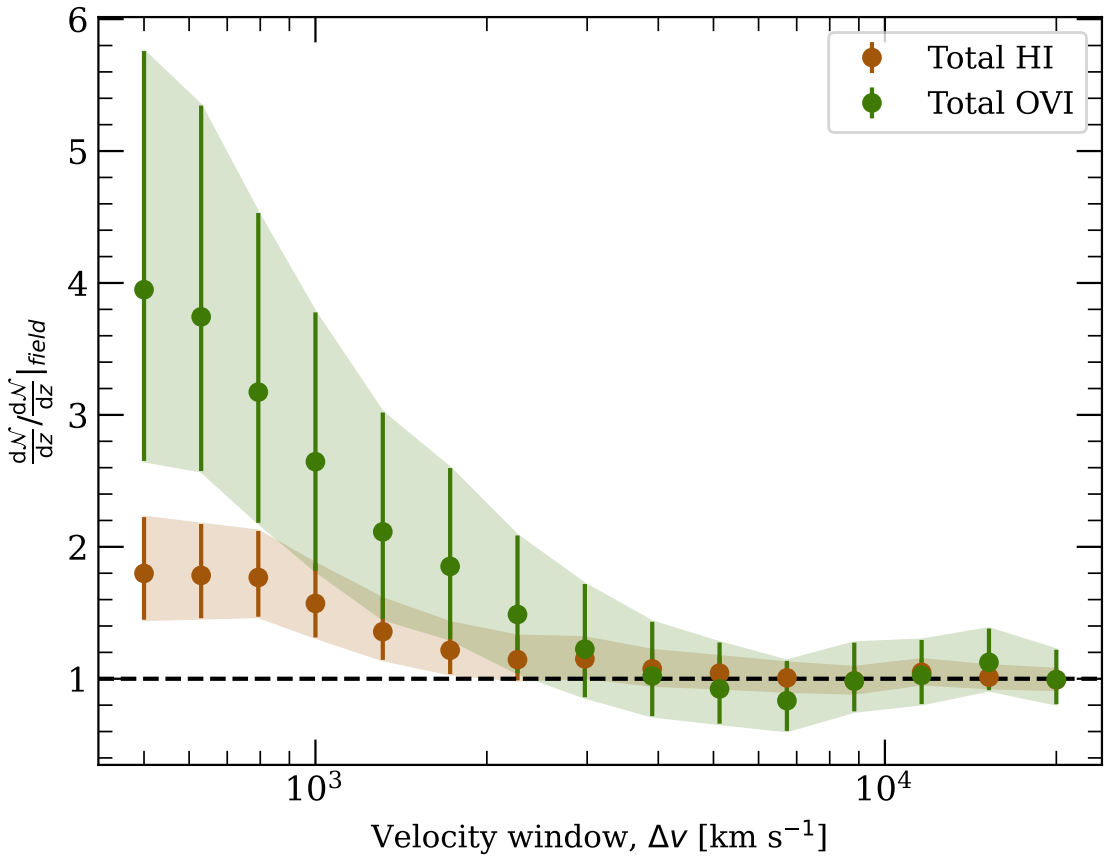

Figure 4.20: Relative excesses of redshift number densities compared to the expected field, as a function of rest-frame velocity window (Δv), for a fixed $\Delta d \leq 3$ Mpc. We show the excess for the absorption line samples of total H I in brown, and for O VI in green.

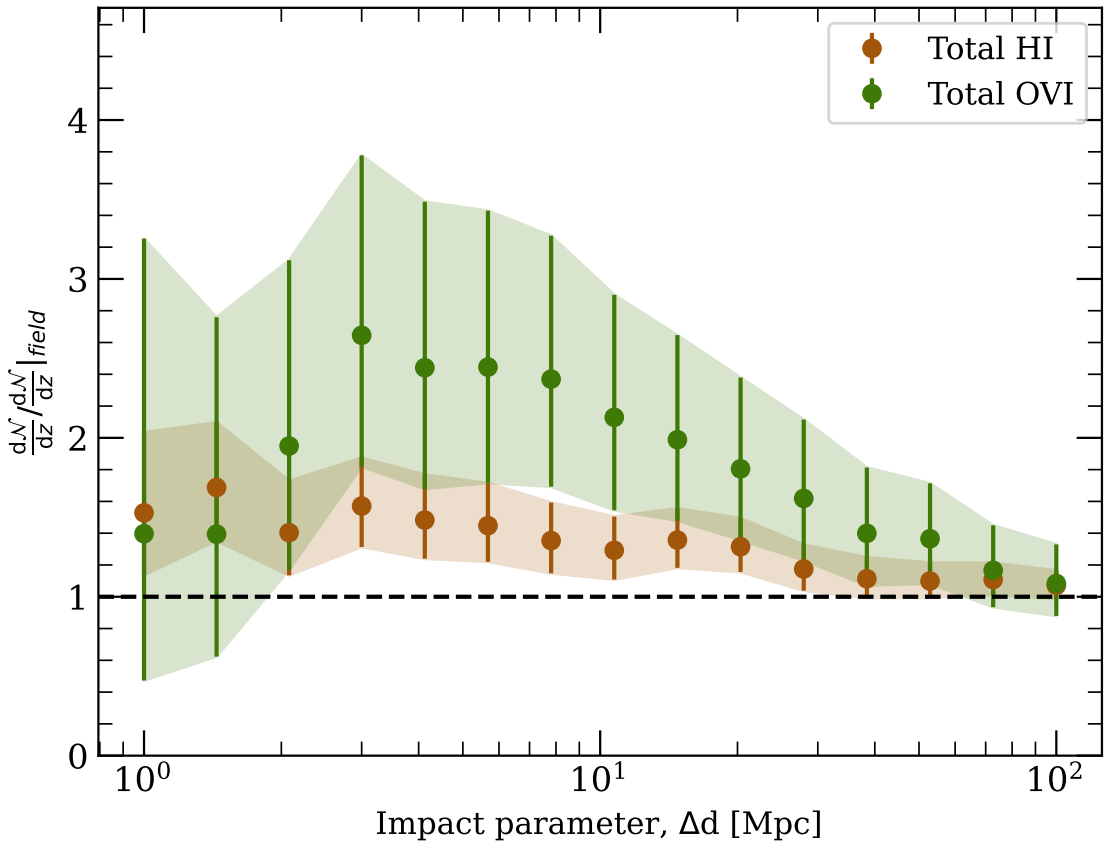

Figure 4.21: Relative excesses of redshift number densities compared to the expected field, as a function of the impact parameter (Δd), for a fixed rest-frame velocity window $\Delta v = \pm 1000$ km s^{-1}. We show the excess for the absorption line samples of total H I in brown, and for O VI in green.

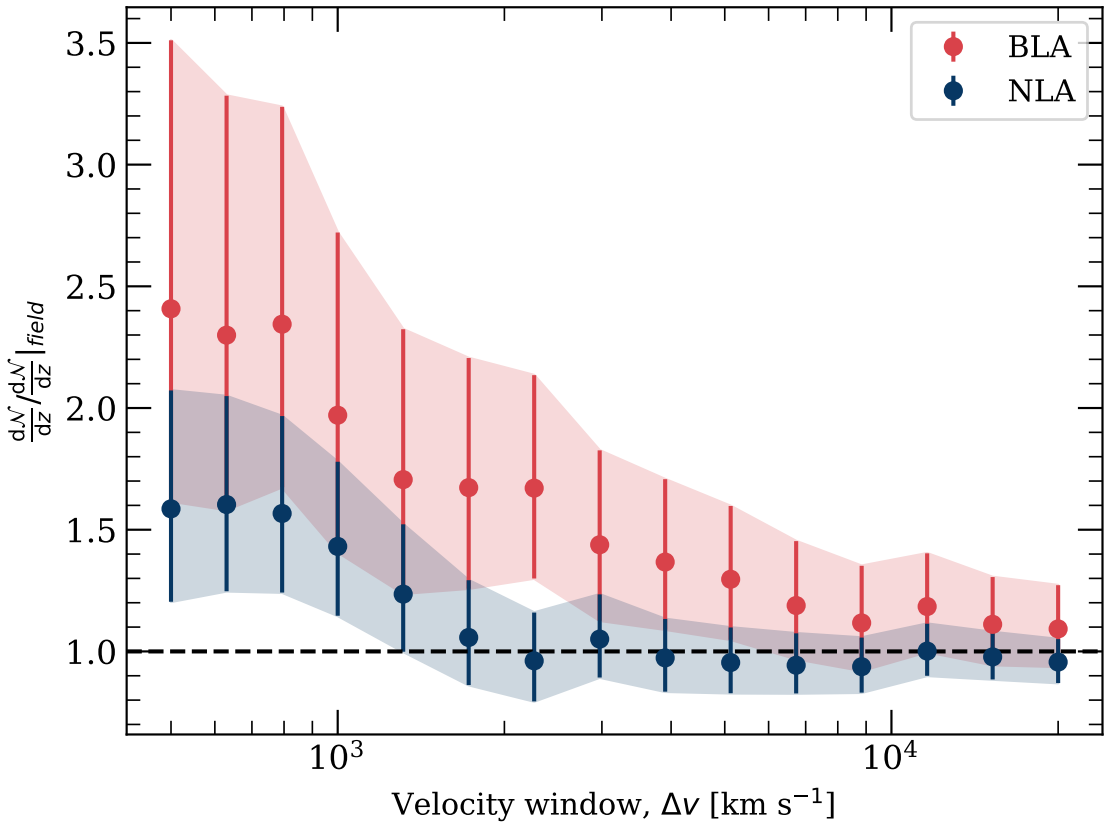

Figure 4.22: Relative excesses of redshift number densities compared to the expected field, as a function of rest-frame velocity window (Δv), for a fixed $\Delta d \leq 3$ Mpc. We indicate the excess for absorption line samples of H I, NLA in blue, and BLAs in red.

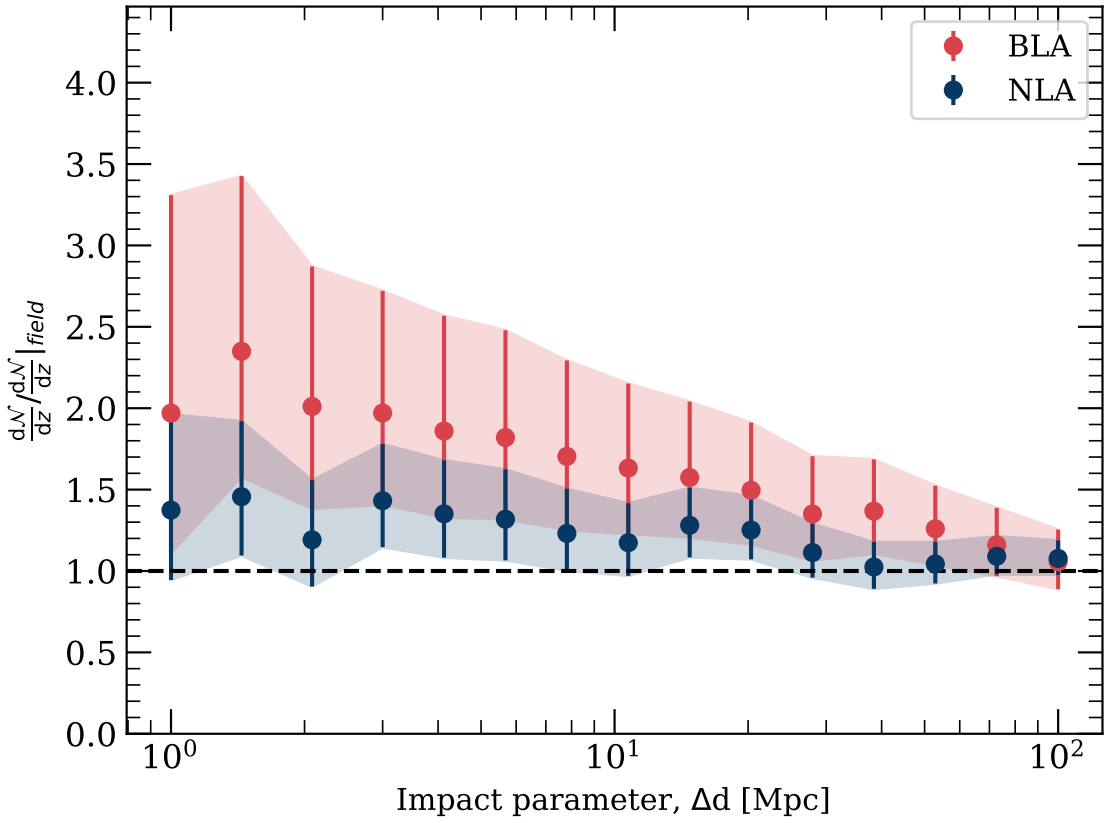

Figure 4.23: Relative excesses of redshift number densities compared to the expected field, as a function of the impact parameter (Δd), for a fixed rest-frame velocity window $\Delta v = \pm 1000$ km s^{-1}. We indicate the excess for absorption line samples of H I, NLA in blue, and BLAs in red.

4.2.3 Discussion

The redshift number density reported in this study tends to increase at smaller rest-frame velocity windows, as we can see in Figures 4.12, 4.14, 4.16, and 4.18. However, as the rest-frame velocity window becomes smaller, the sample size decreases, thereby increasing the statistical uncertainties (Tejos et al. 2016). Additionally, we found that the relative excess of O VI is approximately twice the excess of H I (see Figure 4.20), which is in agreement with a previous case study Tejos et al. 2016, based on a single sightline. For the O VI sample, we obtained the largest relative excess compared to the field (approximately 2.6) at $\Delta v = \pm 1000$ km s^{-1} and $\Delta d \leq 3$ Mpc; however, this sample has larger statistical uncertainties compared to total H I, due to its small number of detections. Even though our uncertainties are large, they remain smaller than those reported by Tejos et al. 2016. Additionally, the relative excess of the incidence of BLAs is systematically higher than that of NLAs. This behaviour is expected if BLAs and NLAs are not probing similar physical conditions (Tejos et al. 2016). Indeed, a WHIM signature associated with inter-cluster filaments includes the detection of a relative excess of WHIM tracers (BLAs and O VI) higher than that of cold gas tracers (NLAs) (Tepper-García et al. 2012), in line with our findings.

Figures 4.24 and 4.25 indicate the location of the 25 independent cluster-pairs of our survey, relative to their corresponding QSO sightline, and their corresponding absorption features detected. This representation enables an assessment of the proximity between the regions probed by the survey sightlines and nearby galaxy clusters, to discuss possible origins to which the observed gas excesses may be attributed. In the y-axis, we indicate the impact parameter to a given independent cluster-pair, Δd; while the x-axis indicates the distance from the closest galaxy cluster in a given cluster-pair to the QSO sightline along the inter-cluster axis, referred to as Δx (see Figure 2.1). Additionally, the approximately virial radii expected for the sample of clusters are shown as a quarter-dashed circumference of radii 1 Mpc (Tejos et al. 2016), centered at the origin. We observe that the vast majority of sightlines are probing regions far away from the virial radii of known galaxy clusters, ruling out that the detected excess of the gas can be attributed to galaxy clusters/groups or individual galaxy halos. Filled symbols correspond to regions of the sightline showing absorption lines of the sample indicated in each panel, within Δv from the redshifts of a given independent cluster-pair. The size of the symbols is proportional to the number of absorption lines found. Empty symbols correspond to regions of the sightline showing no absorptions. Regions where the spectra do not allow identification of a particular transition are excluded. Therefore, only the data points corresponding to independent cluster-pairs that have H I or O VI coverage in the corresponding QSO spectrum at the redshift of the pair are displayed. Of the 25 independent cluster-pairs detected in our survey, we identify that 20 have H I coverage and 24 have O VI coverage. Conse-

quently, the panels corresponding to H I, NLAs, and BLAs include 20 data points, while the panel corresponding to O VI includes 24 data points. In Section 2.3, we show the regions in the spectra where the independent cluster-pairs are located for H I and O VI. In Figure 4.24, we consider absorptions within $\Delta v = \pm 1000$ km s^{-1} from the redshifts of a given independent cluster-pair, whereas in Figure 4.25 we consider $\Delta v = \pm 500$ km s^{-1}.

We present the covering fraction of each absorber in approximately $\Delta v = \pm 1000$ km s^{-1} and $\Delta v = \pm 500$ km s^{-1} along the sightline close to the independent cluster-pairs named $f_c^{filament}$, and we compared them with the random expectation f_c^{random}. The estimation for the distinct absorption lines is shown in the same colors used previously.

To estimate the random covering fraction f_c^{random}, we use equation (4.10), taken from Tejos et al. 2016:

$$f_c^{random} = \begin{cases} \Delta z(\Delta v)\frac{dN}{dz}|_{field} & \text{if } \Delta z(\Delta v)\frac{dN}{dz}|_{field} < 1 \\ 1 & \text{if } \Delta z(\Delta v)\frac{dN}{dz}|_{field} \geq 1 \end{cases} \tag{4.10}$$

Here, $\frac{dN}{dz}|_{field}$ is the expected field, $\Delta z(\Delta v)$ is the redshift path to a rest-frame velocity window Δv, evaluated at the median redshift of our independent cluster-pairs sample. For our survey, $z = 0.226$ for both H I and O VI.

We estimate the covering fraction of filaments close to independent cluster-pairs, $f_c^{filament} = n_{hits}/n_{trials}$, where n_{hits} are sightlines showing absorption in a given sample, within $\Delta v = \{\pm 1000, \pm 500\}$ km s^{-1} and within $\Delta d \leq 3$ Mpc, and n_{trials} are defined as the total number of sightlines where absorptions could have been detected.

To estimate the uncertainties for f_c^{random} and $f_c^{filament}$, we used the Bayesian formalism assuming a confidence level of 1σ for a binomial distribution, for the number of 'hits' given the number of independent cluster-pairs 'trials' for each transition (Cameron 2011).

The covering fraction of H I at $\Delta v = \pm 1000$ km s^{-1} is $f_c^{filament} = 0.90^{+0.06}_{-0.12}$, a value close to 1, which is in agreement with Figure 4.24, where almost every independent cluster-pair is filled for H I. For the samples of NLAs and BLAs, we obtained covering fractions of $0.45^{+0.14}_{-0.13}$ and $0.80^{+0.09}_{-0.13}$, respectively. Finally, in Table 4.2, we compare the covering fractions found in our survey for each sample with the random expectation, considering a rest-frame velocity window of $\Delta v = \pm 1000$ km s^{-1} (see also Figure 4.26) and $\Delta v = \pm 500$ km s^{-1} (see also Figure 4.27).

For BLAs and O VI, at a rest-frame velocity window of $\Delta v = \pm 1000$ km s^{-1}, the covering fraction found in our study, close to cluster-pairs, is greater than their respective random expectation. However, for NLAs, the covering fraction detected is smaller than the random expectation, consistent within 1σ confidence level. For a smaller rest-frame velocity window of $\Delta v = \pm 500$ km s^{-1} (Figure 4.27), we find that covering fractions for BLAs and O VI are even higher than their respective randomly expected values. Consequently, we have found that the excesses in the covering fraction, at both rest-frame

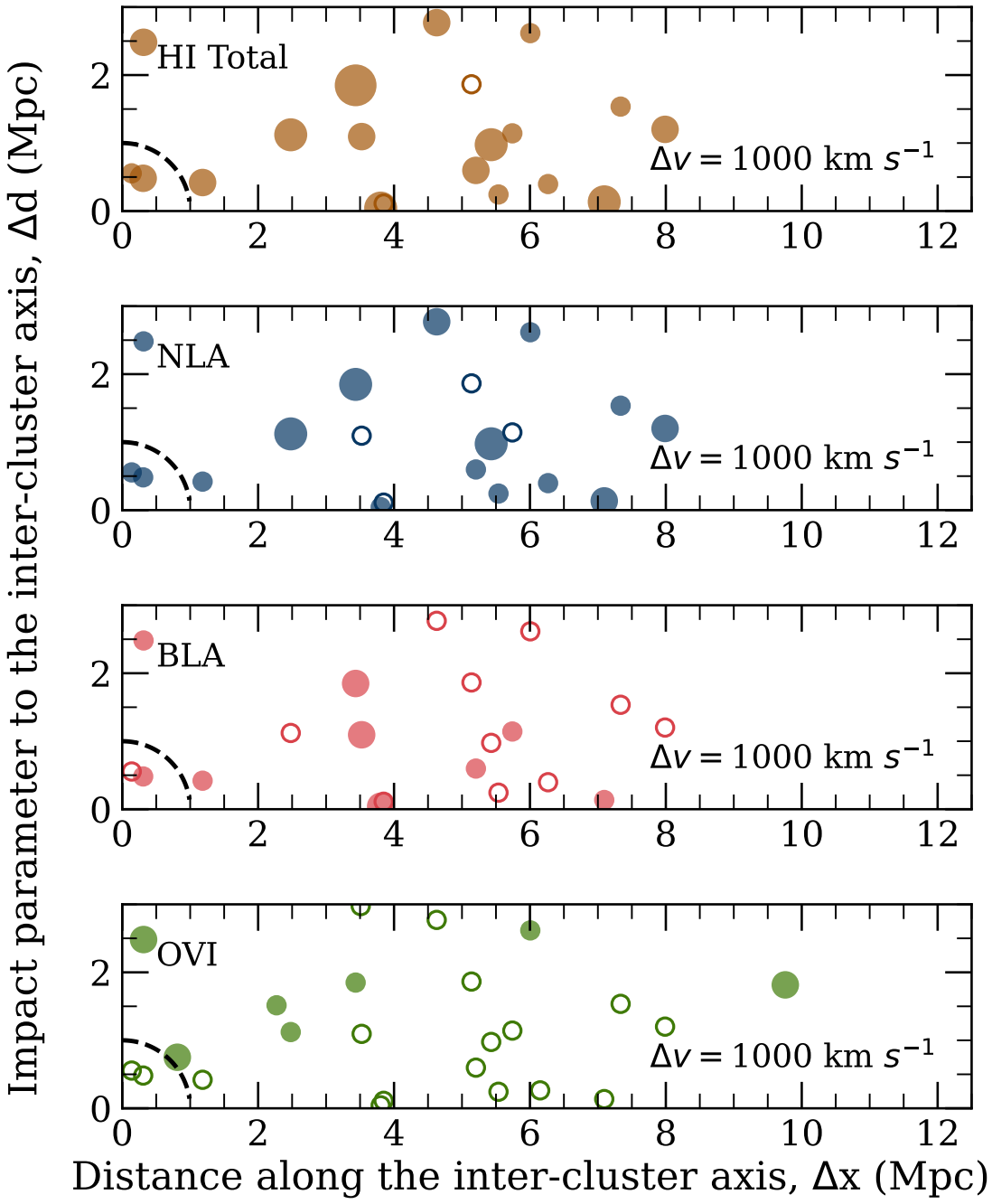

Figure 4.24: Representation of the position of each independent cluster-pair of our survey, relative to its corresponding QSO sightline. The y-axis indicates the impact parameter to a given cluster-pair, Δd; while the x-axis indicates the distance of the closest galaxy cluster in a given cluster-pair to the QSO sightline, known as Δx. Filled symbols correspond to regions of the sightline showing absorption line samples of the species indicated in each panel within Δv from the redshifts of the corresponding cluster-pair. The size of the symbols is proportional to the number of detected absorption lines. Empty symbols correspond to regions of the sightline showing no absorptions. We consider absorptions within a rest-frame velocity window $\Delta v = \pm 1000$ km s^{-1} around independent cluster pairs.

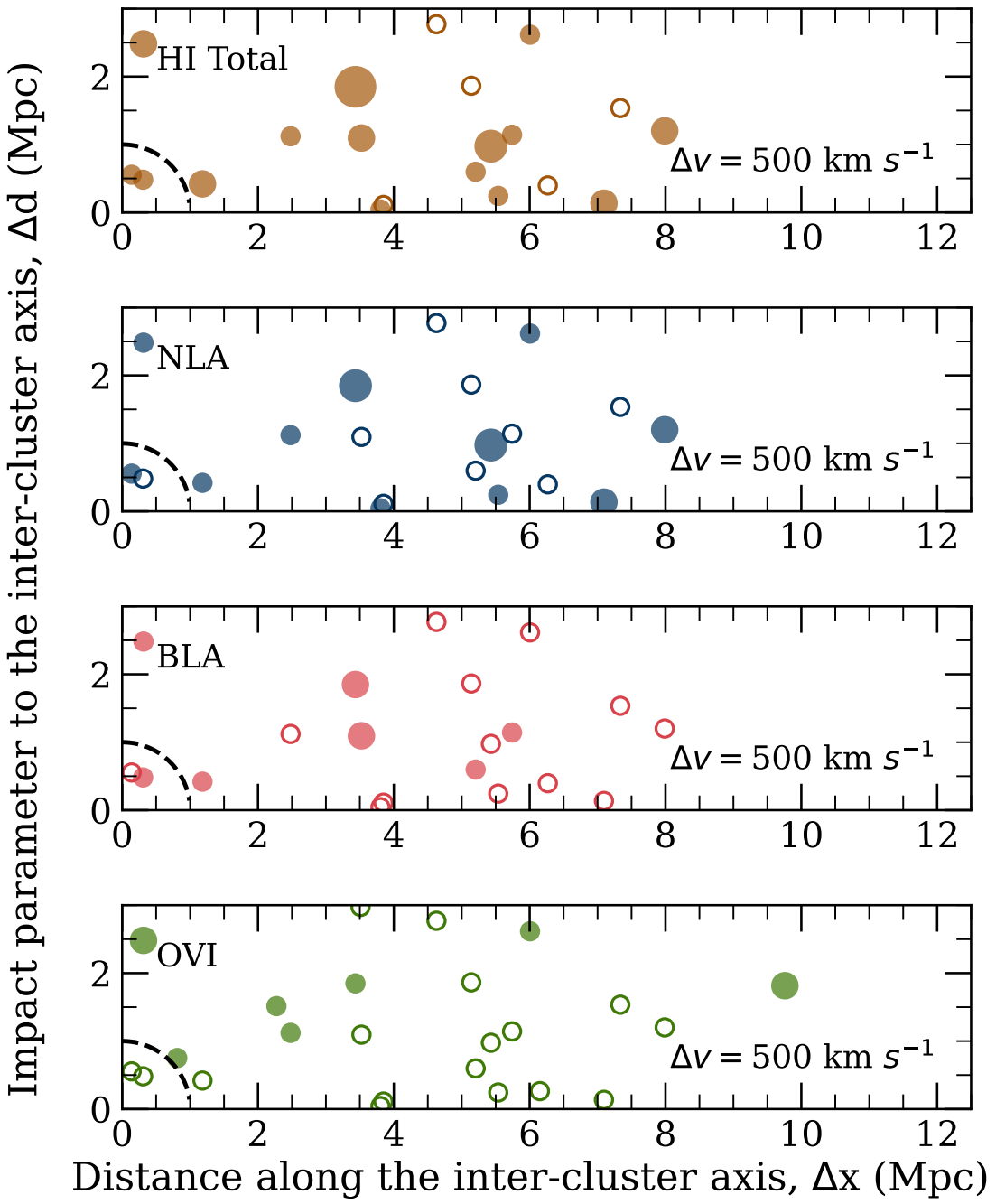

Figure 4.25: Representation of the position of each independent cluster-pair of our survey, relative to its corresponding QSO sightline. The y-axis indicates the impact parameter to a given cluster-pair, Δd; while the x-axis indicates the distance of the closest galaxy cluster in a given cluster-pair to the QSO sightline, known as Δx. Filled symbols correspond to regions of the sightline showing absorption line samples of the species indicated in each panel within Δv from the redshifts of the corresponding cluster-pair. The size of the symbols is proportional to the number of detected absorption lines. Empty symbols correspond to regions of the sightline showing no absorptions. We consider absorptions within a rest-frame velocity window $\Delta v = \pm 500$ km s^{-1} around independent cluster-pairs.

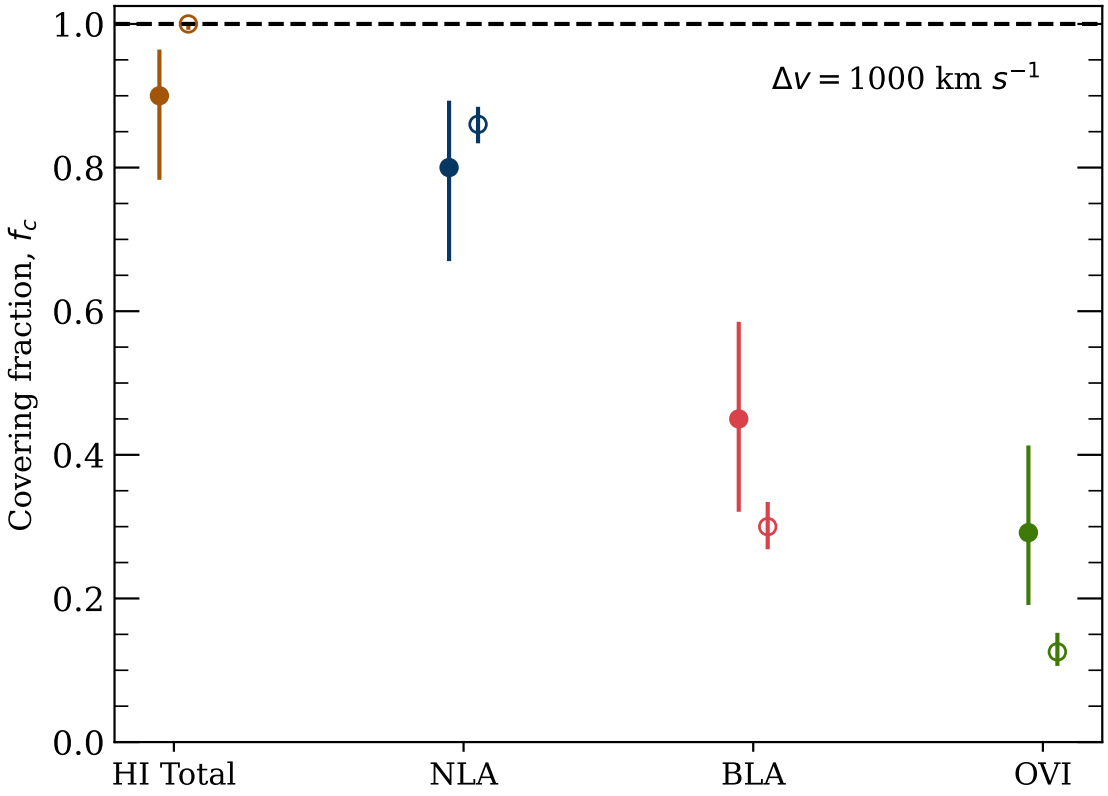

Figure 4.26: Covering fraction for samples of total H I, NLAs, BLAs, and O VI within a rest-frame velocity window of $\Delta v = \pm 1000$ km s^{-1} around independent cluster-pairs in solid symbols, $f_c^{filament}$; and their corresponding randomly expected values in open symbols, f_c^{random}.

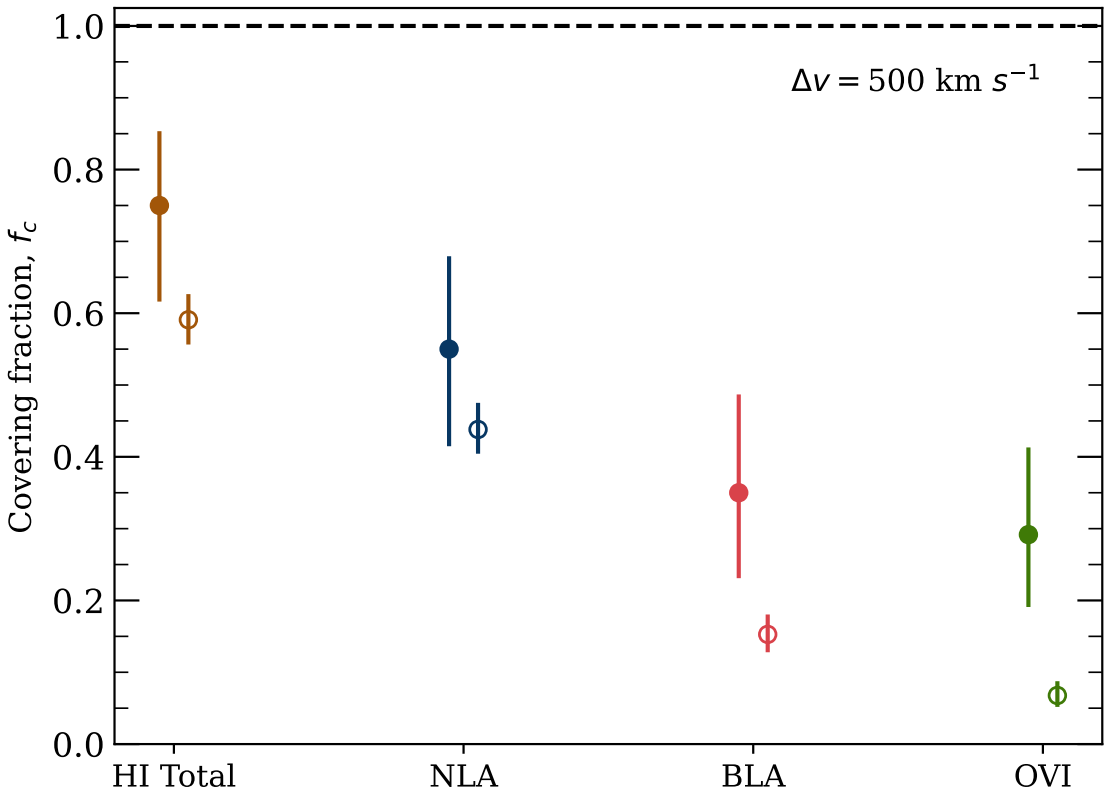

Figure 4.27: Covering fraction for samples of total H I, NLAs, BLAs, and O VI within a rest-frame velocity window of $\Delta v = \pm 500$ km s^{-1} around independent cluster-pairs in solid symbols, $f_c^{filament}$; and their corresponding randomly expected values in open symbols, f_c^{random}.

Sample	n_{hits}	n_{trials}	$f_c^{filament}$	f_c^{random}	Excess
(1)	(2)	(3)	(4)	(5)	(6)
$\Delta v = \pm 1000 \mathrm{km\,s^{-1}}$ and $\Delta d \leq 3$ Mpc					
HI Total	18	20	$0.9^{0.06}_{-0.12}$	$1^{0.0}_{-0.01}$	0.9
NLA	16	20	$0.8^{0.09}_{-0.13}$	$0.85^{0.02}_{-0.03}$	0.9
BLA	9	20	$0.45^{0.14}_{-0.13}$	$0.32^{0.03}_{-0.03}$	1.5
OVI	7	24	$0.29^{0.12}_{-0.1}$	$0.13^{0.03}_{-0.02}$	2.3
$\Delta v = \pm 500 \mathrm{km\,s^{-1}}$ and $\Delta d \leq 3$ Mpc					
HI Total	15	20	$0.75^{0.1}_{-0.13}$	$0.6^{0.03}_{-0.04}$	1.3
NLA	11	20	$0.55^{0.13}_{-0.14}$	$0.43^{0.03}_{-0.04}$	1.3
BLA	7	20	$0.35^{0.14}_{-0.12}$	$0.16^{0.03}_{-0.02}$	2.3
OVI	7	24	$0.29^{0.12}_{-0.1}$	$0.07^{0.02}_{-0.02}$	4.3

Table 4.2: Covering fraction for samples of total H I, NLAs, BLAs, and O VI, within a rest-frame velocity window of $\Delta v = \pm 1000$ km s^{-1} (top) and $\Delta v = \pm 500$ km s^{-1} (right) around independent cluster-pairs. (1) Transition of absorbing gas. (2) Number of independent cluster-pairs showing absorption of a given transition. (3) Total number of independent-cluster-pairs where we can detect transitions. (4) Covering fraction close to cluster-pairs for each transition. (5) Covering fraction for a random sightline, estimated using equation (4.10). (6) Excess covering fraction, calculated as $f_c^{filament}/f_c^{random}$.

velocity windows, for BLAs and O VI are greater than the excess for NLAs. Since BLAs and O VI trace temperatures of $\sim 1 - 3 \times 10^5$ K (Richter et al. 2006a) respectively, a greater excess in these ion species than cold gas tracers (NLAs) suggests that the potential filaments associated with the independent cluster-pairs in our survey might be tracing the WHIM. Indeed, the increase in the covering fractions of BLAs and O VI observed in this work towards inter-cluster axes, relative to random expectations, constitutes another WHIM signature detected.

Furthermore, it is worth emphasizing that when characterizing absorption lines, certain biases and/or systematics can affect the analysis and/or interpretation. In addition, noise and line blends can potentially mimic broad and shallow absorption features (Richter et al. 2006a, Tejos et al. 2016, Pessa et al. 2025). This justifies the use of higher S/N, which enables a better characterization of the kinematic structure of the absorption features (Richter et al. 2006a, Danforth et al. 2010). Finally, we highlight the possibility that not all BLAs and O VI- detected systems strictly trace the WHIM.

The restrictions imposed on the catalogs were designed to prioritize QSO sightlines with possible intervening filaments. Therefore, our approach increases the likelihood of

detecting intergalactic structures in our survey. However, we cannot be certain whether any cluster-pairs in our survey are truly tracing inter-cluster filaments because some filaments might be warped or displaced from the direct cluster–cluster axis (Colberg et al. 2005), implying that a sightline aligned with the cluster-pair does not necessarily intersect the filamentary structure. However, the presence of a non-straight filament should imply an underestimation of the signal, if anything (Meng et al. 2026). In fact, there is always the possibility of not detecting any transitions of interest near the defined cluster-pairs at a velocity window of ± 1000 km s^{-1} (as in the case of QSO J1410+0910). For instance, the inclusion of this QSO in the redshift number density measurement results in an increase of the redshift path measurement without an increase in detections. If we assume this QSO does not intersect a filament and we remove it from the analysis, then we find an increase of 6.8 and 14.1 in the redshift number density of BLAs and NLAs, respectively, at the fiducial values. Finally, even if cluster-pairs trace intergalactic filaments, insufficient SNR in the spectra may prevent the detection of H I and O VI absorption lines; for that reason, we analyze the quality of our survey, measuring the SNR in the QSO spectra at the expected observed wavelength for relevant absorption features (H I and O VI), as indicated in Section 2.3.

4.3 Concluding remarks

Based on the results of the analysis of our experiment, the following conclusions are presented:

- The absorption lines of WHIM tracers (BLAs and O VI) identified in our survey for a velocity window $\Delta v = \pm 1000$ km s^{-1}, and $\Delta d \leq 3$ Mpc from the cluster-pairs are indicated in Figures 4.3 and 4.4. Nine out of the ten QSO spectra of our survey show absorption features from at least one of these two WHIM tracers. This finding suggests that we could have traced the WHIM using this methodology.

- From the distribution of Doppler parameter (b) and column density ($\log N$) of H I in Figures 4.6 and 4.7, we conclude that an observational bias may arise against the detection of BLAs with b ≥ 80 [km s^{-1}] and with column densities ($\log$[N/cm^{-2}]) $\leq$ 13. This could be due to the resolution of the HST/COS instrument, which cannot resolve broadened, shallow lines. In the case of O VI, the amount of detected lines is significantly lower than that for H I.

- We present the redshift number density (dN/dz) in Figures 4.12-4.19. Here, we conclude that near the independent cluster-pairs at velocity windows $\Delta v = \pm 1000$ km s^{-1}, we observed a higher incidence than expected in the field, which could

confirm the presence of intergalactic filaments between cluster-pairs. From Figures 4.20-4.23, we conclude that all the tracers have an excess of absorptions where intergalactic filaments should exist. Indeed, the excess of O VI is around three times the expected field. We argued that the larger relative excess detected for BLAs in regions near cluster-pairs, compared with NLAs, may be an indirect signature of the WHIM.

- From Figures 4.26 and 4.27, we conclude that the WHIM tracers (BLAs and O VI) exhibit a higher covering fraction close to cluster-pairs compared to a random control sample. At a rest-frame velocity windows of $\Delta v = \pm 1000$ km s^{-1} and $\Delta v = \pm 500$ km s^{-1}, the excesses in the covering fraction of BLAs and O VI are larger than that of NLAs. This implies that near the inter-cluster axis, the WHIM is more likely to be detected by this technique.

Chapter 5

Pinpointing the cosmic web between massive galaxy clusters II: Overdensities of WHIM absorbers

Chapter based on the article ***Karen Martínez-Acosta****, et al. in prep. Tentative title: "Pinpointing the cosmic web between massive galaxy clusters II: Overdensities of WHIM absorbers".*

5.1 Overview

In this chapter, we briefly describe the aim of the next article associated with this research, which is currently in progress. The focus of this work is to identify the overdensities ($\rho/\langle\rho\rangle$) associated with regions where BLAs are detected. To identify overdensities associated with different regions of the Universe, we use products generated by the Monte Carlo Physarum Machine (Burchett et al. 2020). The MCPM algorithm mimics the growth of the Physarum Polycephalum (Slime mold). This algorithm generates optimal transport networks to connect discrete locations (Burchett et al. 2020).

Applying the MCPM algorithm to both simulated and observational cosmological data yields consistent 3D density maps of the cosmic web. Figure 5.1 illustrates the reconstruction of the cosmic web using the MCPM, applied to a sample of 37 662 galaxies from the Sloan Digital Sky Survey (SDSS). The upper panel presents a large-scale view of the emergent filamentary network identified by the MCPM algorithm. This reconstruction is obtained using only the observed galaxy positions, redshifts, and masses, without imposing any explicit assumptions about the underlying large-scale structure. The resulting network highlights the continuous and interconnected nature of cosmic filaments. The lower panels display three representative subregions, where the discrete SDSS galaxy distribution (G) is shown together with the superimposed MCPM filament density field

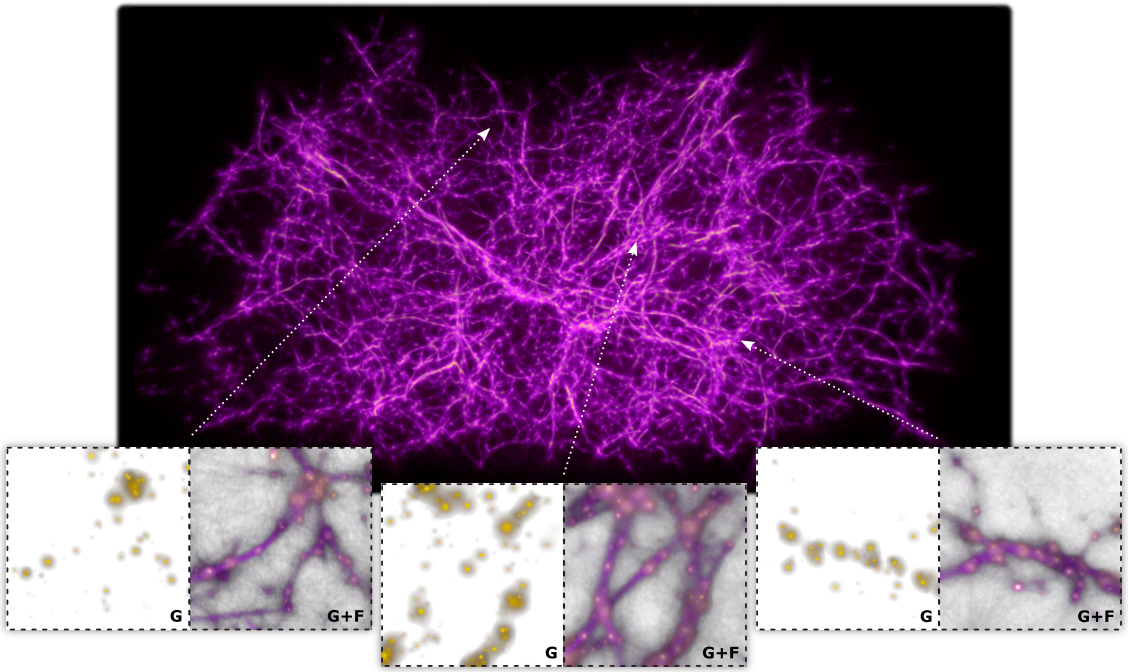

Figure 5.1: MCPM reconstruction of the cosmic web based on 37 662 galaxies from the SDSS. Top: large-scale view of the emergent structure identified by the MCPM algorithm. Bottom: three representative subregions illustrating the SDSS galaxy distribution (G) together with the overlaid MCPM filament density field (F) (Burchett et al. 2020).

(G+F). These examples demonstrate how the MCPM method implicitly traces the cosmic web structure by identifying efficient continuous pathways connecting galaxies, which preferentially reside along filamentary structures Burchett et al. 2020.

The work of Wilde et al. 2023 produced a Value-Added Catalog (VAC) and nine data cubes that contain local overdensities. The VAC contains the density at the location of a set of 638 820 galaxies, and the data cubes incorporate the full 3D density field of the relevant volumes. These data can be queried using the library Pyslime [1]. We retrieved the local overdensity at any point in the cosmic web from the data cubes and cross-matched it with the VAC to derive calibration factors for each data cube. This was necessary because the density in the VAC is given on a logarithmic scale, whereas the data cubes use a linear scale.

This procedure was carried out as follows. For each data cube j, we first identified all galaxies i from the VAC that lie within the spatial volume covered by that data cube. Using the astronomical coordinates of these galaxies, we sample the corresponding voxel values, $\rho_{i,j}$, from the density field stored in the data cube. This was done using the sky_to_data function from Pyslime. For each cube, we computed the mean density, $\langle \rho_{i,j} \rangle_i$, by averaging the density values at the galaxy locations within that cube. All calculations were performed excluding undefined, zeros, and non-finite (NaN) values. The calibra-

[1] https://github.com/jnburchett/pyslime

Data cube, j (1)	Redshift range (2)	Region (3)	Calibration factor, A_j (4)
0	0.01<z<0.10	NGC	0.9735
1	z<0.20	NGC	1.0238
2	z<0.20	SGC	1.0409
3	0.18<z<0.30	NGC	0.9364
4	0.18<z<0.30	SGC	1.0316
5	0.28<z<0.38	NGC	0.3043
6	0.28<z<0.38	SGC	0.3800
7	0.36<z<0.51	NGC	0.2949
8	0.36<z<0.51	SGC	0.3265

Table 5.1: Characteristics of data cubes. Columns (1)-(4) indicate the ID, redshift range, region, and calibration factor for each data cube, respectively.

tion factor associated with each data cube A_j was subsequently determined according to equation (5.1).

$$A_j = \frac{\langle \rho_{i,\mathrm{VAC}} \rangle_i}{\left\langle \log_{10} \frac{\rho_{i,j}}{\langle \rho_{i,j} \rangle_i} \right\rangle_i}. \tag{5.1}$$

where $\rho_{i,\mathrm{VAC}}$ is the overdensity of galaxy i, given in the VAC.

Finally, we apply a base-10 logarithm transformation to all voxel values in each data cube. The transformed values were then scaled by the corresponding calibration factor A_j, yielding the calibrated overdensities for subsequent analysis. The calibration factor was required to ensure consistency between the density field reported in the data cubes and the density values of the galaxies provided in the VAC.

As an illustration, Figure 5.2 compares the overdensities retrieved from the VAC (shown in green) for a random sample of 100 galaxies with those retrieved from the calibrated data cube at the corresponding astronomical coordinates for data cube 0. For clarity, the figure displays only a small subset of the 300 130 galaxies employed in the calibration of data cube 0. The same procedure was subsequently applied to calibrate the remaining eight data cubes.

The calibration values that we found for the data cubes are summarized in Table 5.1. Additionally, Table 5.1 lists the redshift intervals spanned by each data cube and specifies their location within either the Northern Galactic Cap (NGC) or the Southern Galactic Cap (SGC) regions.

In particular, we aim to use the astronomical coordinates of the detected absorption features from the QSO spectra analyzed in Chapter 4, jointly with the calibrated data cubes, to retrieve and analyze their local overdensities. We aim to compare overdensities associated with BLAs with those of NLAs and with randomly selected control samples to assess their statistical significance. In addition, we expect to investigate correlations

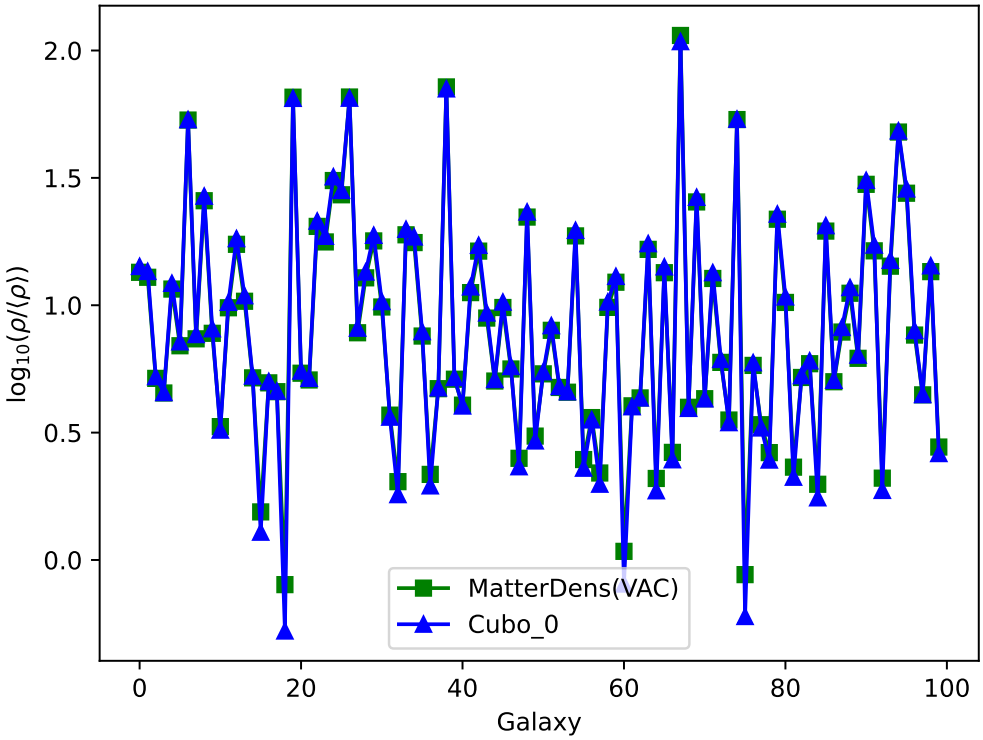

Figure 5.2: Calibration of data cubes using the VAC (first approach) at $z \leq 0.1$ (Cube 0). We show the overdensities retrieved from the VAC (in green) for a random sample of 100 galaxies, and the overdensities retrieved at the astronomical coordinates of the same galaxies using the data cubes (in blue) after calibration.

between measured observational parameters, such as Doppler parameter and column density, and the overdensities of the identified absorption features.

Finally, we indicate that the results presented so far in this Chapter constitute a work in progress. We have only presented an initial perspective on our future work. At this stage, we have chosen to include the components that are fully developed and internally validated, while additional analyses and results are currently being completed and will be presented in the subsequent article.

Chapter 6

Thesis conclusions

Using a novel experiment, we obtained a sample of ten QSO sightlines that meet the criteria for probing inter-cluster regions (described in Section 2.2) and used them to search for intergalactic filaments. In this way, we obtained 25 cluster-pairs that define independent intergalactic structures. We analyzed the QSO sightline spectra obtained in FUV from HST/COS and characterized those whose sightline likely intersect these filaments. We identified all absorption lines in the spectra, not only those where inter-cluster filaments are expected to exist. We estimated observational parameters, such as the Doppler parameter and column density, via Voigt profile fitting for each transition. With these samples, we investigated the incidence of two tracers of the WHIM: BLAs and O VI. We separated the H I absorptions in two samples, BLAs and NLAs, based on the width of the line, and we used a Doppler parameter $b \geq 40$ km s^{-1} for BLAs. Subsequently, we analyzed the redshift number density (dN/dz), the relative excess ($\frac{dN}{dz}/\frac{dN}{dz}|_{field}$), and the covering fraction ($f_c^{filament}$) for total H I, NLAs, BLAs, and O VI.

In Chapter 3, we report the methodology used to identify absorption components along the spectra of a QSO sightline acquired in the FUV range in the HST/COS for QSO SDSSJ161940.56+254323.0. Since the interest of our work is to probe WHIM, we focus our analysis on observational parameters of BLA features and further analyze metal absorptions in the QSO spectra at the same redshift, providing further evidence of the galactic origin of these features. Additionally, we present statistical validation of the detection method, evaluating different fitting approaches using the BIC to determine whether single- or multiple-component models are better suited to the observed spectra. We use a sample of 13 broad Lyα absorbers (BLAs) detected in the HST/COS spectrum of a single QSO ($z \sim 0.2685$), whose sightline intersects several inter-cluster axes, to study the relation between BLAs and the large-scale structure of the Universe. Local overdensities of galaxies at the redshifts of the BLAs were inferred from VLT/MUSE and VLT/VIMOS data to assess the potential association of the BLAs with nearby galaxies (see Pessa et al. 2025 for further details). Altogether, in this research, we find that most of the BLAs iden-

tified in the FUV spectra of QSO SDSSJ161940.56+254323.0 are really tracing WHIM, and that WHIM properties correlate with the distribution of galaxies within its local volume, where denser intergalactic gas correlates with a stronger local excess of galaxies, relative to the cosmic expectancy.

In Chapter 4, we analyze the incidence of WHIM tracers using the spectra of a survey of QSOs (described in Chapter 2). Nine out of the ten QSO spectra of our survey show absorption features from at least one of the WHIM tracers (BLAs and O VI). This finding suggests that we might have been able to trace the WHIM with this methodology. Near the independent cluster-pairs at velocity windows $\Delta v = \pm 1000$ km s^{-1}, we observed a higher incidence than expected in the field, which could confirm the presence of intergalactic filaments between cluster-pairs. Indeed, all tracers have an excess of absorptions where intergalactic filaments should exist. Particularly, the excess of O VI is around 2.6 times the expected field value. We argued that the larger relative excess detected for BLAs in regions near cluster-pairs, compared with NLAs, may be an indirect signature of the WHIM. In addition, WHIM tracers exhibit a higher covering fraction close to cluster-pairs compared to a random control sample. At a rest-frame velocity windows of $\Delta v = \pm 1000$ km s^{-1} and $\Delta v = \pm 500$ km s^{-1}, the excesses in the covering fraction of BLAs and O VI are larger than that of NLAs. This implies that near the inter-cluster axis, the WHIM is more likely to be detected by this technique. These results confirm the trends reported by Tejos et al. 2016 with a much larger sample size, indicating robustness. In summary, it may be stated that, based on the incidences determined in this work, a tentative excess of WHIM tracers is reported for our survey. Although the uncertainties are large, we obtained a representative result for what may be happening in the WHIM of the inter-cluster filaments.

Chapter 5 provides a brief introduction to a component of the future work associated with this research. We first introduce the application of Monte Carlo Physarum Polycephalum (MCPM) to cosmological data for the reconstruction of density maps of the cosmic web. In particular, we describe the use of the dataset reported by Wilde et al. 2023 and the procedure adopted to calibrate the overdensity data cubes. The direction of this component of the research is to retrieve and analyze the local overdensities associated with BLAs and to investigate their correlations with the observational parameters of the absorption features.

In summary, these results confirm previous reported trends by Tejos et al. 2016 with a much larger sample size, indicating robustness. As a general and final conclusion, it may be stated that, based on the incidences determined in this paper, a tentative excess of WHIM tracers is reported for our survey. Although the uncertainties are large, we obtained a representative result for what may be happening in the WHIM of the inter-cluster filaments.

As future work, we expect to increase the number of sightlines in the survey by using the HST data archive to reduce uncertainties in the incidence of H I and O VI. Finally, we aim to further explore our observational results by reproducing the experiment using cosmological simulations of the low-redshift intergalactic medium, which have not been previously explored in this context.

Bibliography

Ahoranta, J., Nevalainen, J., Wijers, N., et al. 2020, A&A, 634, A106

Aragón-Calvo, M. A., van de Weygaert, R., & Jones, B. J. T. 2010, MNRAS, 408, 2163

Benson, A. J., Frenk, C. S., Baugh, C. M., Cole, S., & Lacey, C. G. 2001, MNRAS, 327, 1041

Bianchi, L., Conti, A., & Shiao, B. 2014, VizieR Online Data Catalog: GALEX-GR6/7 data release (Bianchi+ 2014), VizieR On-line Data Catalog: II/335. Originally published in: 2014AdSpR..53..900B

Bond, J. R., Kofman, L., & Pogosyan, D. 1996, Nature, 380, 603

Bonjean, V., Aghanim, N., Salomé, P., Douspis, M., & Beelen, A. 2018, A&A, 609, A49

Bouma, S. J. D., Richter, P., & Wendt, M. 2021, A&A, 647, A166

Bregman, J. N. 2007, ARA&A, 45, 221

Burchett, J. N., Elek, O., Tejos, N., et al. 2020, ApJ, 891, L35

Butsky, I. S., Burchett, J. N., Nagai, D., et al. 2019, MNRAS, 490, 4292

Cameron, E. 2011, PASA, 28, 128

Cen, R. & Fang, T. 2006, ApJ, 650, 573

Cen, R. & Ostriker, J. P. 1999, ApJ, 514, 1

Cen, R. & Ostriker, J. P. 2006, ApJ, 650, 560

Colberg, J. M., Krughoff, K. S., & Connolly, A. J. 2005, Monthly Notices of the Royal Astronomical Society, 359, 272

Danforth, C. W., Keeney, B. A., Tilton, E. M., et al. 2016, ApJ, 817, 111

Danforth, C. W. & Shull, J. M. 2008, ApJ, 679, 194

Danforth, C. W., Shull, J. M., Rosenberg, J. L., & Stocke, J. T. 2006, ApJ, 640, 716

Danforth, C. W., Stocke, J. T., & Shull, J. M. 2010, ApJ, 710, 613

Davé, R. 2003, arXiv e-prints, astro

Davé, R., Cen, R., Ostriker, J. P., et al. 2001, ApJ, 552, 473

de Graaff, A., Cai, Y.-C., Heymans, C., & Peacock, J. A. 2019, A&A, 624, A48

de Lapparent, V., Geller, M. J., & Huchra, J. P. 1986, ApJ, 302, L1

D'Odorico, V. 2023, Experimental Astronomy, 55, 209

Draine, B. T. 2011, Physics of the Interstellar and Intergalactic Medium (Princeton University Press)

Eckert, D., Jauzac, M., Shan, H., et al. 2015, Nature, 528, 105

Farnes, J., Mort, B., Dulwich, F., Salvini, S., & Armour, W. 2018, Galaxies, 6, 120

Galárraga-Espinosa, D., Aghanim, N., Langer, M., & Tanimura, H. 2021, A&A, 649, A117

Gehrels, N. 1986, ApJ, 303, 336

González, R. E. & Padilla, N. D. 2010, MNRAS, 407, 1449

Green, J. C., Froning, C. S., Osterman, S., et al. 2012, ApJ, 744, 60

Haardt, F. & Madau, P. 1996, ApJ, 461, 20

Hodge, P. E., Keyes, C., & Kaiser, M. 2007, in American Astronomical Society Meeting Abstracts, Vol. 211, American Astronomical Society Meeting Abstracts, 135.03

Holguin Luna, P., Burchett, J. N., Nagai, D., et al. 2024, arXiv e-prints, arXiv:2411.13551

Hu, T., Khaire, V., Hennawi, J. F., et al. 2024, MNRAS, 527, 11338

James, B. L., Berg, D. A., King, T., et al. 2022, ApJS, 262, 37

Koplitz, B., Ramesh, A., & Borthakur, S. 2024, Investigating Ionization in the Intergalactic Medium

Lehner, N., Savage, B. D., Richter, P., et al. 2007, ApJ, 658, 680

Locatelli, N., Vazza, F., Bonafede, A., et al. 2021, A&A, 652, A80

Luber, N. M., Hasan, F., van Gorkom, J. H., et al. 2025, ApJ, 985, 214

Macquart, J. P., Prochaska, J. X., McQuinn, M., et al. 2020, Nature, 581, 391

Mandelker, N., van den Bosch, F. C., Springel, V., & van de Voort, F. 2019, ApJ, 881, L20

Martizzi, D., Vogelsberger, M., Artale, M. C., et al. 2019, MNRAS, 486, 3766

McQuinn, M. 2014, ApJ, 780, L33

McQuinn, M. 2016, ARA&A, 54, 313

Meiksin, A. A. 2009, Reviews of Modern Physics, 81, 1405

Meng, Y., Zheng, H., Liao, S., et al. 2026, ApJ, 998, 251

Monroe, T. R., Prochaska, J. X., Tejos, N., et al. 2016, AJ, 152, 25

Nicastro, F. 2016, in XMM-Newton: The Next Decade, ed. J.-U. Ness, 27

Pâris, I., Petitjean, P., Aubourg, É., et al. 2012, A&A, 548, A66

Pessa, I., Tejos, N., Barrientos, L. F., et al. 2018, MNRAS, 477, 2991

Pessa, I., Tejos, N., Martinez-Acosta, K., et al. 2025, A&A, 698, A116

Planck Collaboration, Ade, P. A. R., Aghanim, N., et al. 2014, A&A, 571, A16

Planck Collaboration, Ade, P. A. R., Aghanim, N., et al. 2016, A&A, 594, A13

Prause, N., Reimers, D., Fechner, C., & Janknecht, E. 2007, A&A, 470, 67

Prochaska, J. X., Tejos, N., Crighton, N., et al. 2016, Linetools/Linetools: Second Major Release, Zenodo

Reiprich, T. H., Veronica, A., Pacaud, F., et al. 2021, A&A, 647, A2

Richter, P. 2010, in 38th COSPAR Scientific Assembly, Vol. 38, 2

Richter, P., Fang, T., & Bryan, G. L. 2006a, A&A, 451, 767

Richter, P., Paerels, F. B. S., & Kaastra, J. S. 2008, Space Sci. Rev., 134, 25

Richter, P., Savage, B. D., Sembach, K. R., & Tripp, T. M. 2006b, A&A, 445, 827

Rykoff, E. S., Rozo, E., Busha, M. T., et al. 2014, ApJ, 785, 104

Sameer, Charlton, J. C., Wakker, B. P., et al. 2024, MNRAS, 530, 3827

Sargent, W. L. W., Young, P. J., Boksenberg, A., & Tytler, D. 1980, ApJS, 42, 41

Savage, B. D., Lehner, N., & Narayanan, A. 2011, ApJ, 743, 180

Schaye, J., Crain, R. A., Bower, R. G., et al. 2015, MNRAS, 446, 521

Schaye, J., Kugel, R., Schaller, M., et al. 2023, MNRAS, 526, 4978

Schneider, D. P., Richards, G. T., Hall, P. B., et al. 2010, AJ, 139, 2360

Schwarz, G. 1978, Annals of Statistics, 6, 461

Shull, J. M., Smith, B. D., & Danforth, C. W. 2012, ApJ, 759, 23

Springel, V., White, S. D. M., Jenkins, A., et al. 2005a, Nature, 435, 629

Springel, V., White, S. D. M., Jenkins, A., et al. 2005b, Nature, 435, 629

Tanimura, H., Aghanim, N., Bonjean, V., Malavasi, N., & Douspis, M. 2020, A&A, 637, A41

Tanimura, H., Aghanim, N., Douspis, M., & Malavasi, N. 2022, A&A, 667, A161

Tejos, N. 2025, arXiv e-prints, arXiv:2504.12539

Tejos, N., Prochaska, J. X., Crighton, N. H. M., et al. 2016, MNRAS, 455, 2662

Tepper-García, T., Richter, P., Schaye, J., et al. 2012, MNRAS, 425, 1640

Tepper-García, T., Richter, P., Schaye, J., et al. 2011, MNRAS, 413, 190

Thom, C. & Chen, H.-W. 2008, ApJ, 683, 22

Tripp, T. M., Sembach, K. R., Bowen, D. V., et al. 2008, ApJS, 177, 39

Vernstrom, T., Heald, G., Vazza, F., et al. 2021, MNRAS, 505, 4178

Vogelsberger, M., Genel, S., Sijacki, D., et al. 2013, MNRAS, 436, 3031

Wakker, B. P., Hernandez, A. K., French, D. M., et al. 2015, ApJ, 814, 40

White, S. D. M. & Frenk, C. S. 1991, ApJ, 379, 52

Wilde, M. C., Elek, O., Burchett, J. N., et al. 2023, arXiv e-prints, arXiv:2301.02719

Yang, L., Katz, N., Scannapieco, E., & Brüggen, M. 2025, MNRAS, 540, 2195

Yao, Y., Nowak, M. A., Wang, Q. D., Schulz, N. S., & Canizares, C. R. 2008, ApJ, 672, L21

Zhang, X., Bulbul, E., Malavasi, N., et al. 2024, A&A, 691, A234

Zhao, Y., Xu, H., Liu, A., et al. 2025, A&A, 695, A15